Analyzing stress change and energy budget of earthquakes through physics-based modeling

Thesis by
Stephen M. Perry

In Partial Fulfillment of the Requirements for the
Degree of
Doctor of Philosophy

CALIFORNIA INSTITUTE OF TECHNOLOGY
Pasadena, California

2018
Defended February 21, 2018

Stephen M. Perry
ORCID: 0000-0003-1748-1827

ACKNOWLEDGEMENTS

This thesis is the cultivation of more than six years of work, and there is no way I could have completed it without the help of a great number of people both in the lab and at home.

I first thank my research advisor, Nadia Lapusta, for being an excellent teacher and mentor. There have been countless times where I entered her office in total confusion about a subject and then emerged soon after with the topic completely illuminated. She has helped me become a much better researcher by teaching me how to attack the research process and focus on the important research questions. Every student encounters adversity and feels like quitting at some point (or many) during their PhD and it takes an understanding and encouraging advisor to pick him or her back up. I was extremely lucky to have such an advisor. Thank you Nadia, for seeing me through to the finish line.

Our research group served a vital function throughout my time at Caltech, and I thank everyone that was a part of it. So many people took considerable time to help me with my research questions and problems when they had many of their own. Junle Jiang introduced me to the computer code, helped me understand how it works, and spent considerable time helping me debug cryptic error messages. Semechah Lui and Natalie Higgins helped me solve research questions, work through understanding the intricacies of the computer code, and kept me sane when the code inevitably broke due to some mistake on my part. So many other members of the group helped me brainstorm ideas, prepare talks, and put my research together into pieces that make up this thesis. I have to thank Yen-Yu Lin, Srivatsan Hulikal, Vito Rubino, Marcello Gori, Kavya Sudhir, Valere Lambert, Stacy Larochelle, and many others.

I also thank the other members of my thesis committee: Jean-Philippe Avouac, Victor Tsai, and Zhongwen Zhan, for the time they dedicated to my thesis and helping me improve upon my work. I interacted with all of them through my coursework in addition to my thesis and they all greatly increased my understanding of the geophysical world and the research techniques used to investigate it.

My first year at Caltech was very difficult, but I don't think I could have asked to arrive with a better cohort in the Seismolab. Chris Rollins, Bryan Riel, Semechah Lui, and Asaf Inbal provided the best support structure for tackling problem sets together late into the night, learning how to do original research, and navigating

the qualifying exam after our first year. You all treated me not just as a friend and colleague, but also like family.

I've met many brilliant people at Caltech and I am lucky enough to call many of them my friends. I have to thank my former roommates at "The Mansion": Krzysztof Chalupka, Robb Wills, Victoria Stevens, Vipul Singhal, and Tristan McKinney for keeping me sane and helping me to see that there is life outside of the lab. Both Vipul and Howard Hui lived with me at the Olive Tree and made the middle years of my PhD fun and enlightening. I'm so glad I had them to talk through roadblocks and vent to when research screeched to a halt due to some issue. I've learned so much from them all that cannot be taught in a lab.

I need to thank my entire family: my mother, my father, my brother Jamus, and my sister Kristine, for supporting me through the arduous and lengthy process that is the PhD. Thank you for keeping me going and telling me that I could do it, even when I thought I could not.

There were several friends who, though they lived thousands of miles away, were active in my live and a large part of my continued happiness. I've known Harrison Engle and Abraham Smith since middle school and both believed in me and helped me get through not only the tough work times, but also the challenging social times. Evan Walsh entered his PhD program at Harvard the same time I did and we kept each other afloat throughout graduate school; I don't know what I would have done without him. There were several times where Evan single-handedly kept me going because he was uniquely able to empathize with many of my challenges that others could not.

Lastly, I have to thank Bailey Ward for being the most supportive and understanding girlfriend in the world. She still loves me even after dealing with the worst versions of myself brought on by the incredible stress, sleeplessness, and crazy work hours that are part of completing the PhD. Especially during the final year when it really got down to crunch time, she was always there to comfort me, believe in me, and help me in any way she could. Thank you so much for persevering through it all and helping me to do the same.

ABSTRACT

Researchers use concepts such as stress drop, breakdown energy, and available energy to describe earthquakes sources and study earthquake physics. These quantities represent the spatially and temporally varying dynamic events by single, event-averaged values. They are inferred indirectly from observations, often based on simplified models. Thus, their relationship to fault constitutive properties, which are local on the fault, is not straightforward.

Here, we use simulations of earthquake sequences in fault models with friction laws motivated by laboratory experiments to examine how the event-averaged observables arise from spatially and temporally varying earthquake rupture. In particular, we consider whether several typically used fault mechanisms, such as rate-and-state friction, thermal pressurization of pore fluids, and flash heating, are consistent with common observations such as magnitude-invariant stress drop, increasing breakdown energy with the event size, and radiation efficiencies of ~0.5.

Stress drops, observed to be magnitude invariant, are a key characteristic used to describe natural earthquakes. Theoretical studies and lab experiments indicate that dynamic weakening, such as thermal pressurization of pore fluids, may be present on natural faults. At first glance, these two observations seem incompatible, since larger events may experience greater weakening and should thus have lower final stresses. We hypothesize that dynamic weakening can be reconciled with magnitude-invariant stress drops due to larger events having lower average prestress when compared to smaller events. The additional weakening would allow the final stresses to also be lower, but the stress drops may be similar.

To explore this hypothesis, we study long-term earthquake sequences on a rate-and-state fault segment with enhanced dynamic weakening due to thermal pressurization using a fully dynamic simulation approach with a seismogenic segment that has uniform friction properties. Our results show, for a range of event sizes, that such models can explain both observationally inferred stress drop invariance and breakdown energy increase with event magnitude. Smaller events indeed have larger average initial stresses than medium-sized events, and we get nearly constant stress drops for events spanning up to five orders of magnitude in seismic moment. Segment-spanning events have more complex behavior, which is dependent on the properties of the velocity-strengthening (VS) region at the edges of the fault. Models

with large values of velocity strengthening in their boundary regions do not allow ruptures to propagate much into the velocity-strengthening region, thus containing the rupture area and leading to higher stress drops for a larger amount of slip. Decreasing the velocity strengthening of the boundaries leads to farther rupture propagation into the velocity-strengthening region and thus lower stress drops.

In all models with the thermal pressurization of pore fluids that we have examined, both the smaller and segment-spanning events exhibit increases in breakdown energy consistent with observations. The breakdown energy is the portion of the dissipated energy that governs the event dynamics, analogous to the fracture energy concept of fracture mechanics. The increase in the breakdown energy is due to continuous weakening of the fault with slip, as hypothesized in previous analytical studies.

We also examine the accuracy of seismically estimated breakdown energies G_{SE} for a range of models, by comparing the values computed directly from our fault models and indirectly from seismically available observations. Observationally, G_{SE} is typically obtained as the difference between the seismically estimated available energy ΔW_0 per unit area and radiated energy E_R. This defines the available energy ΔW_{0A} as the sum of the breakdown energy and radiated energy. However, the seismically estimated available energy ΔW_0 is obtained as one-half of the product of the (average) stress drop and (average) final slip, based on a simplified model. As such, we examine the relation between the actual available energy ΔW_{0A} and its seismic estimate ΔW_0 in our models. We find that, as rupture mode changes from crack-like to pulse-like, the actual available energy ΔW_{0A}, becomes increasingly larger that the seismically estimated available energy ΔW_0, due to significant and increasing stress undershoot characteristic of pulse-like ruptures. The extra available energy for more pulse-like ruptures either makes the breakdown energy much larger than its seismically estimated value, or makes the radiated energy much larger than the seismically estimated available energy ΔW_0, or both. In the two latter cases, the radiation ratio η (sometimes called radiation efficiency) between the radiated energy and seismically estimated available energy increases beyond 1, consistent with some observations that were previously thought to be aphysical.

Overall, we find that models with rate-and-state friction and thermal pressurization of pore fluids, when resulting in continuous weakening of fault with slip and crack-like ruptures, produce events with magnitude-invariant stress drops, increases in breakdown energies with the event sizes consistent with observations, radiation ratios consistent with observations, and available energies similar to the ones inferred

seismically. More pulse-like ruptures, which result occasionally in such models and reliably in models that incorporate more severe enhanced weakening motivated by flash heating, have increasingly more significant undershoot and hence extra energy available for breakdown and radiation compared with the seismically estimated available energy. Therefore, current seismic estimates of their breakdown energy and radiation ratio are not reliable. More work is needed to understand the energy budget of pulse-like events obtained in realistic fault models, especially since one of the common paradigms in earthquake physics is that many large events occur as pulse-like ruptures.

PUBLISHED CONTENT AND CONTRIBUTIONS

Stephen Perry, Nadia Lapusta and Valere Lambert (2018). "Magnitude-invariant stress drops and increases in breakdown energy in earthquake sequence simulations on rate-and-state faults with thermal pressurization". In: *[in prep]*.
Perry and Lapusta co-designed the study. Perry performed most of the numerical simulations, analyzed the results, and produced figures. Lambert checked these calculations. Perry and Lapusta interpreted the results and wrote the manuscript. Lambert contributed to the numerical simulations and their analysis and finalizing the manuscript.

Valere Lambert, Stephen Perry and Nadia Lapusta (2018). "Estimates of breakdown energy and radiation efficiency: insights from numerical earthquake source models". In: *[in prep]*.
Lapusta designed the study. Perry performed the numerical simulations, analyzed the results, produced figures, and wrote the draft of the manuscript. Both Perry and Lapusta contributed to interpreting the results and finalizing the the part of the manuscript that relates to crack-like ruptures and some of the pulse-like ruptures. Both Perry and Lapusta contributed to interpreting those results. Lambert will continue to perform simulations for pulse-like ruptures needed to finalize the results. Lambert and Lapusta will finalize the manuscript.

TABLE OF CONTENTS

LIST OF ILLUSTRATIONS

LIST OF TABLES

Chapter 1

INTRODUCTION

Stress drops and breakdown energy are important descriptors of natural earthquakes. Stress drops characterize the average change in stress state before and after the dynamic event (Kanamori and Brodsky, 2004). The stress drop distribution varies along the fault and can be averaged in several different ways in order to produce a single, representative value for an event (Section 2.2). There is a fair amount of scatter in the inferred values of stress drops of natural earthquakes, from about 0.1 MPa up to values around 100 MPa (Kanamori and Brodsky, 2004; Baltay et al., 2011). However inferred values of stress drop are magnitude-invariant; most events have stress drops that fall between 1 MPa and 10 MPa, and this has been observed for events ranging 9 orders of magnitude in moment (Ide and Beroza, 2001). The interpretation and reliability of the stress drops estimates have been actively studied recently, with indications that the current standard methods of estimating stress drops can introduce some significant discrepancies between the actual and inferred stress drops (e.g., Noda et al., 2013; Kaneko and Shearer, 2014; Kaneko and Shearer, 2015). However, the values can be both under- and overestimated, and hence there are no indications at present that the overall magnitude-invariant trend should be questioned.

Breakdown energy, a quantity thought to be the earthquake analog to fracture energy from fracture mechanics, describes the energy consumed near the rupture tip that is necessary to propagate the rupture forward. It is the frictional-rupture generalization of the fracture energy of singular and cohesive zone models of fracture (Palmer and Rice, 1973; Cocco et al., 2004), and is a potentially controlling factor of the dynamics of the rupture front including its velocity and radiative aspects. Breakdown energy is a part of the overall energy budget of a seismic event, with the total strain energy released (ΔW) typically divided into the breakdown energy G, radiated energy E_R, and other dissipation E_D (Kanamori and Rivera, 2006). It is a more straightforward concept for shear stress vs. slip behavior that follows slip weakening during dynamic rupture (Kanamori and Heaton, 2000; Rice, 2000; Kanamori and Brodsky, 2004). It is calculated by taking the area underneath the stress-slip curve for a single event from initiation to its lowest dynamic level of stress and then subtracting off the frictional energy dissipation (Figure 1.3 and Section 2.2.2). Breakdown energy

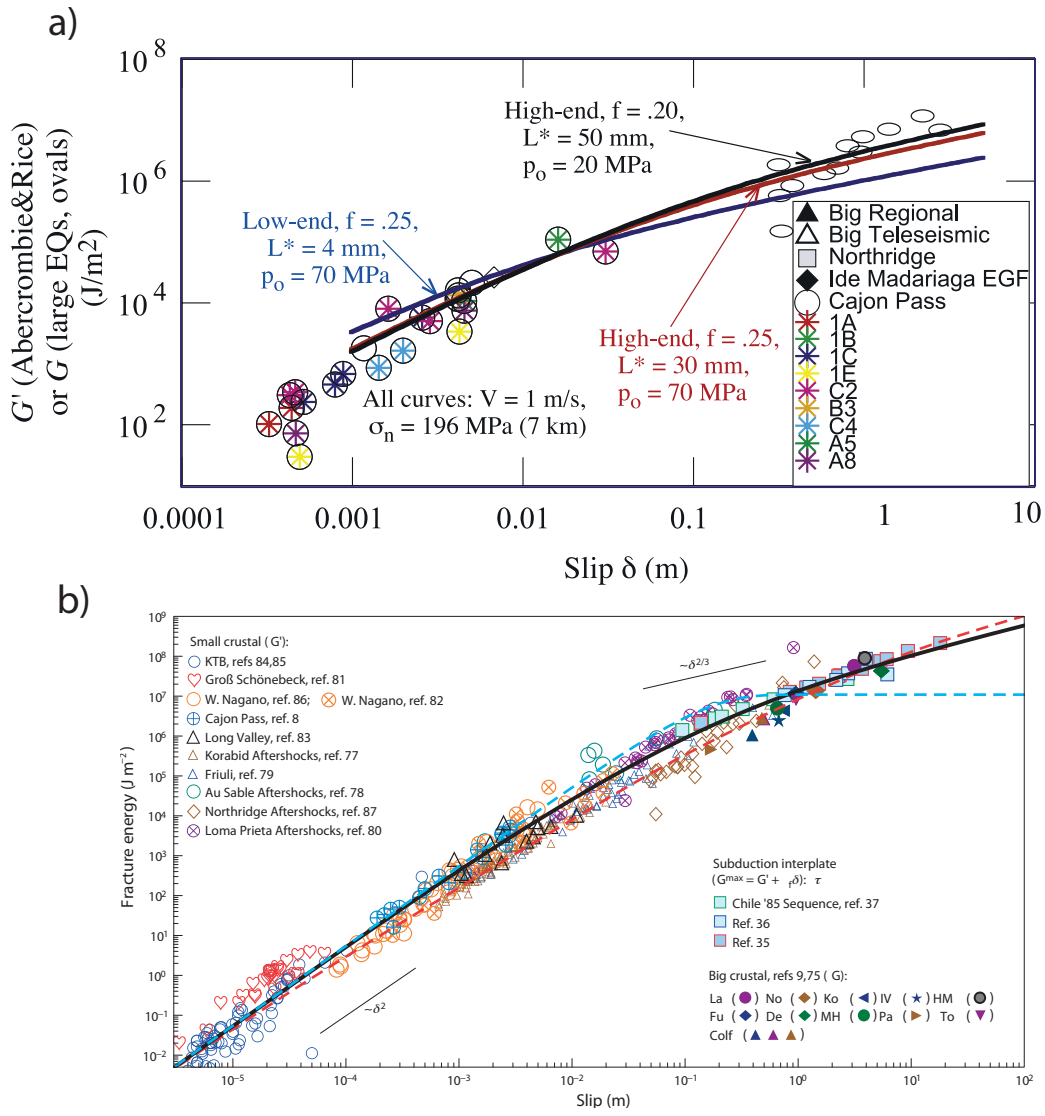

Figure 1.1: Breakdown energies inferred for observed events from the work of a) Rice (2006) and b) Viesca and Garagash (2015). Both show a trend of increasing breakdown energy with increasing event size.

is inferred to increase with the event size in natural earthquakes (Abercrombie and Rice, 2005; Rice, 2006; Viesca and Garagash, 2015). However, our analysis shows (Section 4), that these inferred values may or may not be close to the actual breakdown energies, depending on the mode of the rupture propagation.

Radiation efficiency η, the ratio between the radiated energy E_R and the portion of total strain energy available for radiation and breakdown (available energy), is an important quantity for describing the dynamic character of an earthquake. The

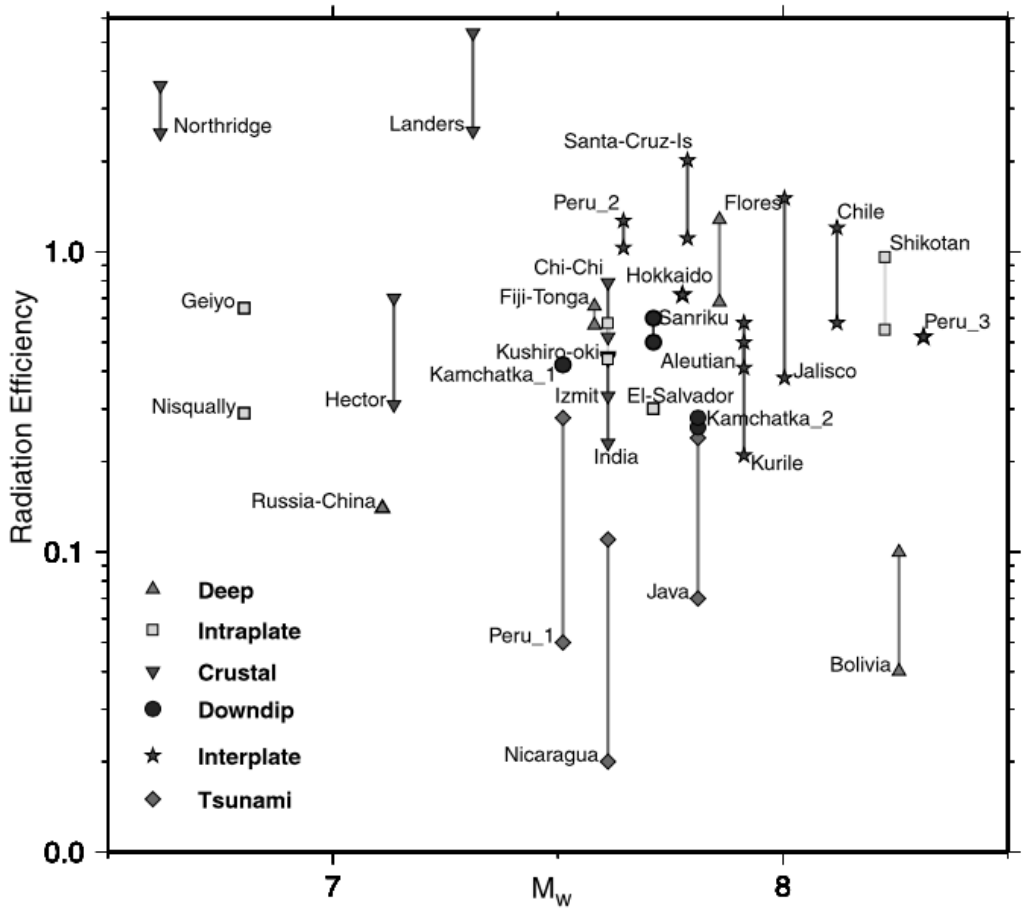

Figure 1.2: Radiation efficiencies inferred for large earthquakes from Venkataraman and Kanamori, 2004. The observed radiation efficiencies most often fall between 0 and 1.

actual available energy is defined as the sum of breakdown energy G and radiated energy E_R. Thus, if $\eta \approx 1$, then radiation is dominating the dynamics of the rupture, and if $\eta << 1$, then the microscopic breakdown process is dominating the dynamics. Breakdown energy cannot be directly measured and thus available energy cannot be directly calculated, even if radiated energy is measured. Using an idealized energy budget with slip-weakening behavior, available energy is able to be seismically estimated using average stress drop and average final slip (Venkataraman and Kanamori, 2004). Observed radiation efficiencies are often between 0-1 with many large events between 0.3 and 0.5 (Ye et al., 2016) and smaller events closer to 0 (Kanamori and Rivera, 2006).

It is clear that during dynamic rupture the fault shear resistance decreases resulting in a stress drop. However the exact nature of this evolution is currently unknown.

Models have been proposed that describe a decrease in shear stress in relation to some other part of the dynamics of the system (e.g., slip, slip rate, etc.). Slip weakening models, where the shear stress decrease depends on the slip accumulated during the event, are commonly used (Ida, 1972; Palmer and Rice, 1973). Linear slip-weakening (LSW) is a simplified model where the stress decreases linearly with slip until it reaches a constant dynamic level (Section 2.3.1).

However, significant insights into the physics of shear resistance during earthquakes have been obtained from the laboratory, showing much richer behavior. It is well established that rate-and-state models explain fault behavior well at slip rates between 10^{-9} – 10^{-3} m/s. Studies using rate-and-state models have successfully reproduced a number of earthquake source observations, including the decay of aftershock rate (Dieterich, 1994), sequences of earthquakes on an actual fault segment (Barbot et al., 2012), and repeating earthquakes (Chen and Lapusta, 2009).

At the same time, many experiments and theoretical studies have shown that enhanced dynamic weakening can be a dominating effect during earthquakes. This type of weakening can be caused by several different mechanisms, many of them due to shear heating. Thermal pressurization is caused by the shear heating of pore fluids during slip. If the fluid is heated quickly enough and not allowed to diffuse away, it will pressurize and relieve normal stress on the fault. This process continues with slip and allows the fault to continue to weaken dynamically as it slips (Sibson, 1973; Andrews, 2002; Rice, 2006). Flash heating is another effect that allows rapid weakening due to micro contacts between the two sides of the fault melting at small scales and rapidly decreasing the effective friction coefficient (Rice, 1999; Goldsby and Tullis, 2011; Passelegue et al., 2014). Thermal decomposition allows the rock to undergo a chemical change during heating that can lead to the production of fluid and then further thermal pressurization of this fluid (even if the fault is dry beforehand) (Han et al., 2007; Sulem and Famin, 2009). Other weakening mechanisms have been proposed, such as macroscopic melting and silica gel formation (Brodsky and Kanamori, 2001; Goldsby and Tullis, 2002; Di Toro et al., 2004). Models with dynamic weakening have also been successful in producing fault operation at low overall prestress and low heat production (Lapusta and Rice, 2003; Rice, 2006; Noda et al., 2009a) as supported by several observations (Brune et al., 1969; Zoback et al., 1987; Hickman and Zoback, 2004; Williams et al., 2004). Different dynamic weakening mechanisms produce different weakening behaviors, but here we focus on thermal pressurization as a representative dynamic weakening mechanism that

can lead to continuous fault weakening with earthquake-source slip. We also add flash heating (Section 4) to explore the effect of strong initial dynamic weakening and its potential to create events with more pulse-like behavior.

There have been several attempts to reconcile these dynamic weakening effects with some of the observed quantities in natural earthquakes. The work of Rice, 2006, Viesca and Garagash, 2015 and others showed that thermal pressurization of pore fluids can explain the inferred increase in breakdown energy with the increasing event size. This has been shown using simplified theoretical arguments. Furthermore, it is not clear how to reconcile enhanced dynamic weakening with magnitude-invariant stress drops.

Here, we use fully dynamic simulations of earthquake sequences to investigate several important issues related to laboratory-derived earthquake physics and relevant observations, such as: Can dynamic weakening be compatible with magnitude-invariant stress drops while also maintaining increasing breakdown energy with increasing event size? How robust are seismic observations of available energy and breakdown energy to different modes of earthquake rupture and what implications do these measurements have for interpreting rupture mode of observed events?

Linear slip-weakening friction laws are relatively easy to reconcile with magnitude-invariant stress drops, provided the peak shear resistance is within 1-2 stress drops from the dynamic resistance, as commonly assumed. As long as the total slip exceeds the slip-weakening distance D_c, the fault weakens with slip down to a constant dynamic level of stress regardless of the amount of total slip. As events grow larger, the amount of total slip increases, but the dynamic level of shear stress does not change. Since the initial stress must fall somewhere between the peak stress and the dynamic level of shear stress, as long as the peak shear resistance is within several stress drops of the dynamic stress level, stress drops for small and large earthquakes would be nearly constant (Figure 1.3a). However, another consequence is that breakdown energies remain constant for events of different sizes, at least for constant friction parameters. The standard rate-and-state friction law results in shear stress evolution with slip, during dynamic rupture, similar to linear slip weakening (Cocco and Bizzarri, 2002; Lapusta and Liu, 2009; Section 2.3.1). As such, we expect the same trends with both breakdown energy and stress drop, as we find in our simulations (Chapter 2).

It is less clear how enhanced dynamic weakening during events affects stress drops. We present two possibilities in Figures 1.3b and 1.3c. First is the potentially more

intuitive view of the process. Let us assume that smaller and larger events nucleate at nearly the same level of average prestress. The smaller event has less slip and thus weakens a smaller amount. This results in a smaller breakdown energy (the dotted region) and a higher final stress. The larger event weakens more, and has a larger breakdown energy and lower final stress. In this scenario, larger events would have systematically larger stress drops and larger breakdown energy (Figure 1.3b).

However, this intuitive scenario may be incorrect. Indeed, both smaller and larger events should *nucleate* at locations with similar levels of prestress. But we must consider the average initial stress of all points involved in the rupture, not just those involved in nucleation. Smaller events would tend to have smaller rupture areas and therefore have average initial stresses that match more closely to the prestresses of the nucleation zone, while larger events propagate further, dynamically weaken more (which they must because they become large), and may be able to propagate over areas of much less favorable (lower) prestress conditions. This means that the average initial stress for larger events can be lower than that for smaller events. Larger events would dynamically weaken more and arrest at a lower average final stress, but they would also have occurred with lower average initial stress. Thus, the average stress drop can be similar for smaller and larger events (Figure 1.3c). However, the observed increase of the breakdown energy with event size is still preserved.

We indeed find that the second scenario prevails in our simulations (Chapter 3) reconciling enhanced dynamic weakening with magnitude-invariant stress drops. Larger events have both lower average initial and final stresses in our models. Why the difference is magnitude-invariant, e.g., why the average initial shear stress decreases by about the same amount as the average final stress, and not systematically more or less, requires further study.

Furthermore, we find that the properties of the velocity-strengthening areas can have a profound impact on the stress drop of events that appreciably propagate into these regions, mostly segment-spanning events in our case. Models with large values of velocity-strengthening do not allow ruptures to propagate much into the velocity-strengthening region, thus leading to higher stress drops. Whereas, models with smaller values of velocity-strengthening allow farther propagation and thus lower stress drops.

Note that here we follow the assumption that most of the breakdown energy occurs on the shearing surface (e.g., Rice, 2006; Viesca and Garagash, 2015). While it is clear

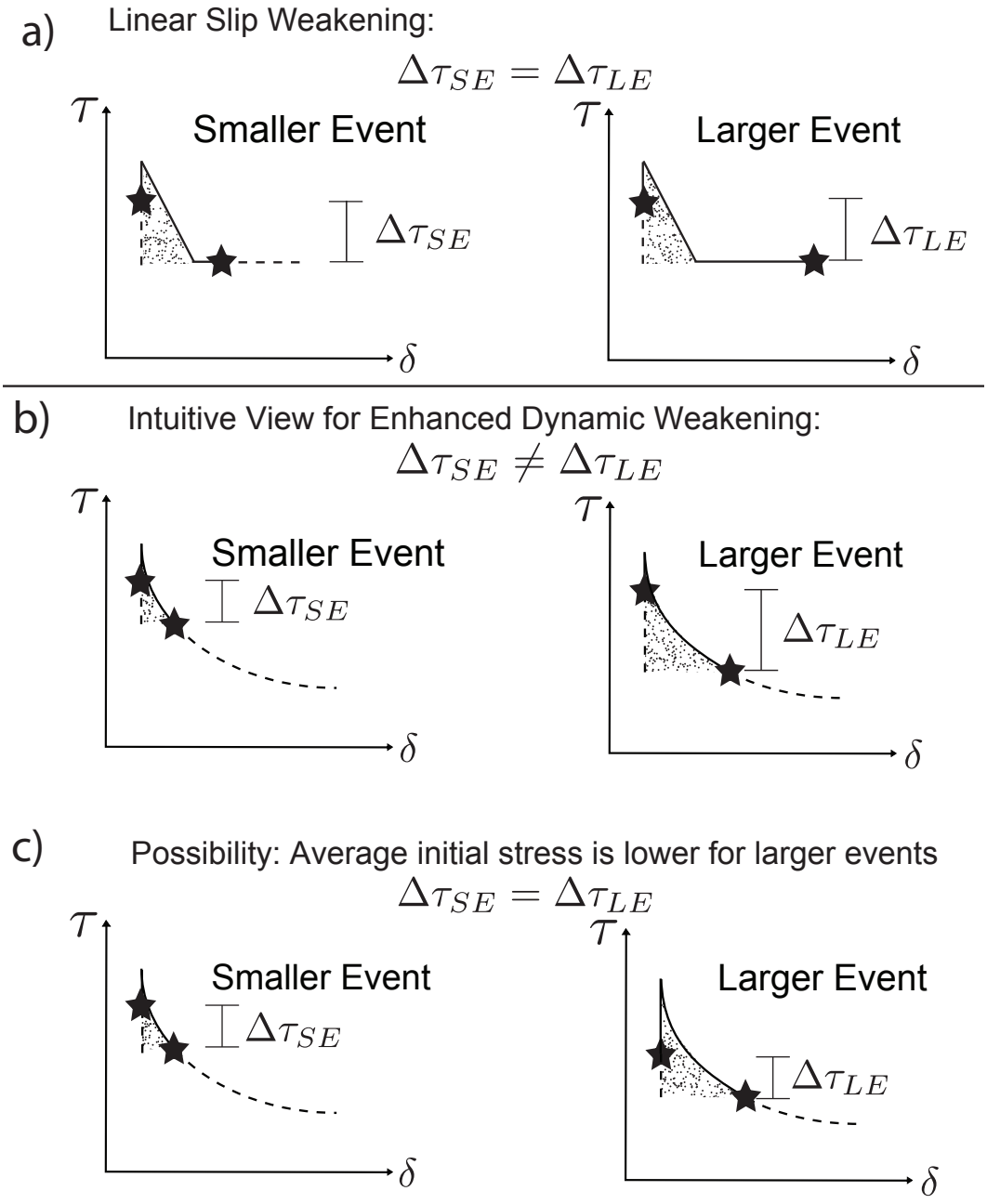

Figure 1.3: Stress drop and breakdown energy implications for both linear slip-weakening and rate-and-state friction with additional dynamic weakening. a) In linear slip weakening laws, smaller and larger events weaken to the same dynamic levels of shear resistance over the same slip. This leads to the same breakdown energies (dotted region) and similar stress drop (marked with stars). b) If smaller and larger events both nucleate at the same levels of prestress, and larger events weaken more than small events, one expects both larger breakdown energies and larger stress drops for larger events. c) However, if dynamic weakening allows larger events to propagate into areas of lower stress, then the average prestress of these events may be lower than for smaller events. In this case, breakdown energies still increase with event size, but stress drops may be magnitude-invariant.

that some energy is dissipated in off-fault damage (Andrews, 2005), those amounts may be negligible compared to seismic estimates of breakdown energy (Chester et al., 2005). To consider the relative importance of the off-fault dissipation is beyond the scope of this work.

We also examine the accuracy of seismically estimated breakdown energies G_{SE} for a range of models using standard rate-and-state friction laws as well as several with enhanced dynamic weakening due to thermal pressurization and flash heating. We compare the values computed directly from our fault models with inferred values taken indirectly from seismically available observations. Breakdown energy cannot be measured directly and is typically found through the use of available energy, the portion of total strain energy release available for breakdown and radiation. Thus, the available energy ΔW_{0A} is defined as the sum of the breakdown energy G and radiated energy E_R. However, the seismically estimated available energy ΔW_0, based on an idealized model of the earthquake energy budget, is dependent on only the average stress drop of the event and the average final slip. Seismically estimated breakdown energy G_{SE} is typically obtained as the difference between the seismically estimated available energy ΔW_0 per unit area and radiated energy E_R, and so we focus on the relation between the actual available energy ΔW_{0A} and the seismically estimated available energy ΔW_0.

We will see (Chapter 4) that rupture behavior can play an important role in the accuracy of measuring available energy and can range from crack-like to pulse-like (Heaton, 1990; Zheng and Rice, 1998; Xiao Lu and Rosakis, 2007; Noda et al., 2009b). Crack-like ruptures behave like a growing opening crack, but in shear, where nearly all points along the ruptured area, once they start slipping, continue their slip until the overall rupture arrests. Thus, the local slip duration on the fault is comparable to the overall rupture duration for most points. Pulse-like ruptures exhibit a propagating slip pulse; each point along the fault slips for an amount of time that is short compared to the overall rupture duration.

Associated with these two types of rupture modes are different shear stress evolutions as the events arrest. The dynamic level of shear stress is determined by the constitutive laws governing friction on the fault, and these describe the evolution of stress with slip. However, the final level of shear stress is determined by the final slip distribution and is not directly dependent on the dynamic level of shear stress. Therefore, the dynamic level of shear stress from the constitutive laws need not match the final shear stress consistent with the final slip on the fault. For crack-like

events, often more stress is released than the dynamic level has suggested. Thus a decrease in shear stress at final slip, termed stress overshoot, is often associated with crack-like ruptures. However, the stress overshoot is often small relative to the average stress change on the fault.

For pulse-like events, the final stress change is determined by the final slip over the fault dimension along with the elastic constants of the system. However, the dynamics of this pulse do not correlate with the final stress. Once slip at a portion of the fault arrests, slip elsewhere reloads the points and thus a substantial increase in shear stress enabled by fault restrengthening. Thus, an increase in shear stress as the event arrests, termed stress undershoot, is associated with healing and thus slip pulses. This undershoot may be large relative to the average stress drop on the fault if there is significant restrengthening experienced as the event arrests and the overall dynamic stress levels are low.

The stress overshoot/undershoot is unaccounted for in the typically used simplified energy budget (Venkataraman and Kanamori, 2004, Abercrombie and Rice, 2005, Rice, 2006, Ye et al., 2016), including seismically estimated available energy, and thus can lead to a discrepancy between actual available energy ΔW_{0A} and seismically estimated available energy ΔW_0, as well as other quantities of interest. The importance of the overshoot and undershoot for some aspects of the energy balance has been recognized in several studies (N. M. Beeler and Hickman, 2003; Noda et al., 2013; Viesca and Garagash, 2015).

In our simulations, we indeed find that, for crack-like ruptures, there is a slight overshoot and, as the result, the actual available energy ΔW_{0A} is slightly smaller than the seismically estimated energy ΔW_0 (Chapter 4). As the rupture mode changes from crack-like to pulse-like, the actual available energy ΔW_{0A} becomes increasingly larger than the seismically estimated available energy ΔW_0, due to increasingly larger stress undershoot. Both breakdown energy and radiated energy increase beyond seismically estimated available energy ΔW_0, leading to the radiation ratios η beyond 1, and seismically estimated breakdown energies G_{SE} that are negative. This is consistent with observations previously thought to be aphysical.

We conclude in Chapter 5 with our overall conclusions and important questions for future work.

References

Abercrombie, Rachel E. and James R. Rice (2005). "Can observations of earthquake scaling constrain slip weakening?" In: *Geophysical Journal International* 162, pp. 406–424. DOI: 10.1111/j.1365-246X.2005.02579.x.

Andrews, D. J. (2005). "Rupture dynamics with energy loss outside the slip zone". In: *Journal of Geophysical Research* 110. DOI: 10.1029/2004JB003191.

Andrews, DJ (2002). "A fault constitutive relation accounting for thermal pressurization of pore fluid". In: *Journal of Geophysical Research: Solid Earth* 107.B12.

Baltay, Annemarie, Satoshi Ide, German Prieto, and Gregory Beroza (2011). "Variability in earthquake stress drop and apparent stress". In: *Geophysical Research Letters* 38. DOI: 10.1029/2011GL046698.

Barbot, Sylvain, Nadia Lapusta, and Jean-Philippe Avouac (2012). "Under the hood of the earthquake machine: Toward predictive modeling of the seismic cycle". In: *Science* 336.6082, pp. 707–710.

Brodsky, Emily E and Hiroo Kanamori (2001). "Elastohydrodynamic lubrication of faults". In: *Journal of Geophysical Research: Solid Earth* 106.B8, pp. 16357–16374.

Brune, James N, Thomas L Henyey, and Robert F Roy (1969). "Heat flow, stress, and rate of slip along the San Andreas fault, California". In: *Journal of Geophysical Research* 74.15, pp. 3821–3827.

Chen, Ting and Nadia Lapusta (2009). "Scaling of small repeating earthquakes explained by interaction of seismic and aseismic slip in a rate and state fault model". In: *Journal of Geophysical Research* 114. DOI: 10.1029/2008JB005749.

Chester, Judith S, Frederick M Chester, and Andreas K Kronenberg (2005). "Fracture surface energy of the Punchbowl fault, San Andreas system". In: *Nature* 437.7055, p. 133.

Cocco, M, A Bizzarri, and E Tinti (2004). "Physical interpretation of the breakdown process using a rate-and state-dependent friction law". In: *Tectonophysics* 378.3-4, pp. 241–262.

Cocco, Massimo and Andrea Bizzarri (2002). "On the slip-weakening behavior of rate- and state dependent constitutive laws". In: *Geophysical Research Letters* 29.11. DOI: 10.1029/2001GL013999.

Di Toro, Giulio, David L Goldsby, and Terry E Tullis (2004). "Friction falls towards zero in quartz rock as slip velocity approaches seismic rates". In: *Nature* 427.6973, pp. 436–439.

Dieterich, James (1994). "A constitutive law for rate of earthquake production and its application to earthquake clustering". In: *Journal of Geophysical Research: Solid Earth* 99.B2, pp. 2601–2618.

Goldsby, David L and Terry E Tullis (2002). "Low frictional strength of quartz rocks at subseismic slip rates". In: *Geophysical Research Letters* 29.17.

Goldsby, David L. and Terry E. Tullis (2011). "Flash Heating Leads to Low Frictional Strength of Crustal Rocks at Earthquake Slip Rates". In: *Science* 334, pp. 216–218. DOI: 10.1126/science.1207902.

Han, Raehee, Toshihiko Shimamoto, Jun-ichi Ando, and Jin-Han Ree (2007). "Seismic slip record in carbonate-bearing fault zones: An insight from high-velocity friction experiments on siderite gouge". In: *Geology* 35.12, pp. 1131–1134.

Heaton, Thomas H (1990). "Evidence for and implications of self-healing pulses of slip in earthquake rupture". In: *Physics of the Earth and Planetary Interiors* 64.1, pp. 1–20.

Hickman, Stephen and Mark Zoback (2004). "Stress orientations and magnitudes in the SAFOD pilot hole". In: *Geophysical Research Letters* 31.15.

Ida, Yoshiaki (1972). "Cohesive force across the tip of a longitudinal-shear crack and Griffith's specific surface energy". In: *Journal of Geophysical Research* 77.20, pp. 3796–3805.

Ide, Satoshi and Gregory C. Beroza (2001). "Does apparent stress vary with earthquake size?" In: *Geophysical Research Letters* 28.17, pp. 3349–3352.

Kanamori, Hiroo and Emily E Brodsky (2004). "The Physics of Earthquakes". In: *Reports on Progress in Physics* 67.8, pp. 1429–1496. DOI: 10.1088/0034-4885/67/8/R03.

Kanamori, Hiroo and Thomas H. Heaton (2000). "Microscopic and macroscopic physics of earthquakes". In: *Geocomplexity and the Physics of Earthquakes*, pp. 147–163.

Kanamori, Hiroo and Luis Rivera (2006). "Energy Partitioning during an earthquake". In: *Earthquakes: Radiated energy and the physics of faulting*, pp. 3–13.

Kaneko, Y. and P. M. Shearer (2014). "Seismic source spectra and estimated stress drop derived from cohesive-zone models of circular subshear rupture." In: *Geophysical Journal International* 197.2, pp. 1002–1015.

– (2015). "Kaneko, Y., and P. M. Shearer. "Variability of seismic source spectra, estimated stress drop, and radiated energy, derived from cohesive-zone models of symmetrical and asymmetrical circular and elliptical ruptures." In: *Journal of Geophysical Research: Solid Earth* 120.2, pp. 1053–1079.

Lapusta, N and JR Rice (2003). "Low-heat and low-stress fault operation in earthquake models of statically strong but dynamically weak faults". In: *AGU FAll Meeting Abstracts*.

Lapusta, Nadia and Yi Liu (2009). "Three-dimensional boundary integral modeling of spontaneous earthquake sequences and aseismic slip". In: *Journal of Geophysical Research* 114, B09303. DOI: 10.1029/2008JB005934.

N. M. Beeler, TF. Wong and S. H. Hickman (2003). "On the expected relationships among apparent stress, static stress drop, effective shear fracture energy, and efficiency". In: *Bulletin of the Seismological Society of America* 93.3, pp. 1381–1389.

Noda, Hiroyuki, Eric M Dunham, and James R Rice (2009a). "Earthquake ruptures with thermal weakening and the operation of major faults at low overall stress levels". In: *Journal of Geophysical Research: Solid Earth* 114.B7.

Noda, Hiroyuki, Eric M. Dunham, and James R. Rice (2009b). "Earthquake ruptures with thermal weakening and the operation of major faults at low overall stress levels". In: *Journal of Geophysical Research* 114, B07302. DOI: 10.1029/2008JB006143.

Noda, Hiroyuki, Nadia Lapusta, and Hiroo Kanamori (2013). "Comparison of average stress drop measures for ruptures with heterogeneous stress change and implications for earthquake physics". In: *Geophysical Journal International*. DOI: 10.1093/gji/ggt074.

Palmer, Andrew Clennel and JR Rice (1973). "The growth of slip surfaces in the progressive failure of over-consolidated clay". In: *Proceedings of the Royal Society of London A: Mathematical, Physical and Engineering Sciences* 332.1591, pp. 527–548.

Passelegue, Francois X., David L. Goldsby, and Olivier Fabbri (2014). "The influence of ambient fault temperature on flash-heating phenomena". In: *Geophysical Research Letters* 41, pp. 828–835. DOI: 10.1002/2013GL058374.

Rice, James R. (2006). "Heating and weakening of faults during earthquake slip". In: *Journal of Geophysical Research* 111, B05311. DOI: 10.1029/2005JB004006.

Rice, JR (1999). "Flash heating at asperity contacts and rate-dependent friction". In: *Eos Trans. AGU* 80.46, F471.

– (2000). "Fracture energy of earthquakes and slip-weakening rupture parameters". In: *EOS, Trans. Am. geophys. Un., Fall Meeting Suppl* 81.48, F1227.

Sibson, R. H. (1973). "Interactions between temperature and pore-fluid pressure during earthquake faulting and a mechanism for partial or total stress relief." In: *Nature* 243.126, pp. 66–68.

Sulem, Jean and Vincent Famin (2009). "Thermal decomposition of carbonates in fault zones: Slip-weakening and temperature-limiting effects". In: *Journal of Geophysical Research: Solid Earth* 114.B3.

Venkataraman, Anupama and Hiroo Kanamori (2004). "Observational constraints on the fracture energy of subduction zone earthquakes". In: *Journal of Geophysical Research: Solid Earth* 109.B5.

Viesca, Robert C. and Dmitry I. Garagash (2015). “Ubiquitous weakening of faults due to thermal pressurization”. In: *Nature Geoscience* 8, pp. 875–879. DOI: 10.1038/NGEO2554.

Williams, Colin F, Frederick V Grubb, and S Peter Galanis (2004). “Heat flow in the SAFOD pilot hole and implications for the strength of the San Andreas Fault”. In: *Geophysical Research Letters* 31.15.

Xiao Lu, Nadia Lapusta and Ares J. Rosakis (2007). “Pulse-like and crack-like ruptures in experiments mimicking crustal earthquakes.” In: *Proceedings of the National Academy of Sciences* 104.48, pp. 18931–18936.

Ye, Lingling, Thorne Lay, Hiroo Kanamori, and Luis Rivera (2016). “Rupture characteristics of major and great (Mw 7.0) megathrust earthquakes from 1990 to 2015: 1. Source parameter scaling relationships”. In: *Journal of Geophysical Research: Solid Earth* 121.2, pp. 826–844.

Zheng, Gutuan and James R. Rice (1998). “Conditions under which velocity-weakening friction allows a self-healing versus a cracklike mode of rupture.” In: *Bulletin of the Seismological Society of America* 88.6, pp. 1466–1483.

Zoback, Mark D et al. (1987). “New evidence on the state of stress of the San Andreas fault system”. In: *Science* 238.4830, pp. 1105–1111.

Chapter 2

ESTIMATES OF STRESS DROPS AND BREAKDOWN ENERGIES FOR MODELS WITH STANDARD RATE-AND-STATE FRICTION

2.1 Fault Models and Simulated Events

2.1.1 Model of a seismogenic region with sequences of earthquakes

Our simulations are conducted following the methodological developments of Lapusta et al., 2000 and Noda and Lapusta, 2010. We consider a mode III, two-dimensional (2-D) model with a 1-D fault embedded into a 2-D uniform, isotropic, elastic medium (Figure 2.1a). The earthquake sequences on the fault are simulated in their entirety: the nucleation process, the dynamic rupture propagation, postseismic slip that follows the event, and the interseismic period between events that can last up to tens or hundreds of years (Figure 2.1b). In all models, the laboratory-derived rate-and-state friction (section 2.1.2) operates on the fault. Our fault setup (Figure 2.1a) consists of a 1D fault composed of a velocity-weakening (VW) region surrounded by velocity-strengthening (VS) regions. The fault slip at the plate rate (V_{pl} = 10^{-9} m/s) is prescribed at the edges of the model. We begin with a standard rate-and-state model, but then add thermal pressurization of pore fluids (section 3). Parameters for the specific models are listed in Tables 2.1 and 2.2.

While many events arrest within the VW region, some span the entire VW region (Figure 2.1b). We will refer to the events that span the entire VW region as "complete rupture" events, and those that arrest within the VW region as "partial rupture" events.

2.1.2 Rate-and-state friction

We use the laboratory derived rate-and-state laws with the aging law proposed by Dieterich, 1979 and Ruina, 1983:

$$\tau = (\sigma - p)f = (\sigma - p)\left[f_* + a\ln\frac{V}{V_*} + b\ln\frac{V_*\theta}{L}\right], \tag{2.1}$$

$$\frac{d\theta}{dt} = 1 - \frac{V\theta}{L}, \tag{2.2}$$

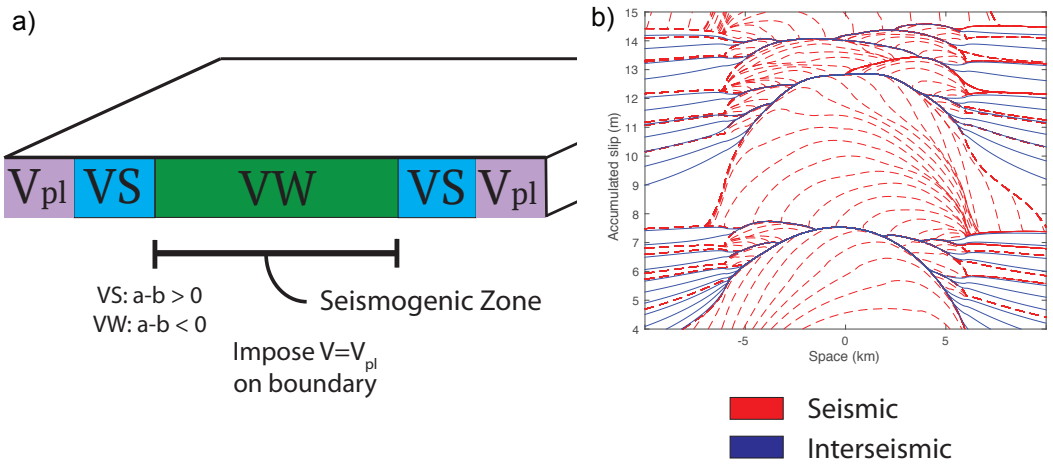

Figure 2.1: a) Model setup for our simulations. The fault is composed of a velocity-weakening (VW) seismogenic section surrounded by two velocity-strengthening (VS) patches. Outside of these regions, relative sliding with the plate rate is prescribed. b) A portion (15 events) of a simulation with the standard rate-and-state friction ($L = 250$ μm) is plotted showing accumulated slip along the fault through time. Seismic events are illustrated by red dashed lines plotted every 0.1 s when slip rate V exceeds 0.1 m/s. Interseismic slip is plotted in solid blue lines every 10 years.

where σ is (constant in time) normal stress, τ is the shear stress, f is the friction coefficient, V is the slip velocity, p is the pore pressure, L is the characteristic slip distance, θ is the state variable, f_* is the friction coefficient corresponding to a reference slip rate V_*, and a and b are constitutive parameters. At steady state (constant slip velocity), the values of τ and θ evolve to be their steady-state values τ_{ss} and θ_{ss} given by:

$$\theta_{ss}(V) = \frac{L}{V}, \tag{2.3}$$

$$\tau_{ss} = (\sigma - p)\left[f_* + (a-b)\ln\frac{V}{V_*}\right]. \tag{2.4}$$

These steady-state relations show that the difference between the parameters a and b controls the fault behavior at steady state. If $(a-b) > 0$ then we have velocity-strengthening (VS) behavior where increases in velocity give increases in shear resistance. This leads to stable sliding on the fault. If $(a-b) < 0$ then we have velocity-weakening (VW) behavior. In this case, an increase in velocity leads to a decrease in shear resistance. This makes these regions of the fault potentially

seismogenic (Rice and Ruina, 1983, Rice et al., 2001, Rubin and Ampuero, 2005). Parameters for our models are shown in Tables 2.1 and 2.2.

Table 2.1: Parameters for All Simulations

Parameter	Symbol	Value
Loading slip rate	V_{pl}	10^{-9} m/s
Shear wave speed	c_s	3464 m/s
Shear modulus	μ	32 GPa
Reference slip velocity	V_0	10^{-6} m/s
Reference friction coefficient	f_0	0.6

Table 2.2: Parameters for R+S Models

Parameter	Symbol	Standard R+S Model
Fault length along strike	λ	36 km
VW region length (total)	W_{VW}	6 km
VS region length (total)	W_{VS}	24 km
Effective normal stress	$\bar{\sigma} = (\sigma - p)$	50 MPa
Rate-and-state direct effect (VS)	a	0.019
Rate-and-state evolution effect (VS)	b	0.015
Rate-and-state direct effect (VW)	a	0.01
Rate-and-state evolution effect (VW)	b	0.015
Characteristic slip	L	0.125 mm - 4 mm
Cell size	Δx	0.625 m - 20 m
Cohesive Zone	Λ_0	5 m - 150 m
Nucleation Size (Rice & Ruina, 1985)	h^*_{RR}	12 m - 400 m
Nucleation Size (Rubin & Ampuero, 2005)	h^*_{RA}	30 m - 980 m

2.1.3 Representative Simulated Events

Our simulations produce sequences of dynamic events together with interseismic creep, including aseismic nucleation processes (Figure 2.1b). However, here we focus on the properties of individual dynamic events. A sample dynamic event from our simulations is shown in Figures 2.2. In general, both slip throughout the event and final slip vary along the fault. The spatially varying initial and final shear stress distributions along the fault lead to a stress drop distribution that varies along the fault. Most of the ruptured area experiences a decrease in shear stress during the event, but both edges of the ruptured area in each of the events show an increase in stress (and hence negative stress drop). The shear stress vs. slip evolution along the fault is illustrated for three representative locations. Locations near the nucleation region experience a small coseismic stress drop and slip an amount comparable to the average. Much of the stress change at these points is achieved aseismically,

during nucleation. Points near the middle of the ruptured area show the expected increase in stress to a peak value, followed by a drop, controlled by our rate-and-state laws, down to some near constant (Figure 2.2) dynamic value. Where the event arrests, points only slip a small amount and do not completely weaken down to the expected dynamic level of shear stress.

Observations of natural earthquakes cannot resolve these fine variations in stress, slip, slip rate, etc. at all points along the fault as we are able to do in our simulations. Thus, natural events are often described by a single, "average" value for stress drop and average final slip. In the next sections, we discuss the various ways of condensing heterogeneous slip and stress distributions into average values for the seismic events.

2.2 Static Stress Drops and Breakdown Energy

2.2.1 Calculating Average Static Stress Drops $\overline{\Delta\tau}$

We follow the averaging methodologies described in Noda et al., 2013 modified to fit our two-dimensional model, since our relevant variables are scalar fields rather than vector fields. The initial distribution of shear traction on the fault before an earthquake is denoted by $\tau^i(x)$. An earthquake produces a slip distribution $\delta(x)$ and the traction along the fault changes to $\tau^f(x)$. The stress drop distribution is defined as:

$$\Delta\tau(x) = \tau_i(x) - \tau_f(x). \tag{2.5}$$

Averaging of Stress Drop Distribution Based on Seismic Moment

Seismically estimated values of average stress drop are based on the seismic moment M_0 of the event as well as the fault dimensions; the following formula is typically used (Kanamori and Anderson, 1975):

$$\overline{\Delta\tau}_M = C\frac{M_0}{\rho^3} = C\frac{M_0}{A^{3/2}}, \tag{2.6}$$

where A is the ruptured area, $\rho = A^{1/2}$ is the characteristic spatial dimension, and C depends on the shape and aspect ratio of the ruptured domain: $C = 2.44$ for a circular ruptured area and increases for rectangular areas with larger aspect ratios (Noda et al., 2013).

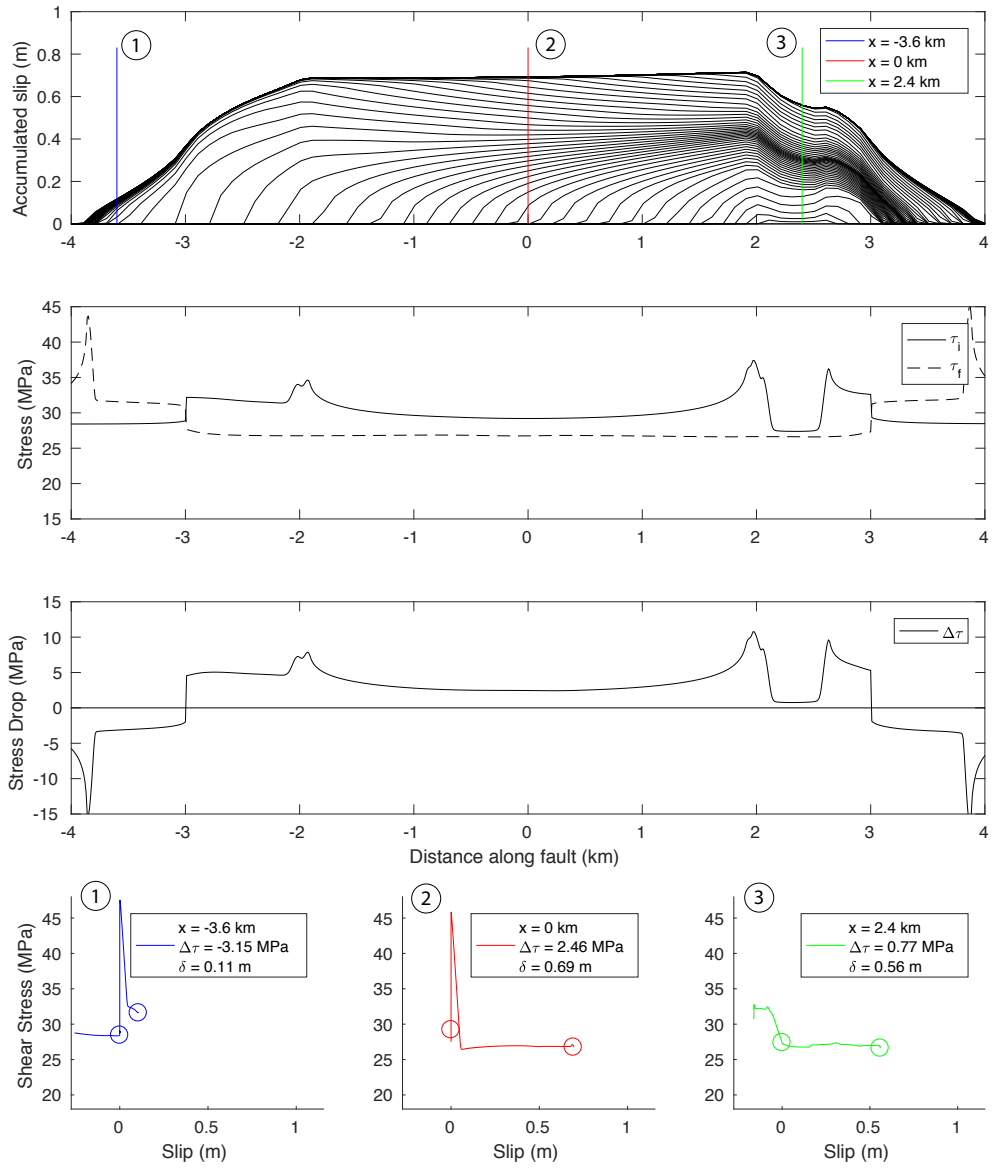

Figure 2.2: A sample event for the standard rate-and-state model. Accumulated slip is plotted every 0.1 s (Row 1). Initial and final stress (Row 2), and stress drop distributions (Row 3) are shown along the fault. The stress vs. slip evolution at three example points illustrate different behaviors along the fault (Row 4). Initial and final stresses during the event are marked (open circles) for each point and some previous slip history is also shown preceding the initial stress marker. The green point shows the evolution for a point in the nucleation zone, the blue point is in the region where the event arrests, and the red point shows behavior of a well-established rupture (the majority of the ruptured points experience this behavior). Note that this event is crack-like and the final stress is nearly equal to the dynamic level of stress for the three representative points.

If the actual stress drop is uniform over the ruptured domain Σ, then $\overline{\Delta\tau}_M$ is exactly equal to that value. However, as we have shown in our example events (section 2.3), the stress drop across the fault is heterogeneous and given by the distribution $\Delta\tau(x)$. In this case, $\overline{\Delta\tau}_M$ is a weighted average of $\Delta\tau(x)$. This average is weighted by the (elliptic) slip distribution E^{12} that gives a uniform stress drop over the same ruptured domain (Madariaga, 1979):

$$\overline{\Delta\tau}_M = \frac{\int_\Sigma \Delta\tau E^{12} d\Sigma}{\int_\Sigma E^{12} d\Sigma}. \tag{2.7}$$

Spatial Averaging of Stress Drop

The spatially averaged stress drop can be expressed as the integral of the stress drop of all ruptured points along the fault divided by the ruptured domain Σ:

$$\overline{\Delta\tau}_A = \frac{\int_\Sigma \Delta\tau d\Sigma}{\int_\Sigma d\Sigma}. \tag{2.8}$$

The stress change at every point has equal weighting of one in this averaging method, unlike $\overline{\Delta\tau_M}$ where E^{12} weights points differently along the fault. Similarly to $\overline{\Delta\tau}_M$, $\overline{\Delta\tau}_A$ depends only on points in the ruptured domain. Considering the entire fault can result in severely underestimating the average stress drop of the event.

The ruptured domain Σ is defined as the region with non-zero slip (which is a line for our model, but a 2D area in general):

$$\Sigma = \{x \in L | \delta(x) > 0\}. \tag{2.9}$$

However, it is difficult to precisely determine Σ for observed events due to non-uniqueness and smoothing when finding a solution. Furthermore, in our models, the fault is prescribed to creep outside the locked, velocity-weakening region, and thus there is small non-zero slip everywhere on the fault during every event. It is appropriate to only consider points where the inertial term becomes significant, but there is no exact quantitative criterion to define that, so we instead approximate this by defining the ruptured domain Σ to consist of locations that exceed a slip rate of 0.1 m/s during the event:

$$\Sigma = \{x \in L | V(x) > 0.1 \text{ m/s}\}. \tag{2.10}$$

Altering the seismic velocity threshold may change the effective rupture size. However, there is a sharp falloff in slip rate outside the ruptured area down to the creeping rate many orders of magnitude below the seismic slip rate. Thus, changing this threshold by even an order of magnitude does not change the rupture size appreciably.

Averaging of Stress Drop Distribution Based on Energy Considerations

The work of Noda and Lapusta, 2012 and Noda et al., 2013 introduced a third method of averaging $\Delta\tau(x)$ that is consistent with energy partitioning. This method conserves both the total strain energy released ΔW as well as the dissipated energy E_D as will be discussed later (Section 2.2.2). Here, the final slip distribution $\delta_f(x)$ is used as the weighting function:

$$\overline{\Delta\tau}_E = \frac{\int_\Sigma \Delta\tau\delta_f(x)d\Sigma}{\int_\Sigma \delta_f(x)d\Sigma}. \tag{2.11}$$

In this method, the ruptured domain is implicitly defined by the slip distribution $\delta_f(x)$.

The three averaging methods (2.7 - 2.8) and (2.11) give similar but not identical results for the average stress drop for a given event. Noda et al., 2013 proved that $\overline{\Delta\tau}_E \geq \overline{\Delta\tau}_M$ and observed that $\overline{\Delta\tau}_M \geq \overline{\Delta\tau}_A$ in their simulations. Given that computing seismic moment on our 1D faults requires additional assumptions of rupture aspect ratio and shape, we focus on computing the energy based stress drop $\overline{\Delta\tau}_E$ and the spatially averaged stress drop $\overline{\Delta\tau}_A$ in this study.

2.2.2 Calculation of Breakdown Energy G in Simulations

In our dynamic simulations, the slip and stress evolution is determined at every point along our fault at all times. As such, we are able to calculate the breakdown energy directly in our model. This can be done using two methods: (I) integrating the breakdown energies along the fault for all ruptured points and (II) constructing a representative average curve for the event and using it to calculate breakdown energy.

In the earthquake energy budget per unit area, illustrated in Figure 2.3, the total strain energy released $\Delta W/A$ is partitioned into dissipated energy E_D/A, which is the area underneath the stress-slip curve, and radiated energy E_R/A:

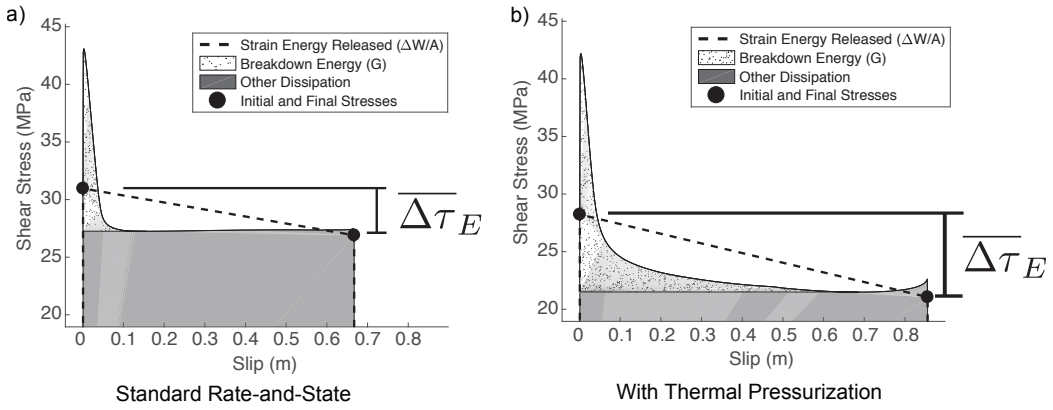

Figure 2.3: Illustration of the earthquake energy budget and average stress drop using average shear stress vs. slip curves. (a) The average curve for the single event from a standard rate-and-state model from Figure 2.2. The shear resistance weakens to a nearly constant dynamic value. (b) The average curve for the single event with enhanced dynamic weakening from Figure 3.1. The fault continues to weaken by more than an additional 5 MPa as it accumulates slip, leading to a larger breakdown energy. In both (a) and (b), the energy-based static stress drop $\Delta\tau_E$ is the difference between the average initial and final shear stresses. The total strain energy released $\Delta W/A$ is outlined by the black dashed line; the associated trapezoid ends at the x-axis (not shown). The dissipated energy E_D/A is given by the total area underneath the stress vs. slip curve (dotted + grey). Breakdown energy G is the subset of the dissipated energy labeled by the dotted area. Radiated energy can be calculated by subtracting total dissipated energy from the total strain energy released.

$$\Delta W/A = E_D/A + E_R/A. \tag{2.12}$$

The total strain energy released $\Delta W/A$ has shown to be described by the average shear stress on the fault during the event $\bar{\tau} = (1/2)(\bar{\tau}_i + \bar{\tau}_f)$ and the average final slip $\bar{\delta}_f$ as:

$$\Delta W/A = \frac{1}{2}(\bar{\tau}_i + \bar{\tau}_f)\bar{\delta}_f. \tag{2.13}$$

The total strain energy is divided into energy dissipated on the fault, dissipated energy E_D, and energy radiated off the fault as seismic waves, radiated energy E_R. Energy is dissipated on the fault due to friction, thus, the dissipated energy E_D/A is calculated by integrating the area under the shear stress vs. slip curve up to the final slip δ_f for the ruptured domain Σ (Section 3.1). For our 1D fault, let us define the edges of the ruptured domain Σ as L_1 and L_2. Then we get:

$$E_D/A = \frac{1}{L_2 - L_1} \int_{L1}^{L2} \left[\int_0^{\delta_f} \tau(\delta) d\delta \right]. \tag{2.14}$$

The remainder of the total strain energy released is the radiated energy:

$$E_R/A = \Delta W/A - E_D/A. \tag{2.15}$$

The dissipated energy E_D/A can further be partitioned into the breakdown energy G (Palmer and Rice, 1973; Rice, 1979) and frictionally dissipated energy E_F/A which makes up the remainder (labeled as "other dissipation" in Figure 2.3). The breakdown energy G_A is analogous to the fracture energy of fracture mechanics and can be calculated as (Method 1):

$$G_A = \frac{1}{L_2 - L_1} \int_{L1}^{L2} \left[\int_0^{\delta(\tau_{min}(x))} (\tau(\delta) - \tau_{min}(\delta)) d\delta \right] dx. \tag{2.16}$$

Then, the frictionally dissipated energy E_F/A can be found by subtracting G_A from E_D/A:

$$E_F/A = E_D/A - G_A. \tag{2.17}$$

Method (II) involves creating an average stress vs. slip representation for each event and calculating the energy balance, including the breakdown energy, from this single plot. This approach has the advantage of giving a single illustrative stress vs. slip plot for each event (Figure 2.3). We follow the averaging methodology of Noda and Lapusta, 2012 to perform this calculation. This involves taking the stress vs. slip evolution of every ruptured point and averaging them in slip rather than in time. Thus this can only be done once the event is complete and the stress vs. slip evolution is known everywhere. This averaging method preserves total strain energy released $\Delta W/A$ and total dissipated energy E_D/A. Every ruptured fault location has, in general, a different amount of total slip $\delta_f(x)$, so the stress vs. slip curves at each point are scaled in slip by $\bar{\delta}_f/\delta_f(x)$ so that each point has the same average slip $\bar{\delta}_f$. Then the stress values are scaled by the factor of $\delta_f(x)/\bar{\delta}_f$, thus preserving the areas representing E_D. Once all shear stress vs. slip curves are scaled, the stress values at each value of slip are averaged among the curves. We achieve this by interpolating the curves at 1000 evenly spaced points in slip. We can then calculate our energy

quantities from this average curve. The total strain energy released $\Delta W/A$ can be computed from the average curve as:

$$\begin{aligned} \Delta W/A &= \frac{1}{2}\bar{\delta_f}(\bar{\tau}_i + \bar{\tau}_f), \\ \bar{\tau}_{i(E)} &= \frac{\int_\Sigma \tau^i \delta_f(x) d\Sigma}{\int_\Sigma \delta_f(x) d\Sigma}, \\ \bar{\tau}_{f(E)} &= \frac{\int_\Sigma \tau^f \delta_f(x) d\Sigma}{\int_\Sigma \delta_f(x) d\Sigma}, \end{aligned} \tag{2.18}$$

where $\bar{\delta_f}$ is the average final slip for the event, $\bar{\tau}_i$ is the average initial shear stress, and $\bar{\tau}_f$ is the average final shear stress. Dissipated energy E_D can be found by integrating the area under the average curve:

$$E_D/A = \int_0^{\bar{\delta}_f} \bar{\tau}(\bar{\delta}) d\bar{\delta}. \tag{2.19}$$

One can also compute the breakdown energy from the average curve, here titled as G_{curve}:

$$G_{curve} = \int_0^{\bar{\delta}(\bar{\tau}_{min})} (\bar{\tau}(\bar{\delta}) - \bar{\tau}_{min}) d\bar{\delta}. \tag{2.20}$$

The average curve construction has been shown to preserve total strain energy released $\Delta W/A$ and dissipated energy E_D/A (Noda and Lapusta, 2012). However, it does not necessarily preserve the breakdown energy as the minimum shear stress of the average curve does not have a simple relation to the minimums of the curves of each ruptured point. We later show that the two methods give similar, but not identical, results. Note that G_A and G_{curve} have units of energy per unit area, while ΔW, E_D, and E_R denote the energies per event and have units of energy. Representations of the type shown in Figure 2.3 show energies per unit area, and that is why we have been considering quantities $\Delta W/A$, E_D/A, and E_R/A. To compute the corresponding energies per event, one needs to multiply them by the total ruptured area.

2.2.3 Stress Drop $\Delta\tau$ and Breakdown Energy G, from Observations

We seek to match the observed trends of magnitude-invariant stress drop and increasing breakdown energy G with increasing event size (Ide and Beroza, 2001;

Abercrombie and Rice, 2005; Viesca and Garagash, 2015). However, as discussed earlier, these values cannot be directly measured in observed events and instead must be inferred from other observations.

Stress drop is often calculated using the moment-based average (Equation 2.7). For large events, the rupture shape and dimension is found from finite-fault inversions (Somerville et al., 1999; Liu and Archuleta, 2000; Tinti et al., 2016). For small events, for which finite-fault inversions are not feasible, the spectral representation of the seismic waveforms is fitted by a model based on a circular crack with constant rupture speed to obtain Ω_0 (the long-period displacement amplitude) and f_c (corner frequency) measurements. These parameters are then used to calculate M_0 from Ω_0 (Brune, 1970) and the source radius r from f_c assuming a circular rupture and constant rupture velocity of $0.9c_s$ (Madariaga, 1976).

The breakdown energy can be estimated from observations as follows (Abercrombie and Rice, 2005):

$$G' = \frac{S}{2}\left(\Delta\sigma - \frac{2\mu E_R}{M_0}\right), \tag{2.21}$$

where G' is the approximation for the breakdown energy G, $\Delta\sigma$ is the (static) stress drop, μ is the shear modulus of the rock material, S is the average slip of the event, M_0 is the seismic moment, and E_R is the radiated energy. G' assumes both that the initial stress is the peak stress and that there is no stress overshoot or undershoot at the end of the event, making it potentially different from the actual G. (see Abercrombie and Rice, 2005, Figure 2). We refer to this G' as seismically-estimated breakdown energy G_{SE}.

Average slip can then be calculated as:

$$S = \frac{M_0}{\mu\pi r^2}, \tag{2.22}$$

and used along with Eshelby (1957) to infer stress drop:

$$\Delta\sigma = \frac{7\pi}{16}\frac{M_0}{r^3}. \tag{2.23}$$

The radiated energy E_R can be estimated by a number of methods (Ye et al., 2016a;Ye et al., 2016b).

2.3 Results for Fault Models with Standard Rate-and-State Friction

We begin with a standard rate-and-state formulation with no additional dynamic weakening. These models contain a 6 km VW region; parameters for our simulations are given in Tables 2.1 and 2.2. An example sequence of events for the standard rate-and-state case is shown in Figure 2.1b.

2.3.1 Theoretical Predictions

Based on previous studies and theoretical considerations (Cocco and Bizzarri, 2002, Lapusta and Liu, 2009), we expect both the fracture energy and the static stress drop to remain approximately the same for events of different sizes on a fault with given rate-and-state properties. This is because, at the rupture tip, the fault governed by the standard rate-and-state formulation behaves essentially as one governed by linear slip-weakening friction:

$$\begin{aligned} \tau_{LSW} &= \tau_p - W(\delta - \delta_{ini}) \text{ for } \delta - \delta_{ini} \leq D_c, \\ \tau_{LSW} &= \tau_d \text{ for } \delta - \delta_{ini} > D_c. \end{aligned} \tag{2.24}$$

For the standard rate-and-state formulation, one can write the initial stress τ_i from (2.1):

$$\tau_i = \bar{\sigma} \left[f_* + a \ln \frac{V_{ini}}{V_*} + b \ln \frac{V_* \theta_{ini}}{L} \right]. \tag{2.25}$$

As slip rate increases, due to the direct effect (assuming $V_{dyn} > V_{ini}$), stress will increase to some peak value τ_p at the dynamic slip rate V_{dyn}:

$$\tau_p = \tau_i + a\bar{\sigma} \ln \frac{V_{dyn}}{V_{ini}}. \tag{2.26}$$

Stress further evolves to a steady state dynamic level given by:

$$\tau_d = \tau_{ss}(V_{dyn}) = \bar{\sigma} \left[f_* + (a - b) \frac{V_{dyn}}{V_*} \right]. \tag{2.27}$$

This weakening effect occurs at weakening rate W:

$$W = \frac{b\bar{\sigma}}{L}, \tag{2.28}$$

and the evolution occurs over some critical slip-weakening distance D_C:

$$D_c = L \ln \frac{\theta_{ini} V_{dyn}}{L}. \tag{2.29}$$

Thus we expect:

$$\Delta\tau = \tau_i - \tau_d = \bar{\sigma} \left[a \ln \frac{V_{ini}}{V_*} + b \ln \frac{V_* \theta_{ini}}{L} - (a-b) \ln \frac{V_{dyn}}{V_*} \right] \tag{2.30}$$

$$G = \frac{1}{2} \left(\tau_p - \tau_d \right) D_c = \frac{1}{2} b \bar{\sigma} L \left(\ln \frac{\theta_{ini} V_{dyn}}{L} \right)^2. \tag{2.31}$$

These quantities depend on the dynamics of the process through V_{dyn} and θ_{ini}, but this is a weak dependence since both are contained within logarithms and changes of even an order of magnitude alter the final product by only a small amount. There is a much stronger dependence on the friction parameters a, b, and L, which are presumed to be constant in a given model.

2.3.2 Magnitude-Invariant G and variations in $\overline{\Delta\tau}$ for given a, b, and L

Indeed, our simulations show that for uniform frictional parameters a, b, and L along the fault, both G_A and $\Delta\tau$ are nearly constant for events of different sizes. Both trends are evident in the accumulated slip profiles and average curves for three events of different sizes, but the same $L = 250$ μm (Figure 2.4). Larger events accumulate more slip and rupture longer fault stretches, but the breakdown energy (dotted area) and static stress drop are nearly equal for the three illustrated events. This is not surprising considering that the effective weakening distance in the standard rate-and-state model depends mostly on L (e.g., Cocco and Bizzarri, 2002).

There are some slights trends due to the dynamics of the process. Larger events tend to have lower average initial stresses, due to rupturing longer fault stretches, building more stress concentration, and entering slightly less favorably stressed regions. All events weaken down to approximately the same dynamic level, as expected. This leads to a slight decrease in the static stress drop from $\overline{\Delta\tau}_E = 3.3$ MPa for the smallest event down to $\overline{\Delta\tau}_E = 1.8$ MPa for the largest event. The peak stress τ_p slightly increases with the event size, due to more stress concentration during the larger event and higher initial values for the state variable θ_{ini} from longer recurrence times. The outcome is slightly higher breakdown energies as the event size increases. However, these two effects produce relatively small variations in both G and $\Delta\tau$.

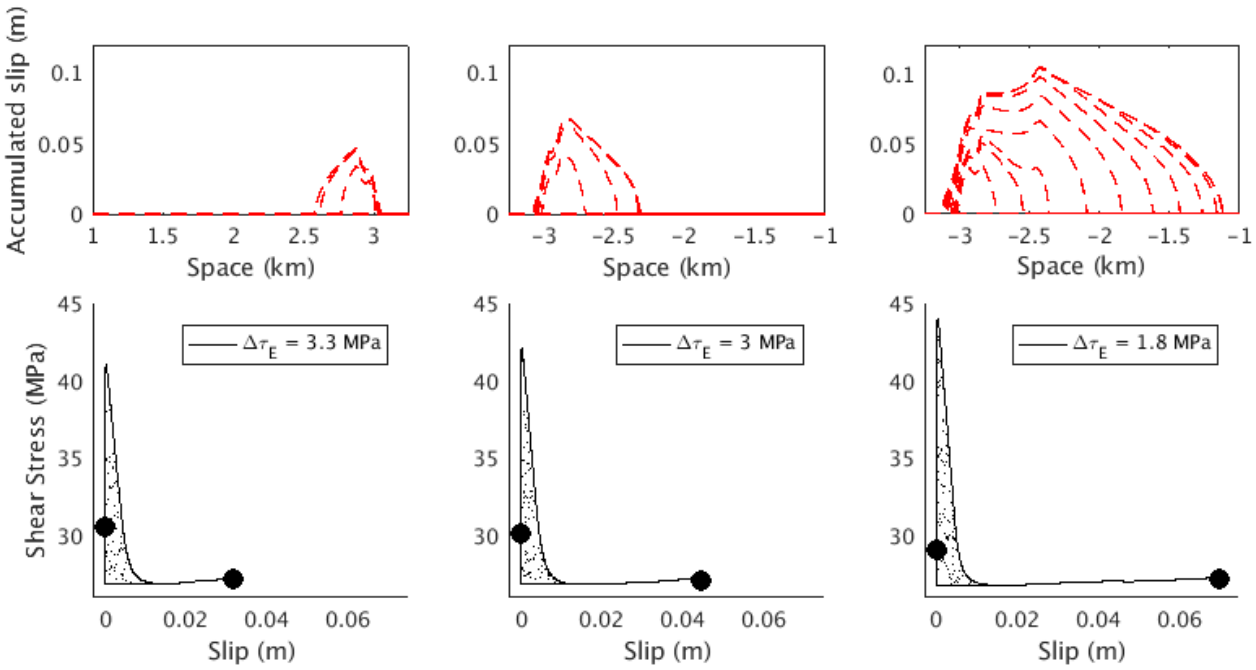

Figure 2.4: Three sample events from the standard rate-and-state simulation with $L = 250\ \mu$m and different average final slip. (top) Accumulated slip profiles illustrate the total slip along the fault as well as the spatial extent of the rupture. (bottom) Average shear stress vs. slip curves illustrate the average behavior on the fault during the event. The initial and final stresses are marked by circles; the breakdown energy is indicated by the dotted area. For a given value of L, the breakdown energy remains nearly constant. The stress drop slightly decreases and the breakdown energy slightly increases with the event slip, as discussed in the text. These three events are marked with grey, downward-pointing triangles in Figure 2.5.

We find that these trends extend for all events in our simulations (Figures 2.5 and 2.6a). For $L = 250\ \mu$m (black circles), events differ by nearly an order of magnitude in slip, from 0.01 m to 0.1 m. The corresponding stress drops are nearly constant around 2-3 MPa with a slight decreasing trend with the increasing event size. The breakdown energies are also approximately constant, with a slight increasing but saturating trend (Figure 2.6a) for all events.

Our example event discussed earlier shows the expected behavior (Figure 2.2) for the standard rate-and-state case. This event has the area-averaged stress drop of $\overline{\Delta\tau}_A = 2.4$ MPa, which matches well with the stress drop distribution seen in Figure 2.2. The entire ruptured domain is plotted in Figure 2.2, including penetration into the velocity-strengthening region. This is evident from the negative stress drops found at the edges of the event, greater than 3 km away from the center of the

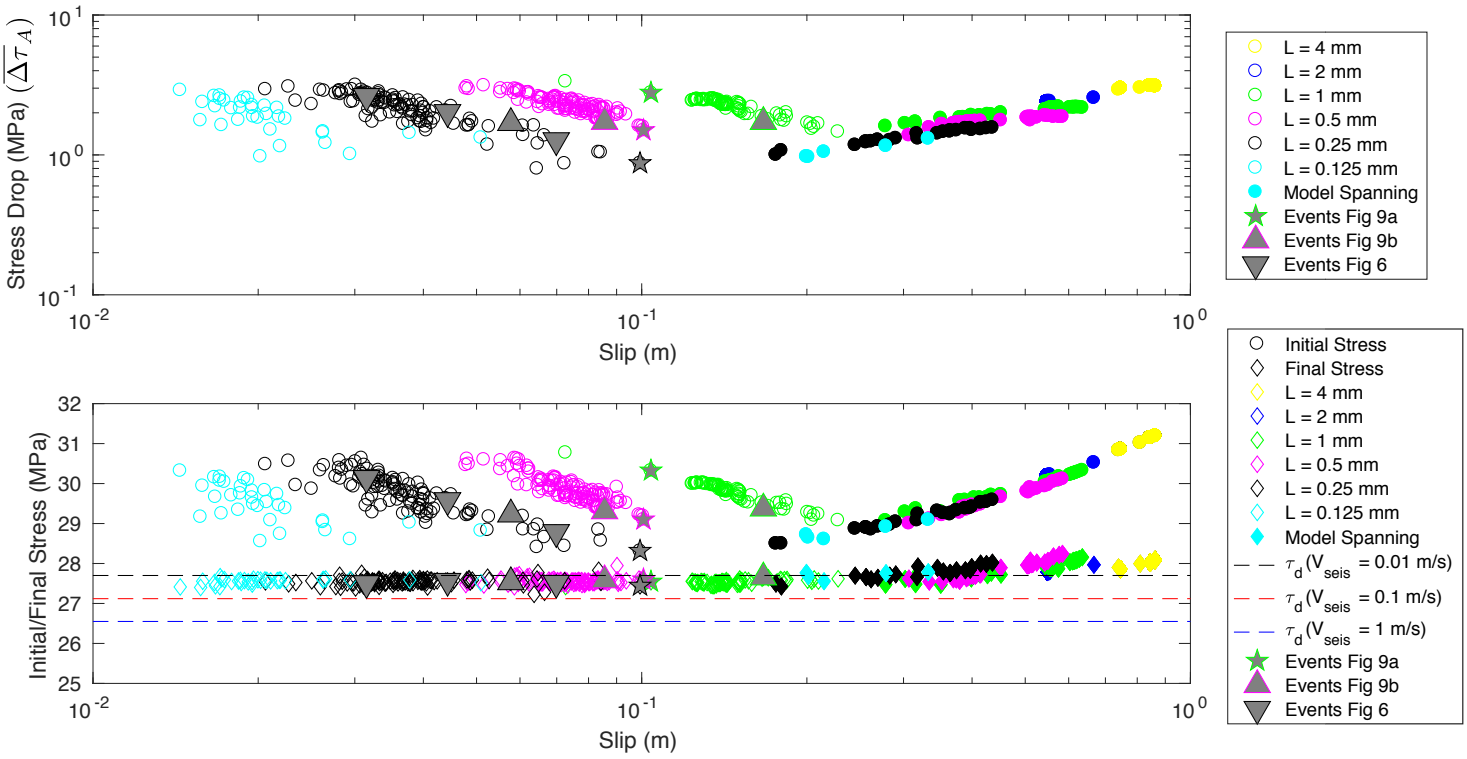

Figure 2.5: (top) Stress drops $\overline{\Delta\tau}_A$ for events from several simulations with standard rate-and-state friction and L ranging from 0.125 mm to 4 mm (no dynamic weakening). Complete rupture events are marked with filled-in shapes. The stress drops do not vary with L. (bottom) Average initial and final stresses for each event from the same simulations. Average final stresses are similar for all events and agree with the expected dynamic levels of stress for V_{dyn} = 0.01 - 0.1 m/s.

fault. Three representative points are chosen to show the variability of the stress vs. slip evolution along the fault. The point at 2.4 km is in the nucleation zone and experiences mostly aseismic stress evolution (solid line preceding initial stress point) followed by little coseismic stress change with slip. The point in the arrest zone (-3.6 km) shows a very different behavior, with an increase to a peak level and a drop. However, the stress drop is negative (stress increase), owing to the velocity-strengthening properties of the fault at this point. The point at the center of the fault (0 km) is representative of the behavior of the majority of the fault. This point shows the typical rate-and-state behavior with an increase to a peak level of stress followed by a drop to a near-constant dynamic level of stress. This point experiences a stress drop similar to the average for the entire event. All of the points on the fault are averaged to create the illustrative average curve (Figure 2.3a). From the average curve, it is apparent that the majority of points follow the behavior qualitatively

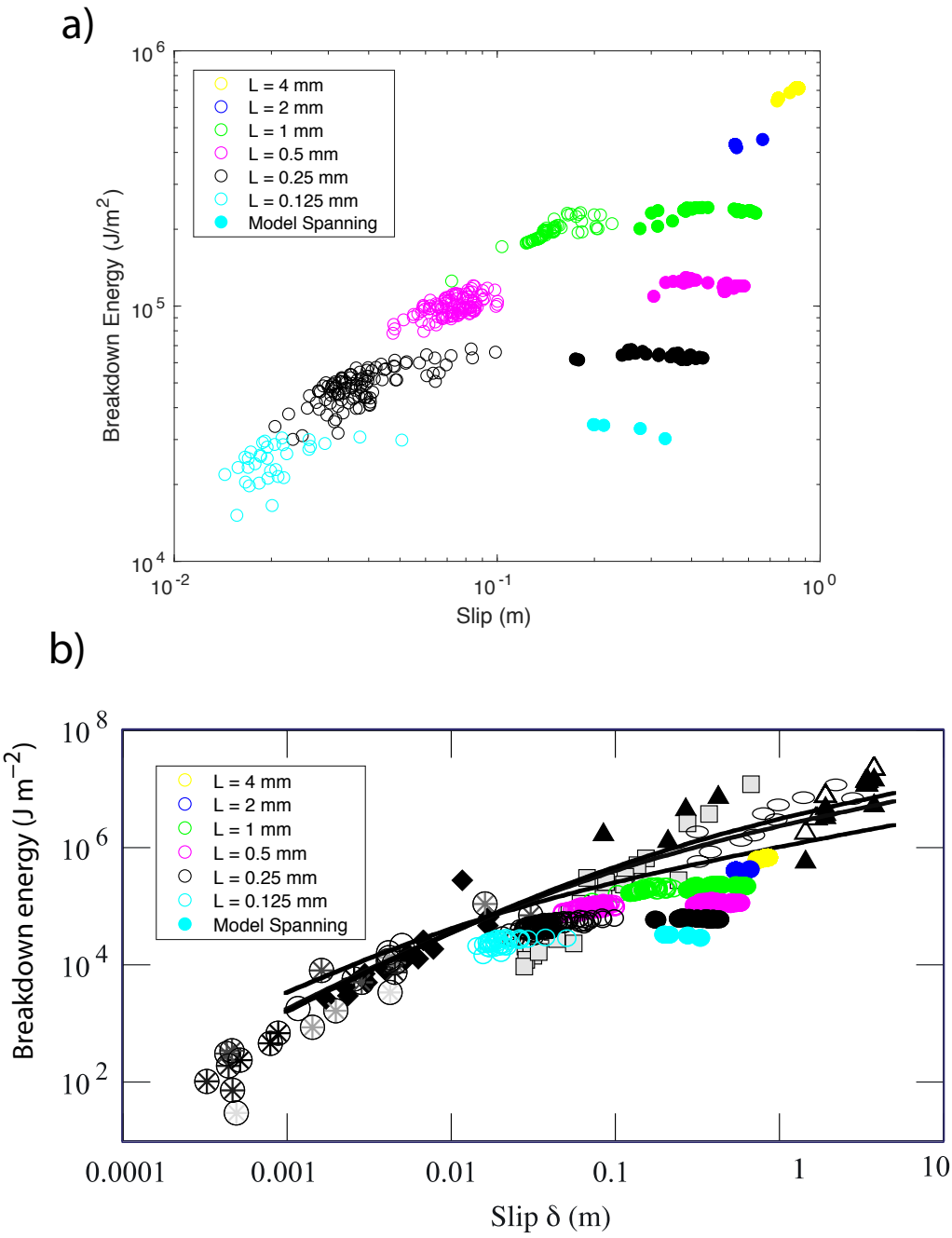

Figure 2.6: a) Breakdown energies G_A for events from several simulations with standard rate-and-state friction and L ranging from 0.125 mm to 4 mm (no dynamic weakening). Complete rupture events are marked with filled-in shapes. Increasing L leads to an increase in the breakdown energy, but the breakdown energy only slightly increases and saturates for events with the same L. The two largest values of L lead to almost exclusively complete rupture events because the nucleation size is too large to produce small events. b) Breakdown energies from simulated events overlaid on results from Rice, 2006. The values are similar, although a standard rate-and-state model produces breakdown energies that do not increase at the same rate as those from observed events. Increasing L leads to an increase in breakdown energy G, but does not match the same increase in the trend of the observed events.

similar to the point at 0 km. Note that the energy-based stress drop from the average curve is $\overline{\Delta\tau}_E = 4$ MPa, which is higher than the $\overline{\Delta\tau}_A = 2.4$ MPa as expected (Noda and Lapusta, 2012).

2.3.3 Increasing G and magnitude-invariable $\overline{\Delta\tau}$ with Increasing Values of L

Breakdown energy has a weak dependence on the dynamics in a standard rate-and-state fault model, but it strongly depends on the characteristic slip distance L. One of the ways to reproduce an increase in G_A with average slip is to systematically increase L, which also systematically alters the effective critical slip-weakening distance D_c (Figure 2.7). The peak stress of each event also increases, predominantly due to a longer recurrence time that results in fault strengthening. Increasing L increases the nucleation size of the event and thus a stress increase must penetrate further into the fault before an event nucleates, leading to a higher initial state variable θ_{ini}, higher initial stress τ_i, and higher peak stress τ_p. This is even the case for events with the same amount of average slip (Figure 2.7a). However, the increase in the critical slip-weakening distance is clearly the main contributing factor to the increased G_A. The dynamic levels of stress are nearly constant in all three cases as expected; this level does not directly depend on L. The stress drops increase with increasing L for these three events, due to the fact that we have chosen three events with very similar slips (Figure 2.5a - star symbols). Stress drops for the entire sequence of events do not change as we increase L (Figure 2.5a). This is illustrated by selecting three other events that no longer have the same average final slip (Figure 2.7b), but do have comparable stress drops.

Varying L over an order of magnitude from 125 μm to 4 mm leads to a clear increase in breakdown energy (Figure 2.6a) that is much larger than the slight increasing trend we find for larger events of a given L. There are clear groups of events with similar breakdown energies, corresponding to simulations with each value of L. Increasing L increases G_A. The values for the breakdown energies compare favorably to those from Rice, 2006, although they are lower for higher values of slip (Figure 2.6b). For a given L, the simulated breakdown energies level-off and do not capture the observed trend. Even increasing L is not completely sufficient to match the observed trend.

Simulations with all values of L have comparable stress drops, determined by values of σa and σb. All of our calculated stress drops fall into the 1-3 MPa range which is consistent with inferred stress drops from natural events. We find two distinct

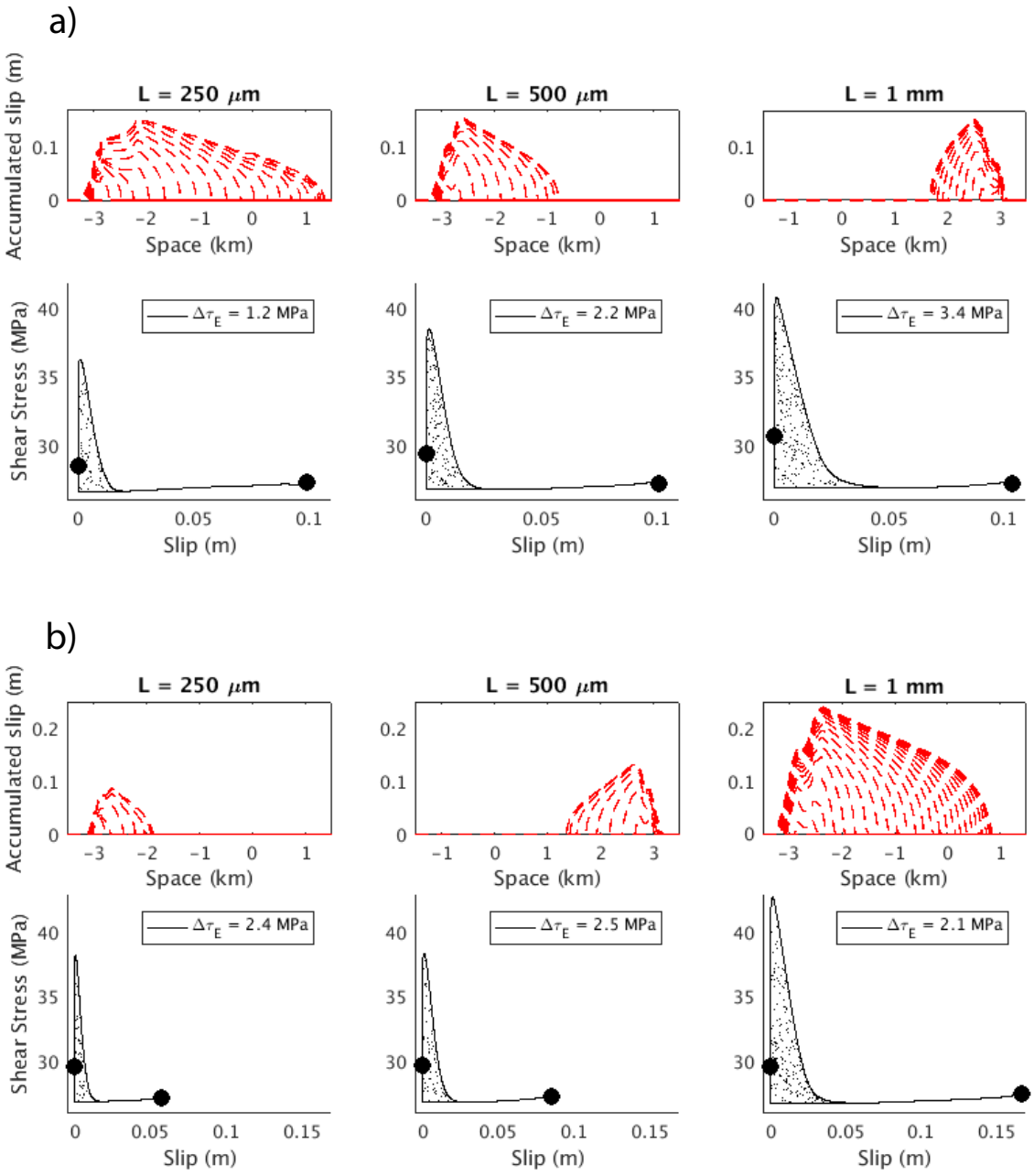

Figure 2.7: a) Three sample events with comparable average final slip from rate-and-state simulations with different L. (Row 1) Accumulated slip profiles illustrate the total slip along the fault as well as the spatial extent of the rupture. (Row 2) Average stress vs. slip curves illustrate the average shear stress vs. slip behavior on the fault during the event. Increasing L increases both the slip weakening distance D_c as well as the breakdown energy of an event with comparable average final slip. These three events are marked with grey stars in Figure 2.5. b) Three sample events with comparable stress drops, but varying final slips, from rate-and-state simulations with different L. (Row 1) Accumulated slip profiles and (Row 2) average stress vs. slip curves. Increasing L increases both the slip weakening distance D_c as well as the breakdown energy, but does not affect the average stress drop. These three events are marked with grey upward-pointing triangles in Figure 2.5.

trends when separating partial rupture from complete rupture events (Figure 2.5). The first trend is that the partial rupture events show a slight decrease in stress drop with increasing slip. This is because all events arrest at similar levels of average final stress. However, as discussed in the previous section, larger events initiate with lower average levels of prestress (unless they are complete ruptures, as discussed below), and thus have smaller stress drops. The second is for the complete rupture events; these events have the same ruptured domain and the ones with larger slip correspond to larger stress drop, reflecting variability in the prestress level for complete rupture events.

2.4 Conclusions

The standard rate-and-state models reproduce realistic stress drops. However, the breakdown energies are dependent on the rate-and-state characteristic slip L and increase only slightly with the increasing event size for events of different sizes for a given value of L, and then saturate for the largest events. This can be resolved by using a non-constant value for L, perhaps one that evolves with slip or slip rate. One can physically motivate this by imagining that the characteristic slip distance evolves as the fault slips and undergoes physical changes including damage on the fault in the form of gouge and off the fault in the form of cracking. These processes may alter the "effective" characteristic slip distance on the fault during the dynamic event. Evolving L during the event may serve as a proxy for these additional phenomena. However, while increasing L leads to increasing breakdown energies, this alone is not sufficient to match the observed trend, and because nucleation size increases with larger L, the models with large L are no longer able to produce the smallest events.

References

Abercrombie, Rachel E. and James R. Rice (2005). “Can observations of earthquake scaling constrain slip weakening?” In: *Geophysical Journal International* 162, pp. 406–424. DOI: 10.1111/j.1365-246X.2005.02579.x.

Brune, James N. (1970). “Tectonic Stress and the Spectra of Seismic Shear Waves from Earthquakes”. In: *Journal of Geophysical Research* 75.26, pp. 4997–5009.

Cocco, Massimo and Andrea Bizzarri (2002). “On the slip-weakening behavior of rate- and state dependent constitutive laws”. In: *Geophysical Research Letters* 29.11. DOI: 10.1029/2001GL013999.

Dieterich, James H. (1979). "Modeling of Rock Friction 1. Experimental Results and Constitutive Equations". In: *Journal of Geophysical Research* 84.B5, pp. 2161–2168.

Ide, Satoshi and Gregory C. Beroza (2001). "Does apparent stress vary with earthquake size?" In: *Geophysical Research Letters* 28.17, pp. 3349–3352.

Kanamori, Hiroo and Don L Anderson (1975). "Theoretical basis of some empirical relations in seismology". In: *Bulletin of the seismological society of America* 65.5, pp. 1073–1095.

Lapusta, Nadia and Yi Liu (2009). "Three-dimensional boundary integral modeling of spontaneous earthquake sequences and aseismic slip". In: *Journal of Geophysical Research* 114, B09303. DOI: 10.1029/2008JB005934.

Lapusta, Nadia, James R. Rice, Yehuda Ben-Zion, and Gutuan Zheng (2000). "Elastodynamic Analysis for Slow Tectonic Loading with Spontaneous Rupture Episodes on Faults with Rate- and State- dependent Friction". In: *Journal of Geophysical Research* 105, pp. 765–789. DOI: 10.1029/2000JB900250.

Liu, P and RJ Archuleta (2000). "Inversions for kinematic source parameters of the 1994 Northridge earthquake using a three dimensional velocity structure". In: *Seism. Res. Lett* 71, p. 220.

Madariaga, Raul (1976). "Dynamics of an Expanding Circular Fault". In: *Bulletin of the Seismological Society of America* 66.3, pp. 639–666.

– (1979). "On the Relation Between Seismic Moment and Stress Drop in the Presence of Stress and Strength Heterogeneity". In: *Journal of Geophysical Research* 84.B5, pp. 2243–2250.

Noda, Hiroyuki and Nadia Lapusta (2010). "Three-dimensional earthquake sequence simulations with evolving temperature and pore pressure due to shear heating: Effect of heterogeneous hydraulic diffusivity". In: *Journal of Geophysical Research* 115, B123414. DOI: 10.1029/2010JB007780.

– (2012). "On Averaging Interface Response During Dynamic Rupture and Energy Partitioning Diagrams for Earthquakes". In: *Journal of Applied Mechanics* 79. DOI: 10.1115/1.4005964.

Noda, Hiroyuki, Nadia Lapusta, and Hiroo Kanamori (2013). "Comparison of average stress drop measures for ruptures with heterogeneous stress change and implications for earthquake physics". In: *Geophysical Journal International*. DOI: 10.1093/gji/ggt074.

Palmer, Andrew Clennel and JR Rice (1973). "The growth of slip surfaces in the progressive failure of over-consolidated clay". In: *Proceedings of the Royal Society of London A: Mathematical, Physical and Engineering Sciences* 332.1591, pp. 527–548.

Rice, J. R. (1979). "The Mechanics of Earthquake Rupture". In: *in Physics of Earth's Interior*, pp. 555–649.

Rice, James R. (2006). “Heating and weakening of faults during earthquake slip”. In: *Journal of Geophysical Research* 111, B05311. DOI: 10.1029/2005JB004006.

Rice, James R, Nadia Lapusta, and K Ranjith (2001). “Rate and state dependent friction and the stability of sliding between elastically deformable solids”. In: *Journal of the Mechanics and Physics of Solids* 49.9, pp. 1865–1898.

Rice, JR and A L Ruina (1983). “Stability of steady frictional slipping”. In: *Journal of Applied Mechanics* 50.2, pp. 343–349.

Rubin, AM and J-P Ampuero (2005). “Earthquake nucleation on (aging) rate and state faults”. In: *Journal of Geophysical Research: Solid Earth* 110.B11.

Ruina, Andy (1983). “Slip Instability and State Variable Friction Laws”. In: *Journal of Geophysical Research* 88.B12, pp. 10359–10370.

Somerville, Paul et al. (1999). “Characterizing crustal earthquake slip models for the prediction of strong ground motion”. In: *Seismological Research Letters* 70.1, pp. 59–80.

Tinti, E, L Scognamiglio, A Michelini, and M Cocco (2016). “Slip heterogeneity and directivity of the ML 6.0, 2016, Amatrice earthquake estimated with rapid finite-fault inversion”. In: *Geophysical Research Letters* 43.20.

Viesca, Robert C. and Dmitry I. Garagash (2015). “Ubiquitous weakening of faults due to thermal pressurization”. In: *Nature Geoscience* 8, pp. 875–879. DOI: 10.1038/NGEO2554.

Ye, Lingling, Thorne Lay, Hiroo Kanamori, and Luis Rivera (2016a). “Rupture characteristics of major and great (Mw 7.0) megathrust earthquakes from 1990 to 2015: 1. Source parameter scaling relationships”. In: *Journal of Geophysical Research: Solid Earth* 121.2, pp. 826–844.

– (2016b). “Rupture characteristics of major and great (Mw 7.0) megathrust earthquakes from 1990 to 2015: 2. Depth dependence”. In: *Journal of Geophysical Research: Solid Earth* 121.2, pp. 845–863.

Chapter 3

MAGNITUDE-INVARIANT STRESS DROPS AND INCREASES IN BREAKDOWN ENERGY IN EARTHQUAKE SEQUENCE SIMULATIONS WITH THERMAL PRESSURIZATION

Here we extend our investigation from Chapter 2 into magnitude-invariant stress drops and increasing breakdown energies with the event size, by adding enhanced dynamic weakening to our rate-and-state models.

3.1 Additional Dynamic Weakening - Thermal Pressurization

Laboratory experiments have shown that the rate-and-state laws (Equations 2.1-2.4) work well for relatively slow slip rates (10^{-9} to 10^{-3} m/s). However, at seismic rates of ~1 m/s, additional dynamic weakening mechanisms, such as thermal pressurization, can be present. Thermal pressurization occurs when fluids within the fault heat up, expand, and pressurize during dynamic rupture, reducing the effective normal stress (Sibson, 1973; Rice, 2006; Noda and Lapusta, 2010). The thermal pressurization effect is governed in our model by the following coupled differential equations for pressure and temperature evolution(Noda and Lapusta, 2010):

$$\frac{\partial p}{\partial t} = \alpha_{hy}\frac{\partial^2 p}{\partial y^2} + \Lambda\frac{\partial T}{\partial t}, \tag{3.1}$$

$$\frac{\partial T}{\partial t} = \alpha_{th}\frac{\partial^2 T}{\partial y^2} + \frac{\tau V}{\rho c}\frac{exp(-y^2/2w^2)}{\sqrt{2\pi}w}, \tag{3.2}$$

where T is the temperature of the pore fluid, α_{hy} is the hydraulic diffusivity, α_{th} is the thermal diffusivity, τV is the source of shear heating distributed over the shear zone of half-width w, ρc is the specific heat, y is the distance normal to the fault plane, and Λ is the coupling coefficient that gives pore pressure change per unit temperature change under undrained conditions.

The efficiency of the thermal pressurization process depends on the interplay of several of these parameters. Shear heating, τV, must be strong enough to raise the temperature, given both the specific heat of the rock, ρc, and the half-width of the shear zone, w. Furthermore, this heat generation must not be dissipated too quickly by the thermal diffusivity, α_{th}, of the system. If sufficient heat is

generated, the temperature of the system increases, and this increase is coupled into an increase in pressure of the fluid. The fluid then pressurizes as long as the hydraulic diffusivity, α_{hy}, is not too large. Several of these parameters are relatively well constrained from laboratory experiments: $\alpha_{th} = 10^{-6}$ m/s, $\Lambda = 0.1$ MPa/K, and $\rho c = 2.7$ MPa/K (Wibberley and Shimamoto, 2005; Rempel and Rice, 2006; Noda and Lapusta, 2010). Thus, the efficiency of the process is effectively controlled by the half-width w and hydraulic diffusivity α_{hy}, which can vary significantly: w can vary from 10^{-3} m to 10^{-1} m and α_{hy} can vary from 10^{-2} m^2/s to 10^{-5} m^2/s (e.g., Rice, 2006). Changing these two parameters within these ranges can make thermal pressurization either very efficient or completely negligible. The values we have chosen are motivated by prior studies (Rice, 2006; Noda and Lapusta, 2010) and are given in Tables 2.1 and 3.1.

Table 3.1: Parameters for Models with Thermal Pressurization

Parameter	Symbol	12 km VW Zone	24 km VW Zone
Fault length along strike	λ	72 km	96 km
VW region length (total)	W_{VW}	12 km	24 km
VS region length (total)	W_{VS}	60 km	48 km
Effective normal stress	$\bar{\sigma} = (\sigma - p)$	50 MPa	50 MPa
Thermal diffusivity	α_{th}	10^{-6} m^2/s	10^{-6} m^2/s
Hydraulic diffusivity	α_{hy}	10^{-3} m^2/s	10^{-3} m^2/s
Specific heat	ρc	2.7 MPa/K	2.7 MPa/K
Half width	w	10 mm	10 mm
Coupling coefficient (when TP present)	Λ	0.1 MPa/K	0.1 MPa/K
Rate-and-state direct effect (VS)	a	0.050	0.025
Rate-and-state evolution effect (VS)	b	0.003	0.005
Rate-and-state direct effect (VW)	a	0.01	0.01
Rate-and-state evolution effect (VW)	b	0.015	0.015
Characteristic slip	L	2 mm	2 mm
Cell size	Δx	5 m	9 m
Cohesive Zone	Λ_0	75 m	75, 38 m
Nucleation Size (Rice & Ruina, 1985)	h^*_{RR}	200 m	200, 100 m
Nucleation Size (Rubin & Ampuero, 2005)	h^*_{RA}	490 m	490, 245 m

3.2 Representative Simulated Events

As in Section 2.1.3, we present a sample dynamic event from our simulations (Figure 3.1). Just as before, the spatially varying initial and final shear stress distributions along the fault lead to a stress drop distribution that varies along the fault. The shear stress vs. slip evolution along the fault is illustrated for three representative locations. Locations near the nucleation region still experience a small coseismic stress drop.

Points near the middle of the ruptured area show the expected increase in stress to a peak value, followed by a drop, controlled by our rate-and-state laws, down to a variable dynamic value. The additional weakening due to thermal pressurization is evident in Figure 3.1, as shear stress continues to decrease with slip beyond the dynamic level reached in Figure 2.2.

3.3 Results for Models with Thermal Pressurization

We begin by considering a 12 km long VW segment surrounded by two 24 km long VS sections. We then increase our seismogenic zone from 12 km to 24 km in order to further expand the range of the simulated event sizes.

3.3.1 12 km Fault

Our simulations produce a range of events, with average slips of 0.1 m up to 5 m. One of the events (Event 2) is illustrated in more detail in Figure 3.1. It nucleates in an area of higher prestress and propagates along the fault until it reaches lower levels of prestress that are unfavorable enough to arrest the event. The shear stress vs. slip behavior is shown for three representative points similar to those for the standard rate-and-state event of Figure 2.2. All three points show continuous weakening with slip, illustrating that thermal pressurization is acting effectively along the entire fault. The point in the nucleation zone (-5.25 km) again shows significant aseismic stress evolution (solid line preceding the initial stress point), followed by lesser coseismic stress change with slip. The other two points along the fault (-3.75 km and -2.4 km) show the expected behavior for most ruptured points with an initial increase and rapid decrease in stress (similar to the standard rate-and-state behavior) followed by a continuous decrease in stress with slip (due to dynamic weakening from thermal pressurization). The average curve for this event (Figure 2.3b) shows the behavior similar to the points outside the nucleation zone.

To illustrate how stress drop and breakdown energy vary with the event size, we consider three representative events with progressively larger average slip (Figure 3.2). The smallest event (Event 64) has the highest average prestress and also the highest average final stress. The intermediate-size event (Event 33) has a lower prestress and it weakens more so it also has a lower final stress. The largest event (Event 20) has the lowest average initial stress and it weakens the most, so it also has the lowest average final stress. As a result, all three events have approximately the same stress drop $\overline{\Delta\tau}_E$ of 7 MPa. As the average slip of the events increases, so does the breakdown energy (Figure 3.2). This increase in the breakdown energy is

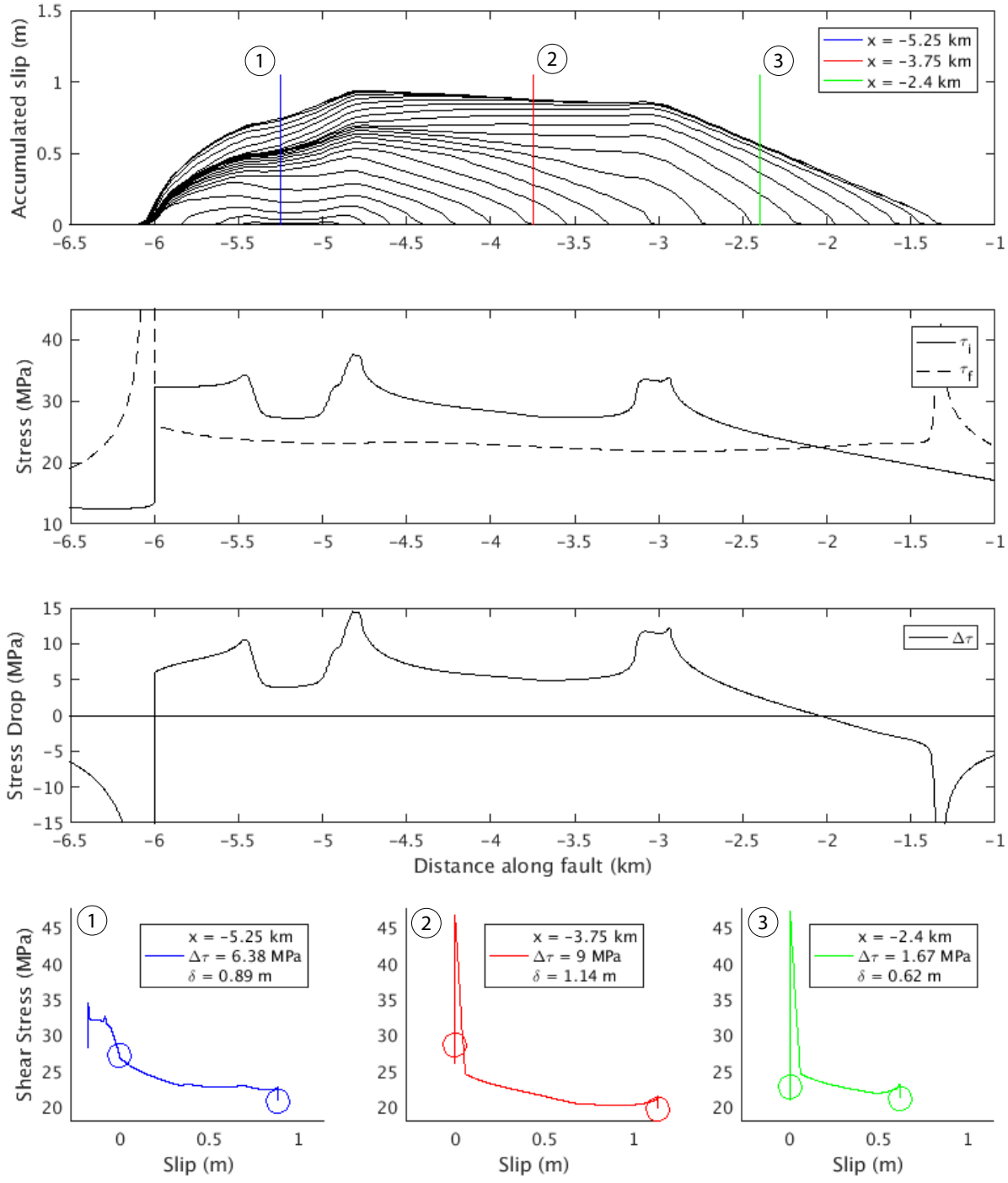

Figure 3.1: A representative event for the model with thermal pressurization. The plotting conventions are the same as on Figure 2.2. The three sample points exhibit decreasing stress with slip throughout the event, illustrating the effect of additional dynamic weakening due to thermal pressurization.

due to the additional dynamic weakening, as expected, based on considerations in Rice, 2006. A portion of the sequence of events produced by this model is shown in Figure 3.3, and events 20 and 33 are plotted in blue to show their relative size to the rest of the sequence.

However, we do observe slightly different behavior for complete rupture events; this will be discussed further in the next section. These events only occur when the prestress on the fault is favorable, meaning they never encounter areas of unfavorable prestress that would both decrease the average initial stress of the rupture points as well as arrest the events. These largest events rupture the whole domain and are forcefully stopped by the velocity-strengthening regions rather than arresting due to insufficient prestress. The properties of the VS regions then affect the stress drops of these complete rupture events, as discussed in section 3.4. A comparison between an intermediate-sized event and a complete rupture event for the 12 km fault shows both the difference in initial stress distribution and stress drop distribution along the fault (Figure 3.4). The partial rupture event (event 72) has an initial stress distribution that dips around the middle of the fault. This prestress condition is unfavorable enough that, even with the dynamic weakening, the event is not able to propagate through this region and it arrests at around 1 km to the right of the center of the fault. In contrast, the complete rupture event (event 15) has a prestress distribution that is higher and favorable for the entire length of the fault.

Stress drop and breakdown energy trends are analyzed in more detail for all events in the 24 km Model 1 sequence in the following section.

3.3.2 24 km Fault

Extending our fault to 24 km allows for a greater range of event sizes, with slips ranging from 0.07 m to 10 m. Model 1 (24 km VW region) utilizes 50 MPa normal stress and hydraulic diffusivity $\alpha_{hy} = 10^{-3}$ m^2/s along with all parameters shown in Tables 2.1 and 3.1.

Let us consider the stress drops for all events. Both energy-based stress drops $\overline{\Delta\tau}_E$ and area-averaged stress drops $\overline{\Delta\tau}_A$ are calculated (Figure 3.5a). For the partial rupture events, the stress drops are approximately constant, for the final average slips ranging from 0.1 m to 1 m, an order of magnitude. The energy-based stress drops are consistently higher than the area-averaged ones, consistent with Noda et al., 2013. The complete rupture events break the magnitude-invariant trend, exhibiting increasing stress drop with the the increasing event size for the area-averaged case.

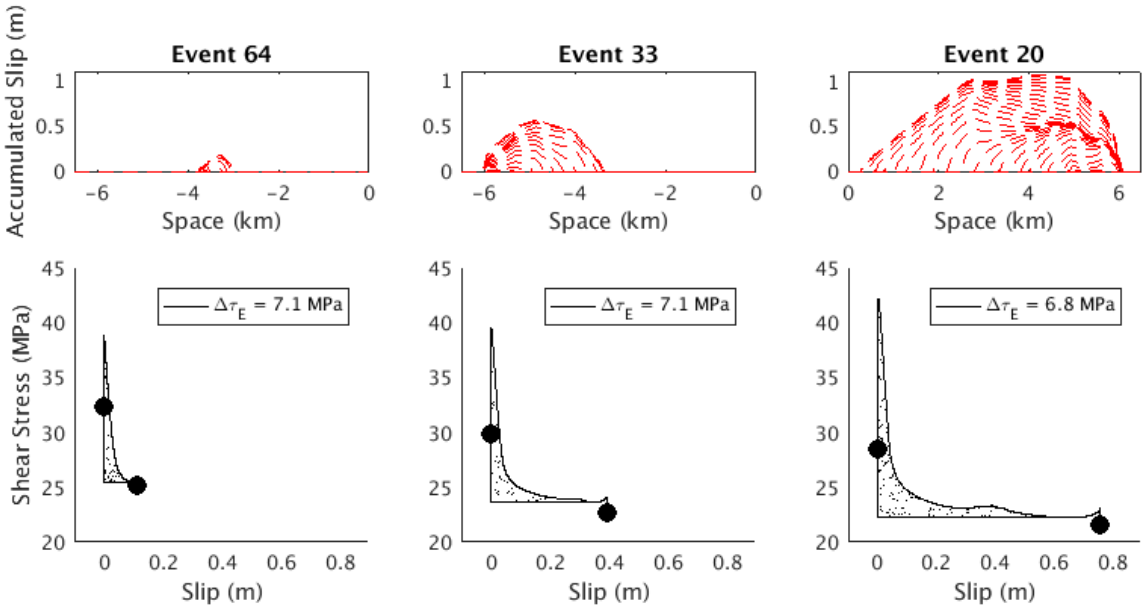

Figure 3.2: Three sample partial rupture events from the simulations with thermal pressurization and a 12 km long velocity-weakening region. (top) Accumulated slip profiles of the three events. (bottom) Average shear stress vs slip curves. The initial and final stresses are marked by circles; the breakdown energy is indicated by the dotted area. As event size increases, both the average initial stress and average final stress decrease, so that the stress drops calculated from the average curves remains nearly constant at ~7 MPa.

These findings confirm our hypothesis that larger events weaken more but also tend to occur at lower average initial stress, thus keeping stress drops relatively constant over a range of event sizes. In fact, for the entire sequence of partial rupture events, both average initial and average final stresses decrease with the increasing event size (or slip) (Figure 3.5b). Complete rupture events have different behavior from partial rupture events. However, the stress drops of these complete rupture events are only slightly larger than their partial rupture counterparts. This is likely due to compensation from the increased penetration into the VS region by the complete rupture events. Including more points with the VS behavior into the ruptured region, which experience a stress increase during the events, decreases the average stress drop of the events. This is further explored in section 3.4.

Breakdown energy G_A increases with increasing event size (Figure 3.6a) and matches the behavior of G_A in the 12 km model. Using our numerical models, we can compare the actual values of G_A computed from simulations with estimates using

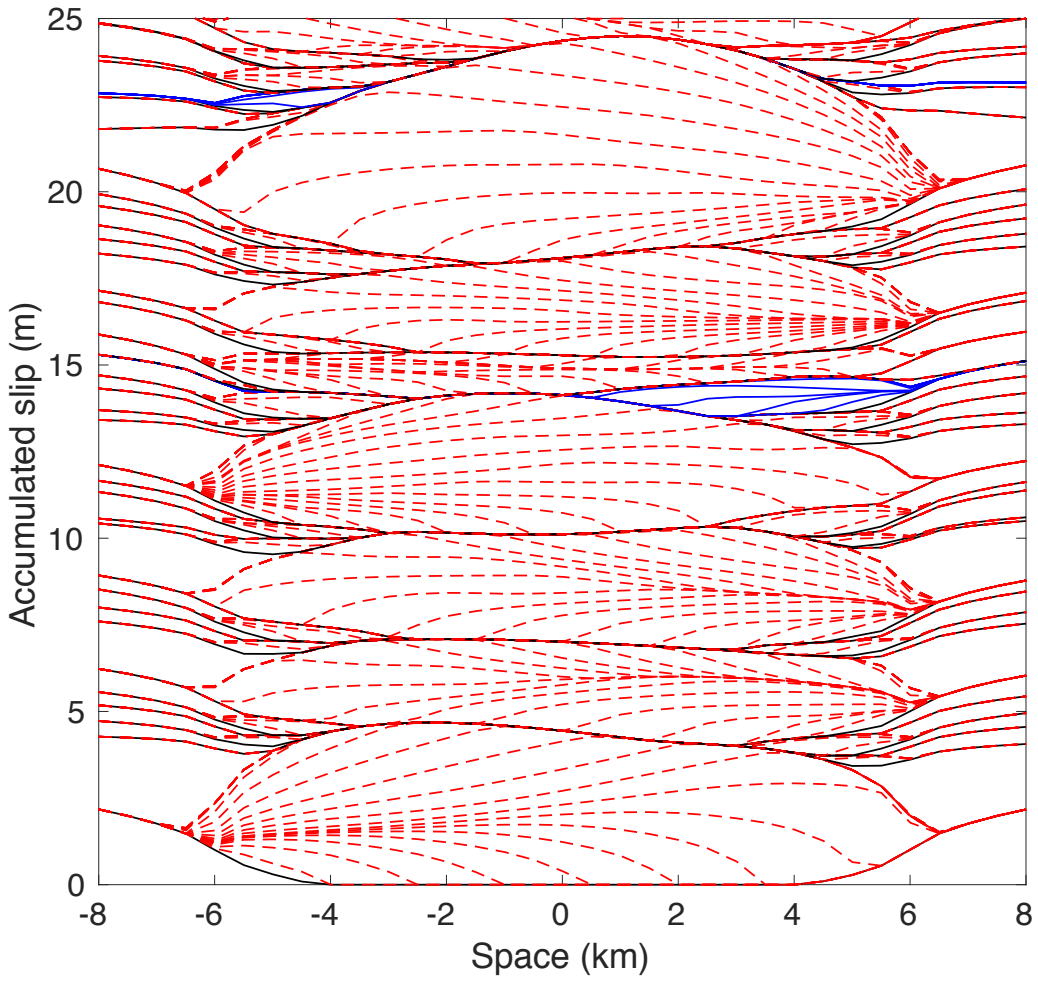

Figure 3.3: Accumulated slip profiles for a portion of the sequence of events produced by the model with thermal pressurization and a 12 km VW region. Two of the events in blue (20 and 33) are shown in Figure 3.2.

seismological methods (e.g., Abercrombie and Rice, 2005). In other words, we compute estimates G_{SE} for our events using Equation (2.21). The comparison (Figure 3.6b) shows that the actual and estimated values agree relatively well in the majority of cases. This is likely because the resulting ruptures are close to being crack-like, without significant undershoot characteristic for pulse-like ruptures (Heaton, 1990; Kanamori and Rivera, 2006; Garagash, 2012). We examine this issue in more detail in Chapter 4.

Next, we compare breakdown energies G_A to breakdown energies estimated for natural events (Rice, 2006). Our results agree well, (Figure 3.6c), as expected from

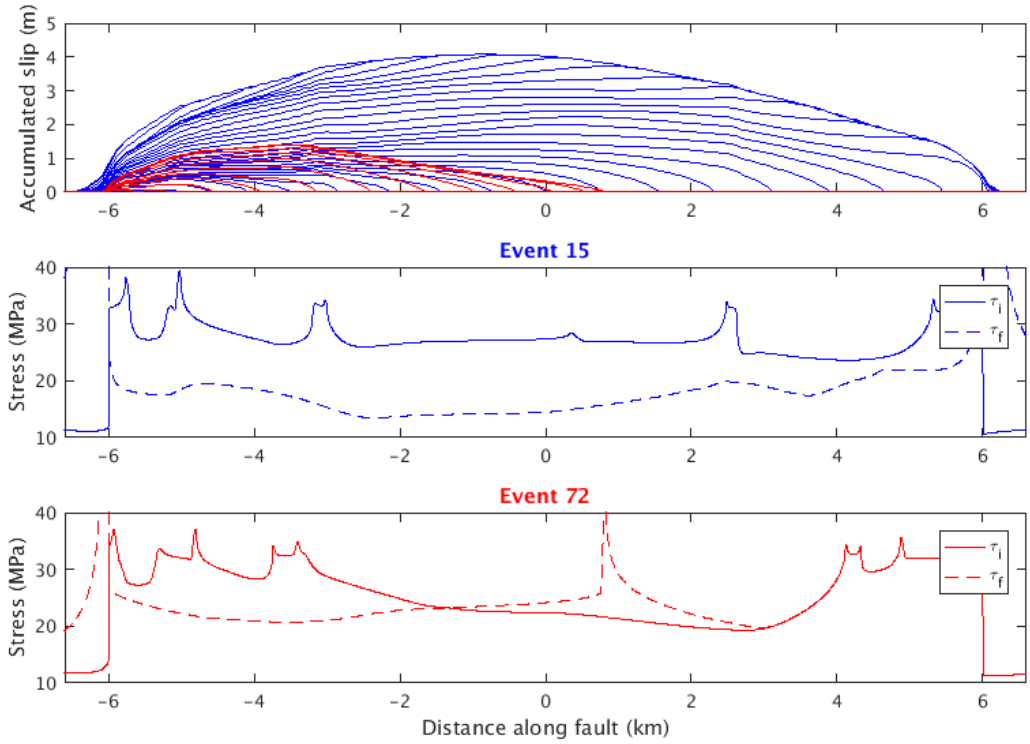

Figure 3.4: Comparison between a complete rupture event (event 15) and partial rupture event (event 72) for the simulation with thermal pressurization and a 12 km long velocity-weakening region. (Top) Accumulated slip profiles for the two events. (Middle and Bottom) Initial and final stress distributions along the fault for each event. The complete rupture event has significantly higher initial stresses and no region of unfavorable prestress, and thus it is able to propagate across the entire fault and into the velocity strengthening region. The partial rupture event has lower initial stress across almost the entire fault and arrests when it reaches the area of lowest prestress.

the simplified theoretical considerations in Rice, 2006.

Comparing G_A to breakdown energy calculated from the average curves G_{curve} we see good, but not perfect agreement (Figure 3.7). This is expected since the averaging process preserves the total strain energy release and the dissipated energy, but not the minimum dynamic level of stress. Therefore, the averaged curve provides a good illustration of G but not the exact value of it. The estimate of breakdown energy from the average curve may underestimate the actual breakdown energy if there is any restrengthening with slip after the minimum shear stress level is reached. Some points on the fault may continuing weakening with slip beyond this slip value, and thus will contribute to the actual breakdown energy. However, the average curve

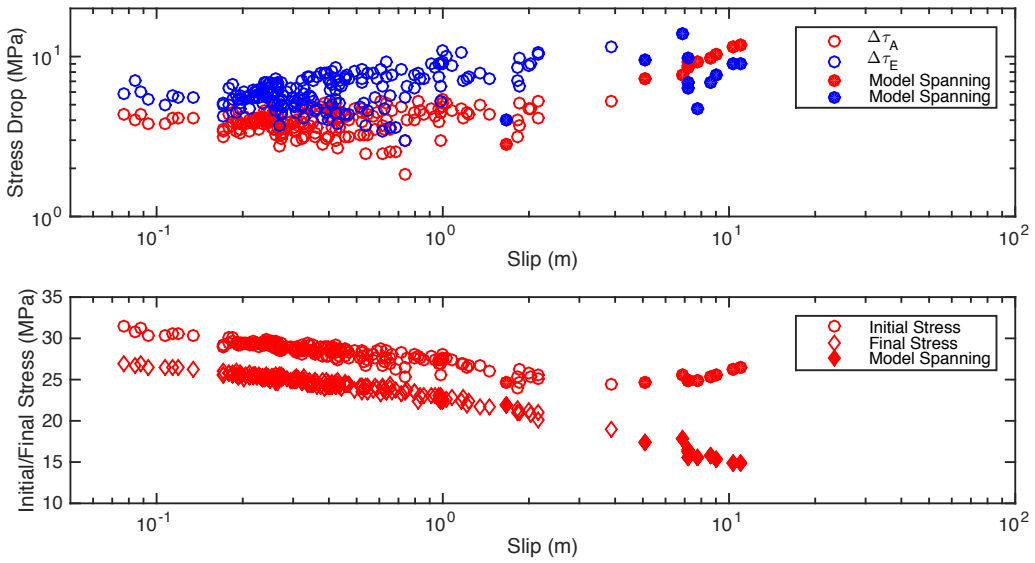

Figure 3.5: top) Stress drops $\overline{\Delta\tau}_A$ and $\overline{\Delta\tau}_E$ for events in the simulation with thermal pressurization and a 24 km long velocity-weakening region. Complete rupture events have filled-in symbols. bottom) Average initial stress $\bar{\tau}_i$ (circles) and final stress $\bar{\tau}_f$ (diamonds) in the simulation with thermal pressurization and a 24 km long fault. Partial rupture events exhibit a decrease in both average initial and final stresses with increasing slip, such that the stress drops are invariant to event size.

shows restrengthening behavior beyond this average slip and thus will not count any of these contributions toward breakdown energy.

3.4 Varying VS properties and effect on stress drop

We further explore how altering the properties of the velocity-strengthening barrier can affect the stress drops of the complete rupture events using six different models (VS1-VS6) with progressively less velocity-strengthening regions (Table 3.2). In other words, the VS regions surrounding the VW seismogenic zone become closer to velocity-neutral. We only alter the properties of the VS region; all other parameters match those from the 12 km model from section 3.3.1 and Tables 2.1 and 3.1. Each model is allowed to produce several complete rupture events and stress drops are plotted against average slip (Figure 3.8 top) and rupture length (Figure 3.8 bottom) for each event.

The model with the most velocity-strengthening regions (VS1) matches the results from our earlier model (section 3.3.1). The stress drops for partial rupture events are magnitude-invariant over about 1 order of magnitude increase in slip. The largest

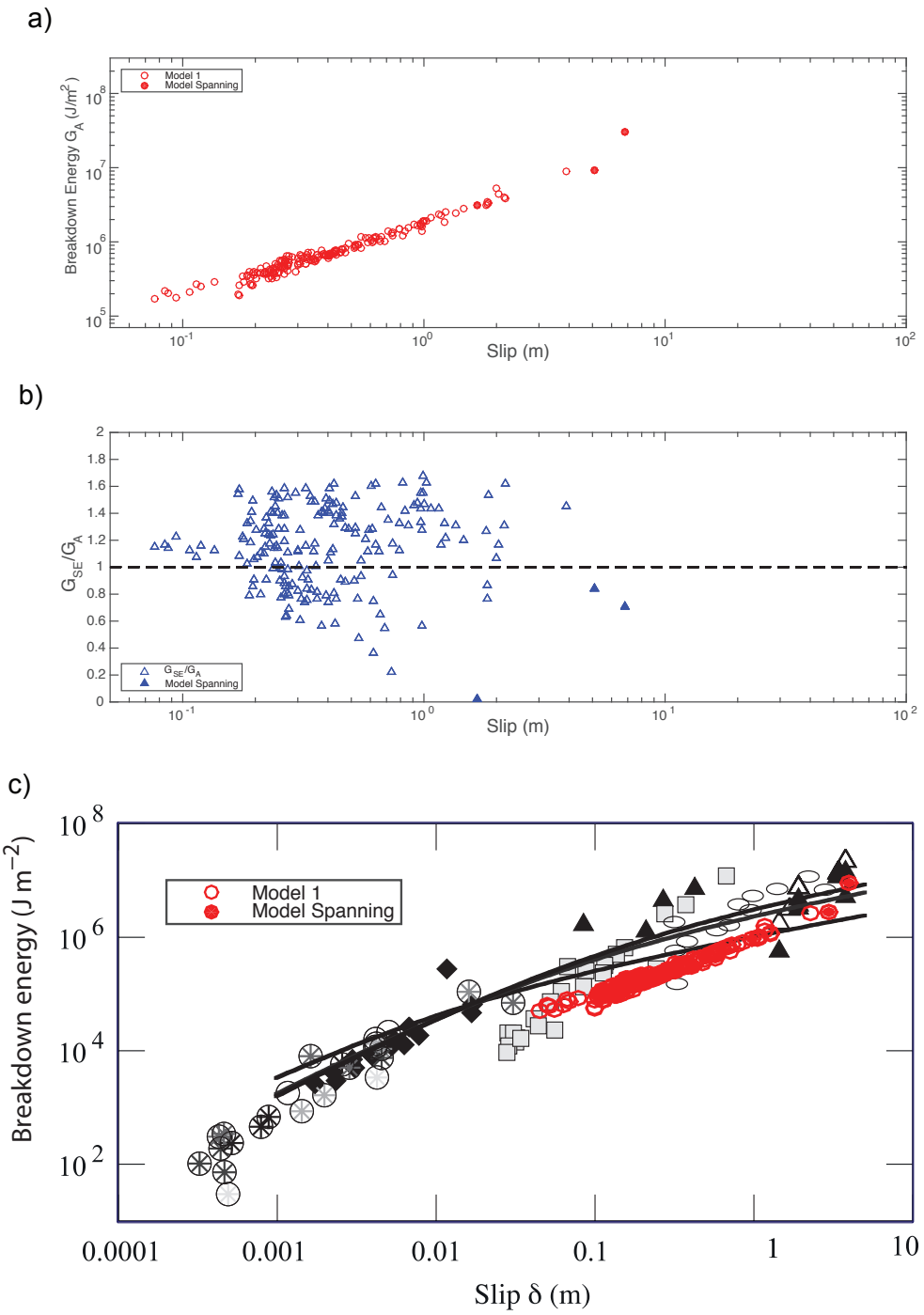

Figure 3.6: a) Breakdown energies G_A for the simulation with thermal pressurization and a 24km VW region. Complete rupture events have filled-in symbols. b) Comparison of seismically estimated breakdown energy G_{SE} to G_A. There is reasonable agreement for the majority of events. c) Breakdown energies from our simulations compared to those inferred for natural events by Rice, 2006. Our models are able to match the trend of the observed events quite well.

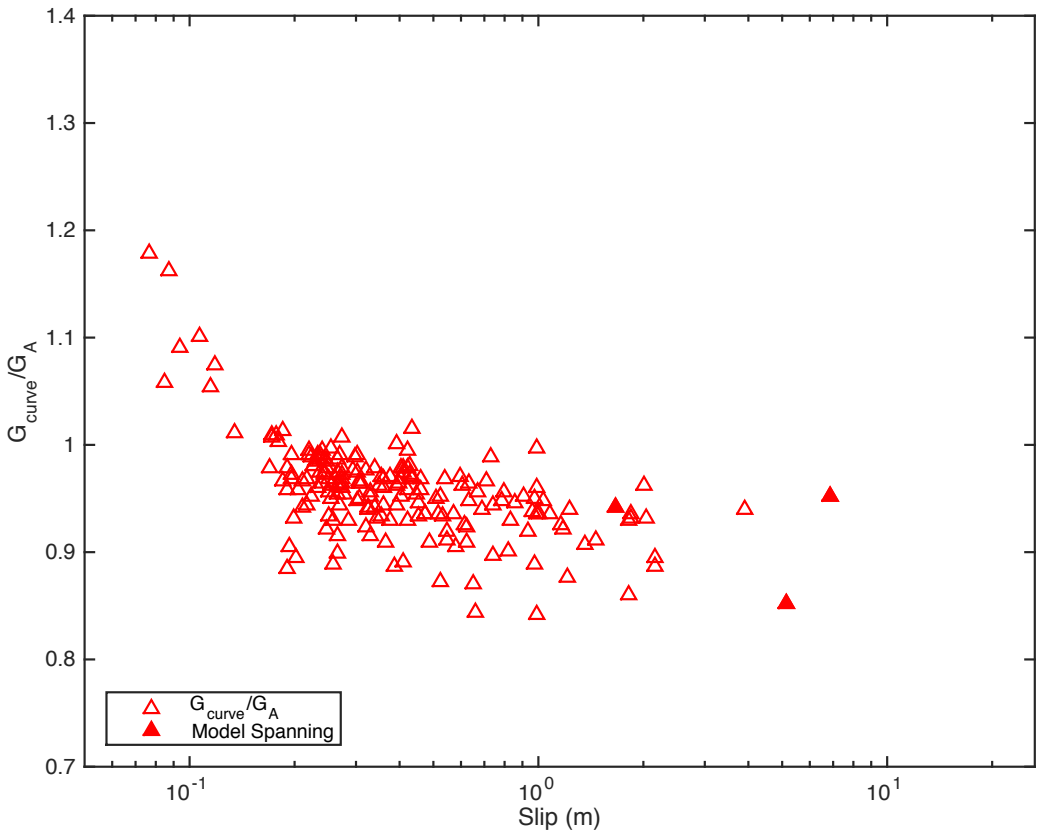

Figure 3.7: Comparison of breakdown energy calculated from the average curves G_{curve} and actual breakdown energy G_A for the 24 km long model. G_{curve} tends to slightly underestimate breakdown energy compared to G_A. As such, the averaged curve provides a good illustration of G but not the exact value of it, as expected.

complete rupture events slip that more are still unable to propagate appreciably further into the velocity-strengthening region (Figure 3.8 bottom). Thus, their stress drops must increase due to larger slip in nearly the same spatial region.

As we decrease the amount of VS in the VS regions, complete rupture events with larger slip propagate further into the VS region and their rupture length increases (Figure 3.8 bottom). Correspondingly, the stress drop of these largest complete rupture events decreases. In fact, for models with the least VS regions (VS4, VS5, and VS6) the trend for the complete rupture events changes from that of stress drop increasing with their size to the decreasing trend. Even the partial rupture events are affected. The smaller, partial rupture, events are able to propagate further into the VS region and thus their average stress drops are decreased. For the two models with the least VS regions (VS5 and VS6), we see stress drop slightly decrease with

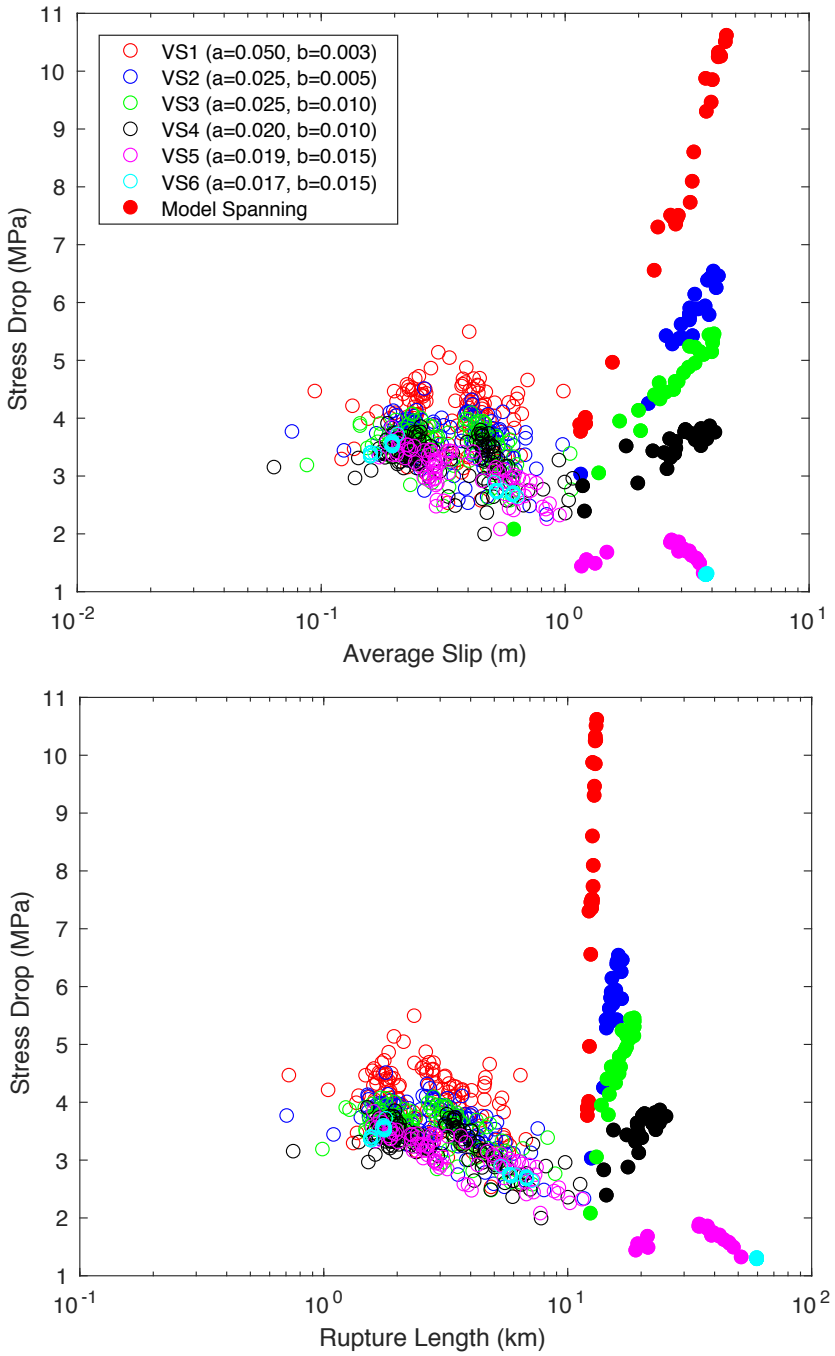

Figure 3.8: Comparison of stress drops for events produced by six different models with a 12 km long VW region surrounded by VS regions of different properties. (top) Stress drops vs. average slip for all events in each of these simulations. Complete rupture events are indicated by filled circles. Stress drops shows a magnitude-invariant trend for VS regions with stronger behavior and a decreasing trend with increasing event size for VS regions with weaker behavior. (bottom) Stress drops vs. rupture length for each event produced in the six simulations. Weaker VS regions allow for greater propagation outside the VW region and thus longer rupture lengths for the complete rupture events.

Table 3.2: Parameters for models of Section 3.4 with different VS properties

Model	a	b	$(a-b)$
VS1	0.050	0.003	0.047
VS2	0.025	0.005	0.020
VS3	0.025	0.010	0.015
VS4	0.020	0.010	0.010
VS5	0.019	0.015	0.004
VS6	0.017	0.015	0.002

increasing event size for all events. The largest events, those that are complete ruptures, also have the lowest stress drops, close to ~1 MPa. It is clear that the properties of the velocity-strengthening region can have a profound effect on the average stress drops. The exact nature of this effect is best studied in 3D models with 2D faults, where the relation of the VS boundary of events to their VW region can be different than in the 1D faults considered in this work.

3.5 Conclusions

We have shown that fully dynamic simulations involving dynamic weakening due to thermal pressurization can explain both the increasing trend in breakdown energy with increasing event size as well as the magnitude-invariant trend with respect to stress drop. Our simulations are able to match the increase in breakdown energy with event size first inferred by Abercrombie and Rice, 2005 and later improved on by Rice, 2006 and Viesca and Garagash, 2015. Similarly, our stress drops are consistent with observations of stress drops in the 1-10 MPa range for all of our event sizes, excluding the complete rupture events in some models.

We follow Rice, 2006, motivated by results of laboratory studies that show the presence of dynamic weakening during seismic slip, and investigate the viability of utilizing dynamic weakening during the event as a mechanism to increase the breakdown energy with event size. Thermal pressurization alone is able to reconcile the increases in breakdown energy while simultaneously keeping stress drops magnitude-invariant. The additional weakening allows breakdown energies to grow with slip and thus with event size. Our calculated breakdown energies G_A match very well the observed trend from Rice, 2006. Furthermore, by looking at average levels of initial and final stresses along the fault, we are able to confirm that with dynamic weakening, larger events will nucleate at lower average levels of prestress. These events will also weaken more than smaller events and arrest at lower levels of final stress. Our simulations reproduce this effect for events ranging several orders

of magnitude in size (5 orders of magnitude in moment and 2 orders of magnitude in slip).

All partial rupture events exhibit magnitude-invariant stress drops, but our complete rupture events do not follow this trend. They are influenced by additional factors that do not affect the smaller and medium sized events, such as being forcibly arrested by the velocity strengthening region. This arises from the fact that the largest events only occur when prestresses are favorable throughout the velocity weakening region. These events never encounter unfavorable prestresses which would inhibit their propagation, and instead are held to a limited rupture domain by the velocity-strengthening regions, no matter their slip. The partial rupture events arrest in the velocity weakening region and do so because they encounter low levels of prestress that inhibit their propagation.

We also find that the properties of the velocity-strengthening region can have an impact on the average stress drop of events that significantly propagate into this region. This is most important for our complete rupture events. We see that varying the VS properties across a range of values is able to produce a range of stress drop behaviors for the largest events. A strong VS region will prevent propagation and lead to sharply increasing stress drops as events slip more, but are unable to increase is physical size. A weak VS region allows for significant propagation and can lead to decreasing stress drops as event size increases. Furthermore, very weak VS regions may lead to lower stress drops overall.

Though our models reproduce magnitude-invariant stress drops, the exact mechanism for this remains unknown and will need to be further investigated in future work.

References

Abercrombie, Rachel E. and James R. Rice (2005). "Can observations of earthquake scaling constrain slip weakening?" In: *Geophysical Journal International* 162, pp. 406–424. DOI: 10.1111/j.1365-246X.2005.02579.x.

Garagash, DI (2012). "Seismic and aseismic slip pulses driven by thermal pressurization of pore fluid". In: *Journal of Geophysical Research: Solid Earth* 117.B4.

Heaton, Thomas H (1990). "Evidence for and implications of self-healing pulses of slip in earthquake rupture". In: *Physics of the Earth and Planetary Interiors* 64.1, pp. 1–20.

Kanamori, Hiroo and Luis Rivera (2006). "Energy Partitioning during an earthquake". In: *Earthquakes: Radiated energy and the physics of faulting*, pp. 3–13.

Noda, Hiroyuki and Nadia Lapusta (2010). "Three-dimensional earthquake sequence simulations with evolving temperature and pore pressure due to shear heating: Effect of heterogeneous hydraulic diffusivity". In: *Journal of Geophysical Research* 115, B123414. DOI: 10.1029/2010JB007780.

Noda, Hiroyuki, Nadia Lapusta, and Hiroo Kanamori (2013). "Comparison of average stress drop measures for ruptures with heterogeneous stress change and implications for earthquake physics". In: *Geophysical Journal International*. DOI: 10.1093/gji/ggt074.

Rempel, Alan W and James R Rice (2006). "Thermal pressurization and onset of melting in fault zones". In: *Journal of Geophysical Research: Solid Earth* 111.B9.

Rice, James R. (2006). "Heating and weakening of faults during earthquake slip". In: *Journal of Geophysical Research* 111, B05311. DOI: 10.1029/2005JB004006.

Sibson, R. H. (1973). "Interactions between temperature and pore-fluid pressure during earthquake faulting and a mechanism for partial or total stress relief." In: *Nature* 243.126, pp. 66–68.

Viesca, Robert C. and Dmitry I. Garagash (2015). "Ubiquitous weakening of faults due to thermal pressurization". In: *Nature Geoscience* 8, pp. 875–879. DOI: 10.1038/NGEO2554.

Wibberley, Christopher AJ and Toshihiko Shimamoto (2005). "Earthquake slip weakening and asperities explained by thermal pressurization". In: *Nature* 436.7051, pp. 689–692.

Chapter 4

ESTIMATES OF BREAKDOWN ENERGY AND RADIATION EFFICIENCY: INSIGHTS FROM NUMERICAL EARTHQUAKE SOURCE MODELS

Here we investigate the earthquake energy budget beyond just the breakdown energy. We utilize both standard rate-and-state models as well as some with enhanced dynamic weakening to reproduce a variety of rupture behaviors and see how these behaviors affect seismically estimated quantities such as breakdown energy G, available energy ΔW_0, and radiation ratio η.

4.1 Motivation and notion of available energy: actual and idealized

Let us recall the energy budget from Chapter 1:

$$\Delta W = E_G + E_R + E_F, \tag{4.1}$$

which can be written per unit area as:

$$\Delta W/A = G + E_R/A + E_F/A. \tag{4.2}$$

The breakdown energy G is the part of the dissipated energy that affects the dynamics of the rupture, the so-called frictionally dissipated energy E_F is the rest of the dissipated energy and is related to heat generated on the fault, and the radiated energy E_R describes how much energy is radiated away from the rupture. The total strain energy released per unit area on the fault $\Delta W/A$ is given by:

$$\Delta W/A = \frac{1}{2}(\bar{\tau}_i + \bar{\tau}_f)\bar{\delta}, \tag{4.3}$$

where $\bar{\tau}_i$ is the average initial stress, $\bar{\tau}_f$ is the average final stress, $\bar{\delta}$ is the average final slip, and A is the fault area. Thus, calculating the total strain energy released requires knowing the absolute stress levels on faults, which remains elusive.

One possible solution (Venkataraman and Kanamori, 2004) is to consider the available energy, i.e. the total energy available for both the breakdown process and for radiation:

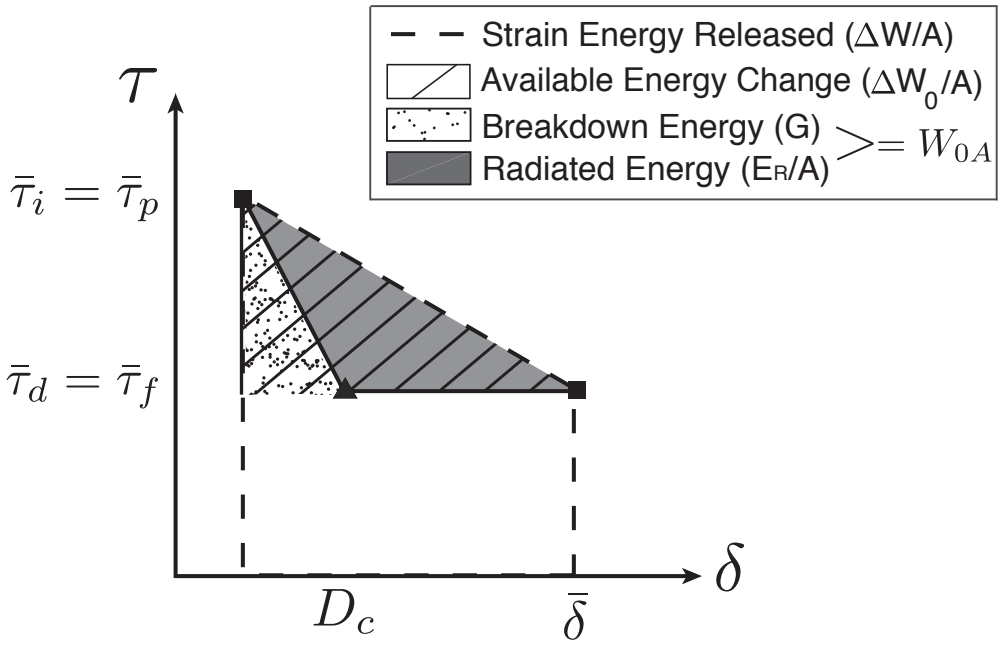

Figure 4.1: Idealized view of earthquake energy budget showing slip weakening behavior from an initial stress $\bar{\tau}_i$, equal to $\bar{\tau}_p$, down to a dynamic level of stress $\bar{\tau}_d$, equal to $\bar{\tau}_f$ over the slip weakening distance D_c. The total strain energy released (area encompassed by dotted lines) is defined to be the sum of breakdown energy G, radiated energy E_R, and frictionally dissipated energy E_F (unshaded area under the curve). Seismically estimated available Energy ΔW_0 can be neatly divided into breakdown energy G and radiated Energy E_R in this idealized case. Actual available energy ΔW_{0A} is the sum of G and E_R/A.

$$\Delta W_{0A}/A = G + E_R/A, \tag{4.4}$$

where W_{0A} is the actual available energy per unit area for the event given as the sum of breakdown energy per unit area G and radiation energy per unit area E_R/A. We can compare the relative magnitudes of breakdown and radiated energy through a radiation ratio (Noda et al., 2013), often called radiation efficiency (Venkataraman and Kanamori, 2004).

$$\eta_A = \frac{E_R/A}{G + E_R/A} = \frac{E_R}{\Delta W_{OA}}, \tag{4.5}$$

where η_A is the (actual) radiation ratio. These quantities are rigorously defined, but their observability for natural events is an important question.

Indeed, it is possible to determine the available energy given an idealized energy budget (Venkataraman and Kanamori, 2004; Kanamori and Rivera, 2006; Kanamori and Heaton, 2000; etc.) (Figure 4.1). In this idealized case, the shear stress evolution follows simplified linear slip weakening where stress drops linearly from an initial value $\bar{\tau}_i$ until slip reaches a critical value D_c, at which the stress remains constant $\bar{\tau}_d$ for the remainder of slip, with $\bar{\tau}_f = \bar{\tau}_d$. The available energy is the sum of the breakdown energy G (dotted area) and the radiated energy E_R/A (shaded area). Thus, in this idealized case, the available energy may be written as:

$$\Delta W_{0A} = G_A + E_R/A = \frac{1}{2}\overline{\Delta\tau}\bar{\delta}A = \Delta W_0, \tag{4.6}$$

where ΔW_0 is the seismically estimated available energy, a quantity that depends on seismically observable quantities such as stress drop $\overline{\Delta\tau}$ and average final slip $\bar{\delta}$. We can define the seismically estimated radiation ratio to compare the magnitudes of breakdown energy and radiated energy in this idealized case:

$$\eta = \frac{E_R}{\Delta W_0} = \frac{E_R}{\frac{1}{2}(\bar{\tau}_i - \bar{\tau}_f)\bar{\delta}A}. \tag{4.7}$$

This quantity can be, and has been, estimated from seismological observations (Venkataraman and Kanamori, 2004; Ye et al., 2016) because it does not depend on any absolute value of stress, but instead depends on the stress drop produced by the event, the radiated energy, average final slip, and rupture area, all of which may be inferred from seismic observations.

4.1.1 General View of Earthquake Energy Budget

However, as we have seen in Chapters 2 and 3 (Figure 4.2), the fault behavior during seismic events is always more complex. The initial stress is not equal to the peak stress experienced at the onset of slipping. The final average shear stress is not the same as the dynamic level of shear stress. This can be due to either overshoot (Figure 4.2a), as is often the case for crack-like ruptures, or undershoot (Figure 4.2b), as is typical for pulse-like events (McGarr, 1999; Kanamori and Rivera, 2006; Viesca and Garagash, 2015). Enhanced dynamic weakening can occur at seismic slip rates and cause shear stress to continue to decrease with accumulating slip instead of dropping to a constant dynamic level (Sibson, 1973; Wibberley and Shimamoto, 2005; Rice, 2006).

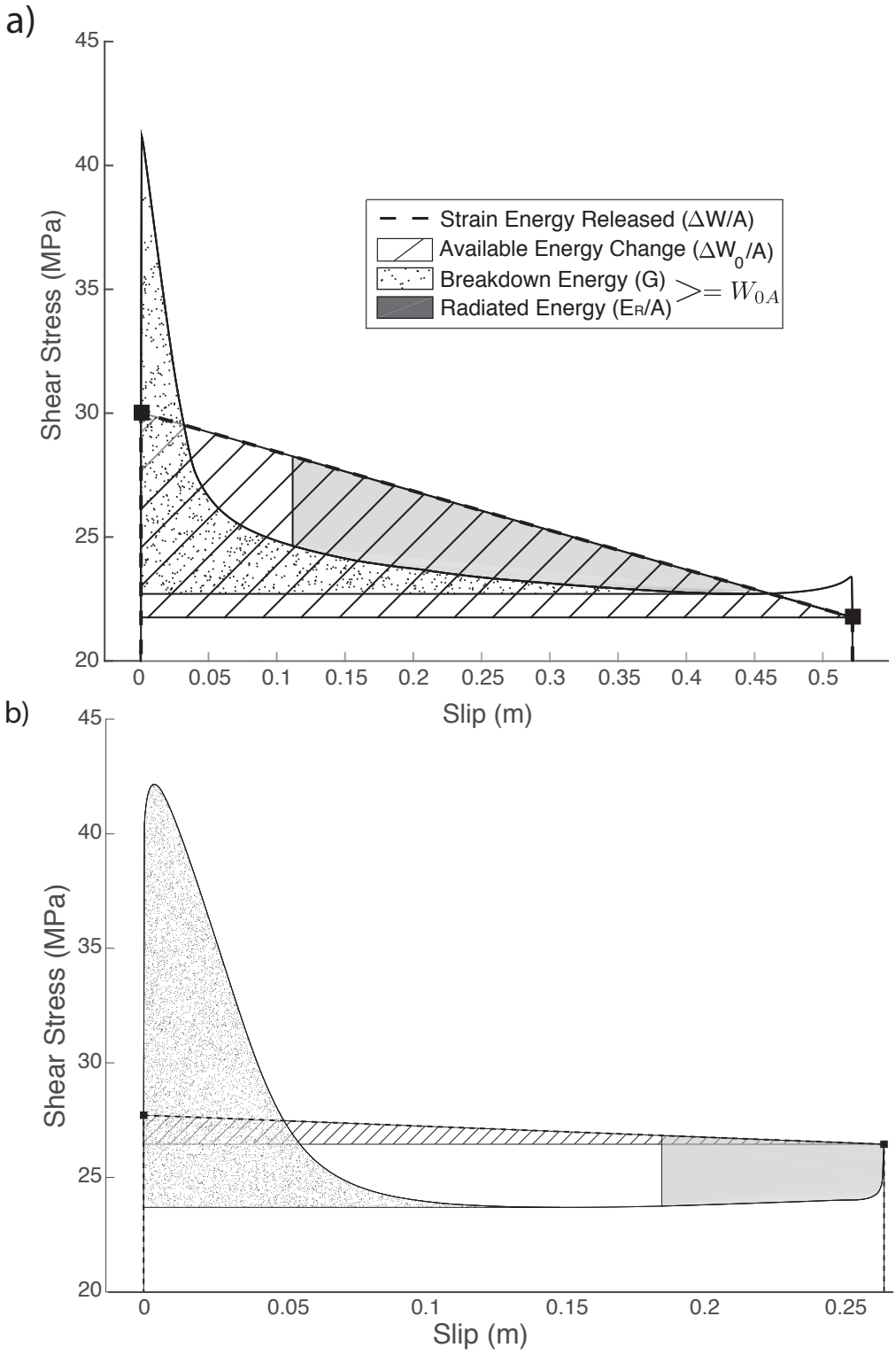

Figure 4.2: Representative rupture behaviors that differ from the idealized model. a) Crack-like event with thermal pressurization that allows for continuous weakening. This event experiences a small stress overshoot at arrest as well as a strength excess during initial slip. b) Pulse-like event with flash heating present. This event shows a much larger stress undershoot at arrest. The initial increase in stress leads to a much larger (relatively) region of breakdown energy above the small hatched area of seismically estimated available energy.

The average shear stress vs. slip curve can vary greatly depending the specific rupture behavior (crack-like vs. pulse-like, dynamic weakening vs. no additional weakening, negligible strength excess vs. large strength excess). Let us consider several different simplified rupture behaviors and see the effect on actual available energy ΔW_{0A} and seismically estimated available energy ΔW_0 (Figure 4.3). The actual available energy ΔW_{0A} is rigorously defined as:

$$\Delta W_{0A}/A = \Delta W/A - E_F/A. \tag{4.8}$$

As discussed previously, frictionally dissipated energy E_F is defined to be energy dissipated below the lowest dynamic level of shear stress $\bar{\tau}_d$ reached on the fault. Thus, the actual available energy per unit area ΔW_{0A} can be rewritten as:

$$\Delta W_{0A}/A = \frac{1}{2}(\bar{\tau}_i + \bar{\tau}_f)\bar{\delta} - \bar{\tau}_d\bar{\delta}. \tag{4.9}$$

This expression for the actual available energy is accurate as long as the fault does not recover from the minimum level of dynamic stress appreciably before the final slip (Figure 4.3 a, c-e). Our generalized shear stress vs. slip evolution with dynamic weakening (Figure 4.3b) illustrates extra dissipated energy after the minimum dynamic level of stress is reached (darker shaded region). Equation (4.9) is valid as long as this area is negligible compared to W_{0A}.

There may also be some extra energy dissipated after the fault reaches its minimum dynamic level of stress if it restrengthens with slip rather than only at the final slip. This can be seen in our schematic of a general rupture behavior (Figure 4.3) and should contribute to frictionally dissipated energy, but we will see that for our simulations this effect is normally negligible compared to the other energy quantities.

If the rupture behavior includes a stress undershoot $\gamma\overline{\Delta\tau}$ (Figure 4.3c), as occurs in all pulse-like ruptures, the actual available energy may be written in terms of the stress undershoot and the seismically estimated available energy ΔW_0:

$$\begin{aligned} \Delta W_{0A}/A &= \frac{1}{2}\overline{\Delta\tau}\bar{\delta} + (\bar{\tau}_f - \bar{\tau}_d)\bar{\delta}. \\ \Delta W_{0A}/A &= \Delta W_0/A + \gamma\overline{\Delta\tau}\bar{\delta} \end{aligned} \tag{4.10}$$

$$\frac{\Delta W_{0A}}{\Delta W_0} = 1 + 2\gamma. \tag{4.11}$$

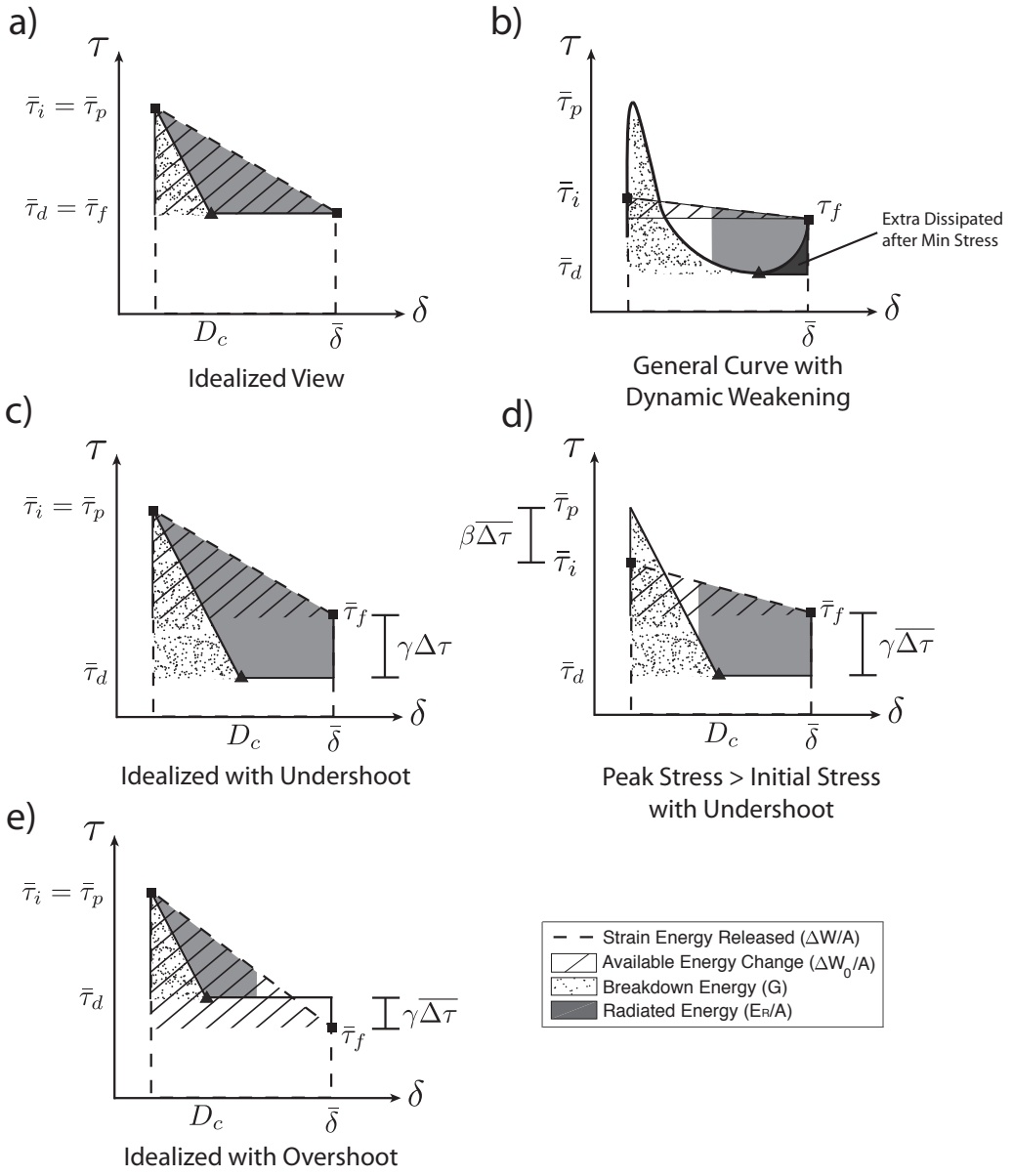

Figure 4.3: Various possible stress vs. slip behaviors. These different behaviors can have a large effect on the accuracy of seismically estimated available energy ΔW_0 as well as various methods of calculating G. a) Idealized view of the earthquake energy budget from Figure 4.1. b) More general event with strength excess, non-constant dynamic level of stress, and restrengthening that occurs before the final slip of the event. In this event there is additional dissipated energy released after the fault reaches the minimum level of dynamic shear stress. c) Idealized view with an additional stress undershoot $\gamma\Delta\tau$ at the end of slip. d) An event with both initial strength excess and stress undershoot at final slip. e) Idealized view with an additional stress overshoot $\gamma\Delta\tau$ at the end of slip.

If $\gamma = 0$, we have the idealized case (Figure 4.3a) and $\Delta W_{0A} = \Delta W_0$. If there is a non-negligible undershoot (Figures 4.3c, d), then $\gamma > 0$ and $\Delta W_{0A} > \Delta W_0$. Thus, if we have an undershoot comparable to the average stress drop ($\gamma = 1$), actual available energy ΔW_{0A} is three times larger than seismically estimated available energy ΔW_0. An undershoot twice larger than the average stress drop ($\gamma = 2$) leads to available energy ΔW_{0A} being five times larger than the seismically estimated available energy ΔW_0. These values of γ are reasonable based on pulse-like ruptures from our simulations, as demonstrated later.

Note that rupture behavior with the strength excess $\beta\overline{\Delta\tau}$, the increase from initial average stress to the peak level of stress ($\bar{\tau}_p - \bar{\tau}_i$), (Figure 4.3d) does not alter the available energy. This initial increase affects how available energy is partitioned into breakdown energy G and radiated energy E_R/A, but does not change the actual available energy ΔW_{0A} of the rupture. The strength excess increases the breakdown energy G at the expense of radiated energy E_R/A.

The same argument can be made for rupture behaviors with an overshoot (Figure 4.3e), as is often the case with crack-like ruptures, and Equation (4.11) still applies. This behavior would result in $\Delta W_{0A} < \Delta W_0$, but in most simulations, including ours, $|\gamma| << 1$ for crack-like ruptures, and thus $\Delta W_{0A} \sim \Delta W_0$.

4.1.2 Seismic estimates of breakdown energy: G_{SE}, G_{DFE}, and G_{Max}

There have been attempts to estimate breakdown energy G for natural events based on the seismically estimated available energy ΔW_0 and assuming behaviors similar to the idealized, slip-weakening version of the energy budget (Abercrombie and Rice, 2005). it is assumed that the contribution due to strength excess ($\bar{\tau}_p - \bar{\tau}_i$) is negligible. Using a similar definition for energies to our idealized model, they subtract the radiated energy E_R/A from the seismically estimated available energy ΔW_0, thus leading to the seismically estimated contribution of breakdown energy G'. We title this quantity G_{SE} for "seismically estimated" breakdown energy:

$$G_{SE} = \Delta W_0/A - E_R/A. \tag{4.12}$$

Substituting values that can be inferred seismically, we get:

$$G_{SE} = \frac{1}{2}\bar{\delta}\left(\overline{\Delta\tau} - \frac{2\mu E_R}{M_0}\right), \tag{4.13}$$

where $\overline{\Delta\tau}$ is the average stress drop of the event, μ is the shear modulus, and M_0 is the seismic moment of the event. The seismically estimated breakdown energy has been shown to agree well (within a factor of 2) with the true breakdown energy G for crack-like events with thermal pressurization (Chapter 3). If the seismically estimated available energy ΔW_0 underestimates the actual available energy ΔW_{0A}, and we still subtract off the actual radiated energy E_R/A, then we are left with a significant underestimation of the true breakdown energy G.

To obtain another estimate of G, let us consider:

$$\begin{aligned} G &= \Delta W_{0A}/A - E_R/A \\ G &= \Delta W_0/A + \gamma\overline{\Delta\tau}\bar{\delta} - E_R/A \\ G &= G_{SE} + (\bar{\tau}_f - \bar{\tau}_d). \end{aligned} \tag{4.14}$$

To distinguish this expression of G from others, we call it G_{DFE} (based on the dynamic and final levels of stress):

$$G_{DFE} = G_{SE} + (\bar{\tau}_f - \bar{\tau}_d)\bar{\delta}. \tag{4.15}$$

G_{DFE} accounts for a stress undershoot or overshoot, and hence provides the closest estimate to the actual G, not accounting only for the extra part of E_F that can occur during restrengthening after the fault has reached its minimum level of dynamic shear resistance (Figure 4.3b, dark grey region). If this portion of E_F is negligible compared to the actual available energy ΔW_{0A}, then $G_{DFE} = G$. However, this estimate for G requires knowing the absolute level of final stress and the dynamic level of stress during the event.

The work of Viesca and Garagash, 2015 used (Equation 4.15) (without linking it to the concept of available energy), and additionally assumed a complete coseismic strength loss ($\tau_d = 0$) during large pulse-like events. Thus, they define G_{max} as:

$$\begin{aligned} G_{max} &= G_{DFE}|_{\tau_d=0}, \\ G_{max} = G_{SE} + \bar{\tau}_f\bar{\delta} &= \frac{1}{2}\bar{\delta}\left(\overline{\Delta\tau} - \frac{2\mu E_R}{M_0}\right) + \bar{\tau}_f\bar{\delta}. \end{aligned} \tag{4.16}$$

To calculate G_{max}, the absolute final stress on the fault still must be known, but the dynamic level of stress no longer needs to be found. Viesca and Garagash (2015)

assume $\bar{\tau}_f = 15 - \overline{\Delta\tau}$ where the stresses are in MPa. Note that G_{max} can dramatically overestimate G if the fault does not weaken to zero strength.

4.1.3 Actual and Seismically Estimated Radiation Ratios

As discussed in section 4.1, one can define $\eta = E_R/\Delta W_0$ and $\eta_A = E_R/\Delta W_{0A}$. Note that $0 \leq \eta_A \leq 1$ by definition, but η can in principle exceed 1. In that sense, η_A can be called radiation efficiency but η is more accurately radiation ratio. For example, if the fault experiences a stress undershoot of magnitude $\gamma\overline{\delta\tau}$ (Figure 4.3c), then:

$$\begin{aligned} \Delta W_0/A &= \frac{1}{2}\overline{\Delta\tau}\bar{\delta} \\ E_R/A &= \frac{1}{2}\overline{\Delta\tau}\bar{\delta} + \gamma\overline{\Delta\tau}\bar{\delta} - \frac{1}{2}(1+\gamma)D_c \\ \eta &= \frac{E_R}{\Delta W_0} = 1 + 2\gamma - (1+\gamma)D_c/\bar{\delta}. \end{aligned} \tag{4.17}$$

Thus, E_R will exceed ΔW_0 for any undershoot such that:

$$\gamma > \frac{D_c/\bar{\delta}}{2 - D_c/\bar{\delta}}. \tag{4.18}$$

This leads to negative G_{SE} (unphysical) and a radiation ratio $\eta > 1$. If $\gamma > 1$, meaning the undershoot is larger than the average stress drop, then the stress undershoot is large enough that E_R will always exceed ΔW_0, no matter the slip-weakening distance D_c. Consistent with the discussion in section 4.1.2, if $\Delta W_0 \approx \Delta W_{0A}$, as is the case for crack-like ruptures, $\eta \approx \eta_A$. But, for pulse-like ruptures, we expect $\eta_A < \eta$.

4.2 Fault Models and Additional Dynamic Weakening Due to Flash Heating

We consider several fault models that produce crack-like, crack-to-pulse-like, and pulse-like ruptures and analyze their energy budget to check the relationships discussed in section 4.1. Our simulations follow the same development as those from Chapters 1 and 2. Model 1 of this chapter is governed by the standard rate-and-state friction with $L = 2$ mm and no additional dynamic weakening. Models 2 and 3 utilize thermal pressurization with parameters motivated by prior studies (Rice, 2006, Noda and Lapusta, 2010).

In addition to thermal pressurization, we also consider enhanced dynamic weakening due to flash heating (Rice, 2006). This effect occurs when the tips of fault gouge grains heat up during a seismic event and weaken dynamically. This process is

often modeled with a characteristic slip velocity V_w at which flash heating activates. The friction coefficient then drops to a residual level f_w and remains there. To model flash heating, we make slight modifications to our steady state rate-and-state equations to take into account the weakening following, Noda, 2008:

$$f_{ss}(V) = f(V, \theta_{ss}(V)) = \frac{f(V, L/V) - \frac{V}{|V|} f_w}{1 - |V|/V_w} + \frac{V}{|V|} f_w \tag{4.19}$$

$$\frac{d\theta}{dt} = \frac{V\theta_{ss}(V)}{L} - \frac{V\theta}{L} = \frac{V}{L}(\theta_{ss}(V) - \theta), \tag{4.20}$$

where V is the slip rate on the fault, V_w is the characteristic slip velocity at which flash heating becomes effective, and f_w is the residual friction coefficient. Model 3 utilizes flash heating in addition to thermal pressurization, and Model 4 has only a stronger form of flash heating. Parameters for all models are given in Tables 2.1 and 4.1. We also include a sample event from an extended version of Model 3 that includes a 100 km VW region. This type of larger model is computationally challenging and will be further analyzed in future work.

Table 4.1: Parameters for Models Investigating Available Energy

Parameter	Symbol	Model 1	Model 2	Model 3	Model 4
Characteristic slip velocity	V_w	-	-	0.6 m/s	0.14 m/s
Residual friction coefficient	f_w	-	-	0.45	0.01
Thermal diffusivity	α_{th}	-	10^{-6} m^2/s	10^{-6} m^2/s	-
Hydraulic diffusivity	α_{hy}	-	10^{-3} m^2/s	10^{-3} m^2/s	-
Coupling coefficient	Λ	0 MPa/K	0.1 MPa/K	0.1 MPa/K	0 MPa/K

4.3 Results

Models 1, 2, and 3 produce both crack-like events, pulse-like events with relatively broad pulses, and events with behavior somewhat transitory between a crack and a pulse. Model 4 produces sharp pulse-like events. We investigate the energy budget, specifically the actual available energy ΔW_{0A}, seismically estimated available energy ΔW_0, and breakdown energies, and the relation between them for different rupture modes.

4.3.1 Crack-Like Events

Our standard rate-and-state model (Model 1) and the two models that include thermal pressurization (Model 2 and Model 3) produce many events that are crack-like

(Figures 4.4, 4.5, 4.6). We have shaded a section of slip, accumulated with 0.1 seconds (Figures 4.4 and 4.6) or within 0.5 seconds (Figure 4.5), for each event (Row 1 of each figure) in order to illustrate their crack-like behavior.

The initial stress (Row 2), final stress (Row 2), and stress drop (Row 3) distributions illustrate the variability of the stress state on the fault before and after the event. As in Chapters 2 and 3, we illustrate the average overall behavior using the average curve (Row 4). Energy quantities from the earthquake energy budget are labeled in the same fashion as in Figure 4.3. Note that the areas representing E_F/A and total strain energy released $\Delta W/A$ extend all the way down to zero shear stress; the figures are cropped for clarity.

In Model 1, seismically estimated available energy $\Delta W_0 = 0.42$ MJ/m^2 is a reasonable approximation for the actual available energy ΔW_{0A} ($\Delta W_{0A}/\Delta W_0 = 0.9$). The slight discrepancy here is due to some restrengthening before final slip. Though this event does experience some restrengthening, it is relatively small (0.01 MJ/m^2) compared to the actual available energy $\Delta W_{0A} = 0.38$ MJ/m^2.

G_A, G_{curve}, and G_{DFE} all agree quite well for this event, producing values around 0.27 MJ/m^2. $G_{SE} = 0.31$ MJ/m^2 slightly overestimates the breakdown energy as expected but is still quite good. G_{Max} is more than an order of magnitude larger, due to the event operating at about 26 MPa rather than experiencing a complete strength drop, but the G_{Max} approximation is not intended for use in such cases. The seismically estimated radiation ratio η is a reasonable value, 0.26; actual radiation ratio $\eta_A = 0.29$ is also similar.

4.3.2 Transition Between Crack and Pulse-Like Events

Models 1, 2, and 3 also produce events that transition from crack-like behavior into more pulse-like behavior as slip is accumulated. Three such events are shown in Figures 4.8, 4.7, and 4.9.

In the sample event from Model 2 (Figure 4.7), the shaded slip (Row 1) approximately illustrates the stage during the event that the rupture shifts from crack-like to pulse-like behavior. The initial stress (Figure 4.7, Row 2) is higher in the region of the crack-like behavior and this leads to a higher stress drop in this region, 5 - 10 MPa, similar to the crack-like events from the previous section. As the event propagates to the right, into lower initial stress, it transitions into a more pulse-like rupture. The stress drops in this region are smaller to negative. This combined crack-like to pulse-like behavior likely results in the small amount of restrengthening present

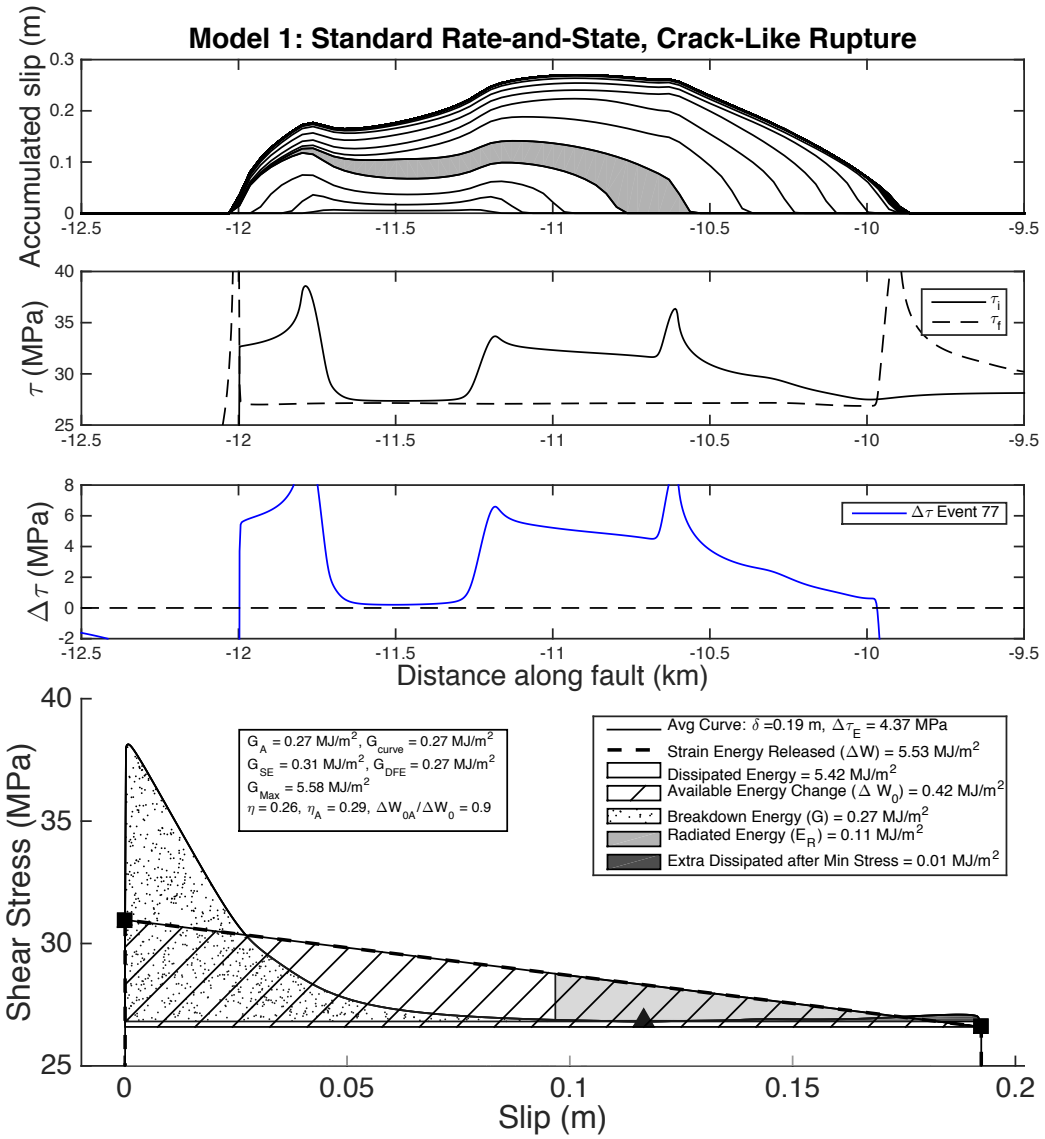

Figure 4.4: Sample event from model 1 showing crack-like behavior. Row 1) Accumulated slip profile with slip distribution along the fault plotted every 0.1 seconds. A portion of slip accumulated is shaded to emphasize the crack-like behavior. Row 2) Initial and final shear stress distributions along the fault. Row 3) Stress drop distribution along the fault. Row 4) Average shear stress vs. slip curve with relevant energy quantities labeled. Initial and final stresses are marked with black squares. The minimum dynamic level of shear stress is marked with a black triangle. The event exhibits slight overshoot and, as derived in section 4.1, the actual available energy ΔW_{OA} is slightly smaller than the seismically estimated ΔW_0, with their ratio being 0.9. However, $\Delta W_{0A}/\Delta W_0$ is ~1, and G_{SE} gives a good approximation for G_A.

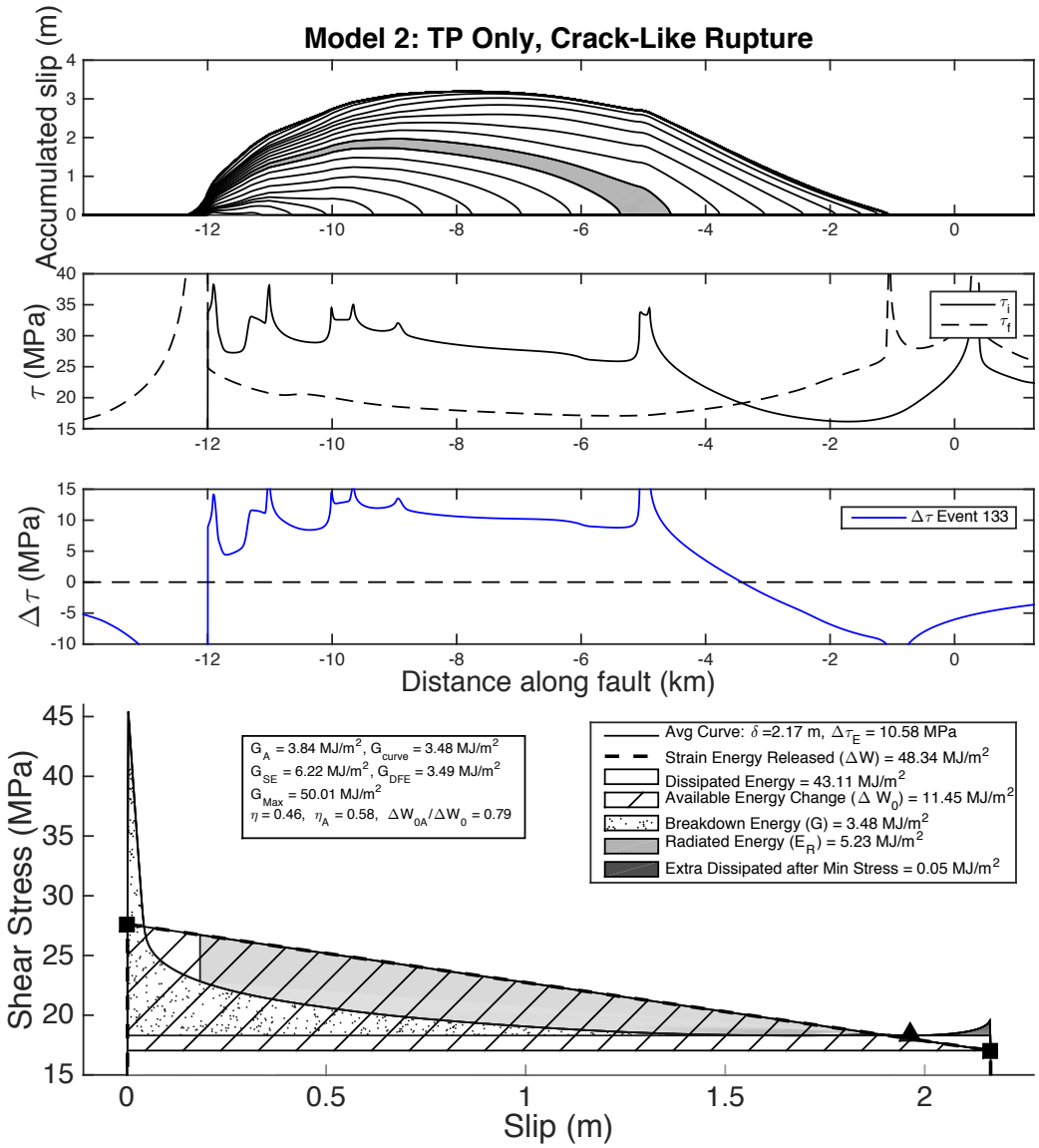

Figure 4.5: Representative event from model 2 showing crack-like behavior. Row 1) Accumulated slip profile with slip distribution along the fault plotted every 0.5 seconds. Row 2) Initial and final stress distributions along the fault. Row 3) Stress drop distribution along the fault. Row 4) Average shear stress vs. slip curve with relevant energy quantities labeled. Initial and final stresses are marked with black squares. The minimum dynamic level of shear stress is marked with a black triangle, and is higher than the final stress, due to a small stress overshoot. Correspondingly, the actual available energy ΔW_{OA} is smaller than the seismically estimated ΔW_0, with their ratio being 0.79. G_{SE} overestimates G_A by about a factor of 1.5.

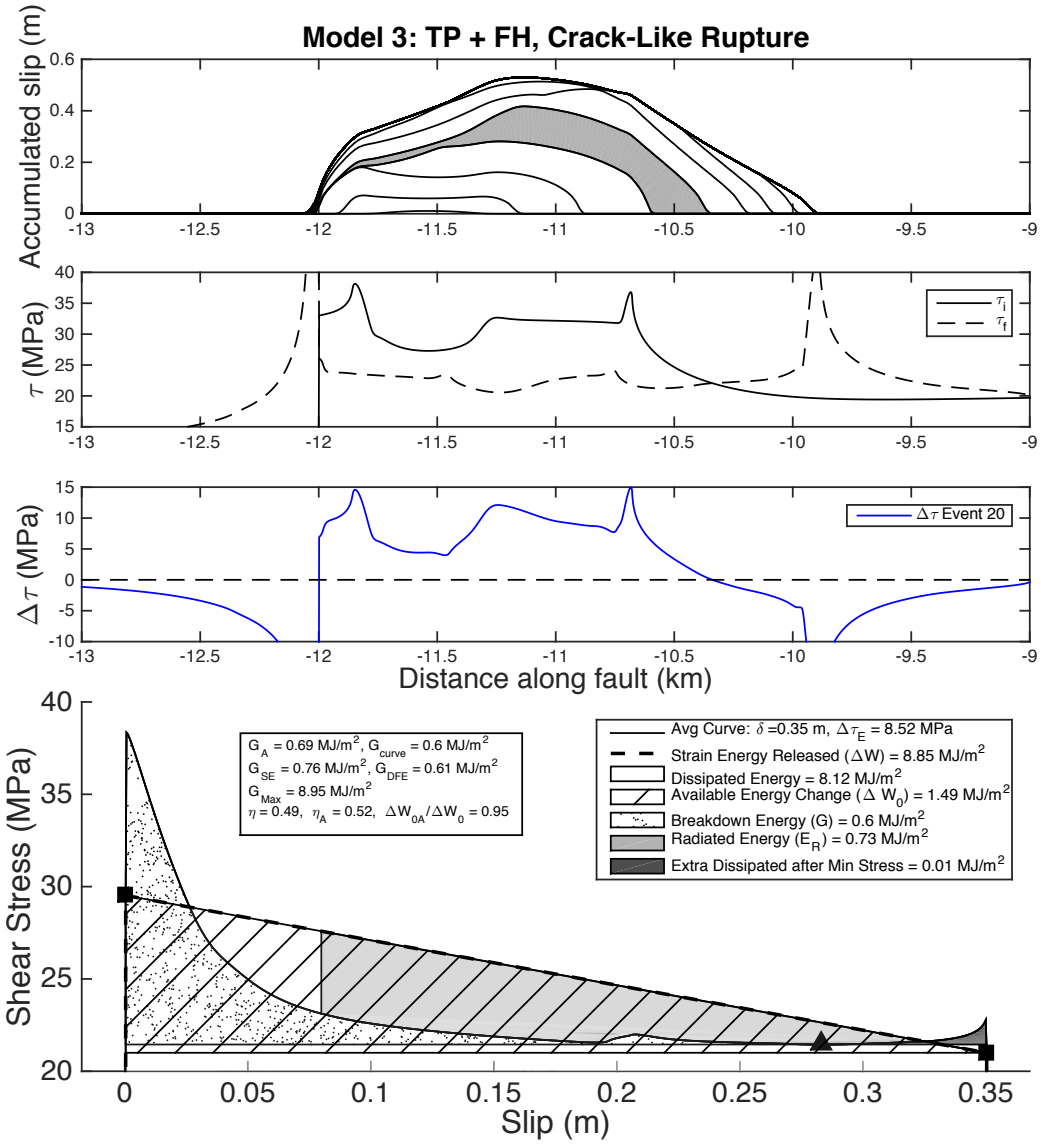

Figure 4.6: Representative event from model 3 showing crack-like behavior. Row 1) Accumulated slip profile with slip distribution along the fault plotted every 0.1 seconds. A portion of slip accumulated in the same time period is shaded to emphasize the crack-like behavior. Row 2) Initial and final stress distributions along the fault. Row 3) Stress drop distribution along the fault. Row 4) Average shear stress vs. slip curve with relevant energy quantities labeled. Initial and final stresses are marked with black squares. The minimum dynamic level of shear stress is marked with a black triangle and is greater than the average final stress due to a small overshoot. $\Delta W_{0A}/\Delta W_0$ is < 1. Again, G_{SE} slightly overestimates G_A.

near the end of slip, resulting in small undershoot. In this case, the seismically estimated available energy ΔW_0 = 2.6 MJ/m^2 is smaller than the actual available energy ΔW_{0A} = 3.3 MJ/m^2. This ~30% difference manifests itself when calculating the seismically estimated breakdown energy G_{SE} = 0.92 MJ/m^2, as G_{SE} is nearly only half of the actual breakdown energy G_A (G_{curve} and G_{DFE} agree well with G_A as expected). While this difference is still relatively small, the disparity is greater than for the events with more crack-like behavior discussed in the previous section. Although G and E_R sum to be larger than ΔW_0, they are each individually smaller than ΔW_0. In part, the radiation ratio η = 0.65 is reasonable and less than 1 and the actual radiation ratio η_A = 0.51.

The event from Model 1 (Figure 4.8), shows a similar transition from crack-like to more pulse-like behavior. However, in this event the minimum dynamic shear stress is reached relatively early in the event, and the fault mildly restrengthens for nearly 80% of the total slip (Row 4). The extra dissipated energy after the event reaches its minimum stress is shaded in darker gray. Though the rupture restrengthens a relatively small amount of shear stress, the relatively large amount of slip over which this occurs increases the amount of this extra dissipated energy (0.06 MJ/m^2). Due to the early restrengthening, the seismically estimated available energy ΔW_0 = 0.57 MJ/m^2 is less than the actual available energy ΔW_{0A} = 0.70 MJ/m^2 ($\Delta W_{0A}/\Delta W_0$ = 1.23, and thus G_{SE} underestimates G_A by about a factor of 2.

The event from Model 3 (Figure 4.9), also shows early restrengthening even with both thermal pressurization and flash heating present. However, though the restrengthening in shear stress is greater, it occurs over a much smaller amount of slip and thus the extra dissipated energy is relatively small, only 0.02 MJ/m^2. The actual available energy ΔW_0 is nearly 2 times larger than the seismically estimated available energy ΔW_0, which is expected, given that our stress undershoot is approximately half the average stress drop of the event ($\gamma \approx 0.5$ from Equation (4.11)). This leads to G_{SE} underestimating G_A by a factor of 3. There is also a greater disparity between the η = 0.61 and η_A = 0.37 than seen for the previous crack-like events.

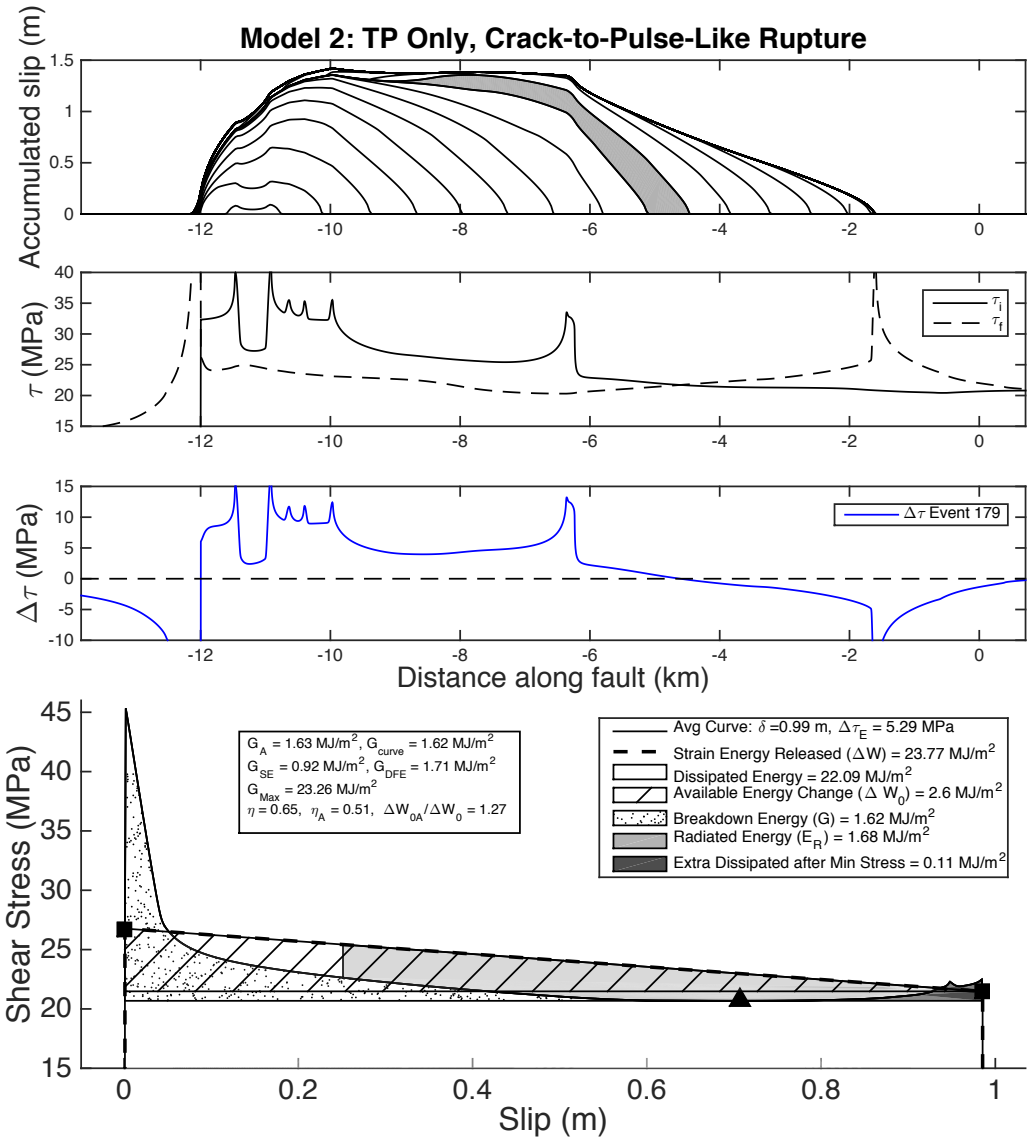

Figure 4.7: Representative event from model 2 showing crack-like behavior that transitions to pulse-like behavior. Row 1) Accumulated slip profile with slip distribution along the fault plotted every 0.5 seconds. Accumulated slip is shaded to emphasize the transition from crack-like to pulse-like behavior. Row 2) Initial and final stress distributions along the fault. Row 3) Stress drop distribution along the fault. Row 4) Average shear stress vs. slip curve with relevant energy quantities labeled. Initial and final stresses are marked with black squares. The minimum level of shear stress is marked with a black triangle and occurs late in the event due to continuous weakening from the thermal pressurization. In this case, the crack-like-to-pulse-like behavior corresponds in a small undershoot, and the actual available energy ΔW_{OA} is now slightly larger than the seismically estimated ΔW_0, with their ratio being 0.9. G_{SE} underestimates G_A by a factor of 2.

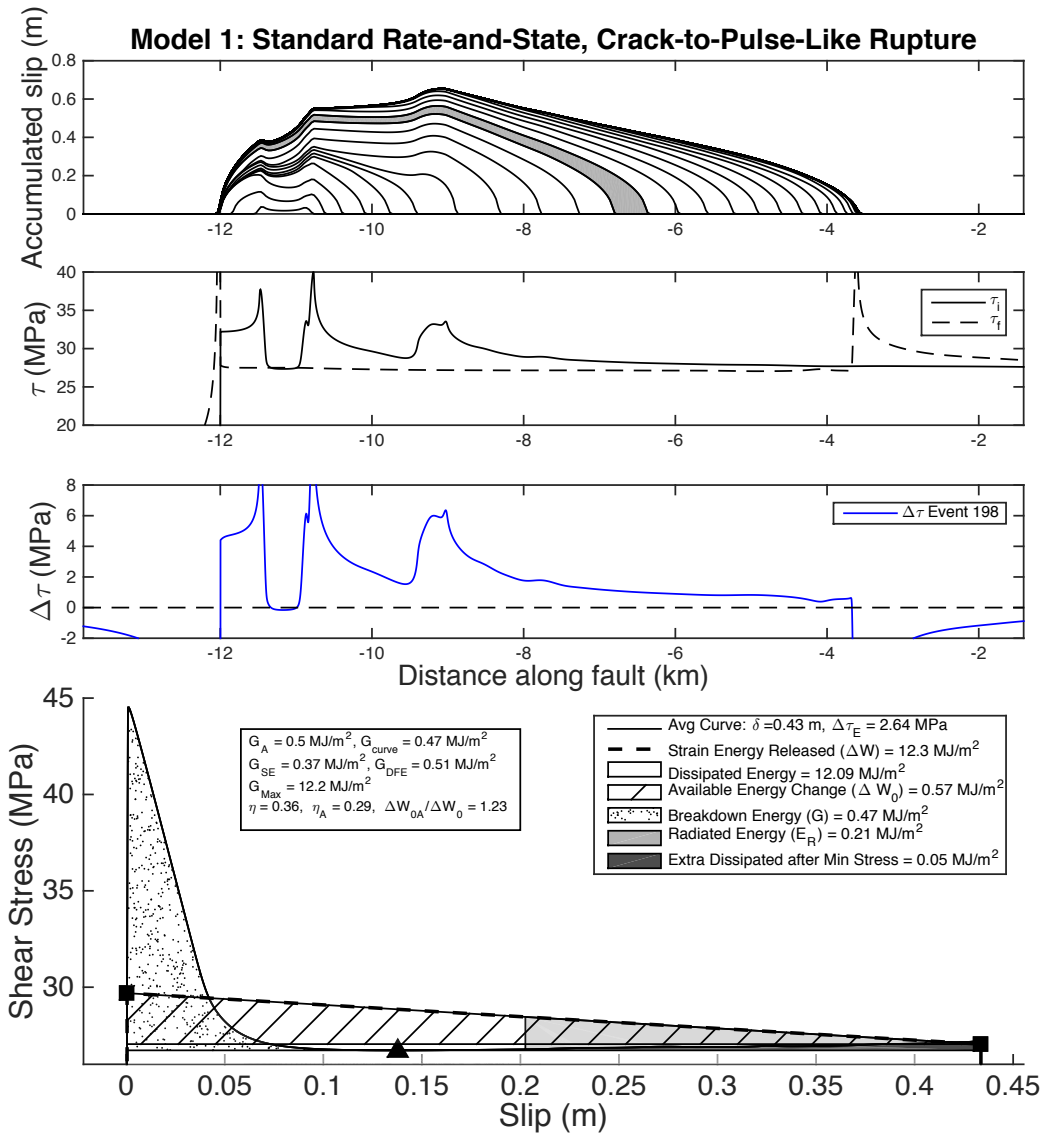

Figure 4.8: Representative event from model 1 showing crack-like-to-pulse-like behavior that begins to restrengthen early on in the event. Row 1) Accumulated slip profile with slip distribution along the fault plotted every 0.5 seconds. Slip shaded to emphasize the transition from crack-like to pulse-like behavior. Row 2) Initial and final stress distributions along the fault. Row 3) Stress drop distribution along the fault. Row 4) Average shear stress vs. slip curve with relevant energy quantities labeled. Initial and final stresses are marked with black squares. The minimum level of shear stress is marked with a black triangle and occurs relatively early in slip. Again, due to a small undershoot, one has $\Delta W_{0A}/\Delta W_0 > 1$. G_{SE} underestimates G_A. Early stress recovery causes a 30 percent discrepancy between G_{DFE} and G_A due to non-negligible dissipation after the minimum dynamic stress level is reached.

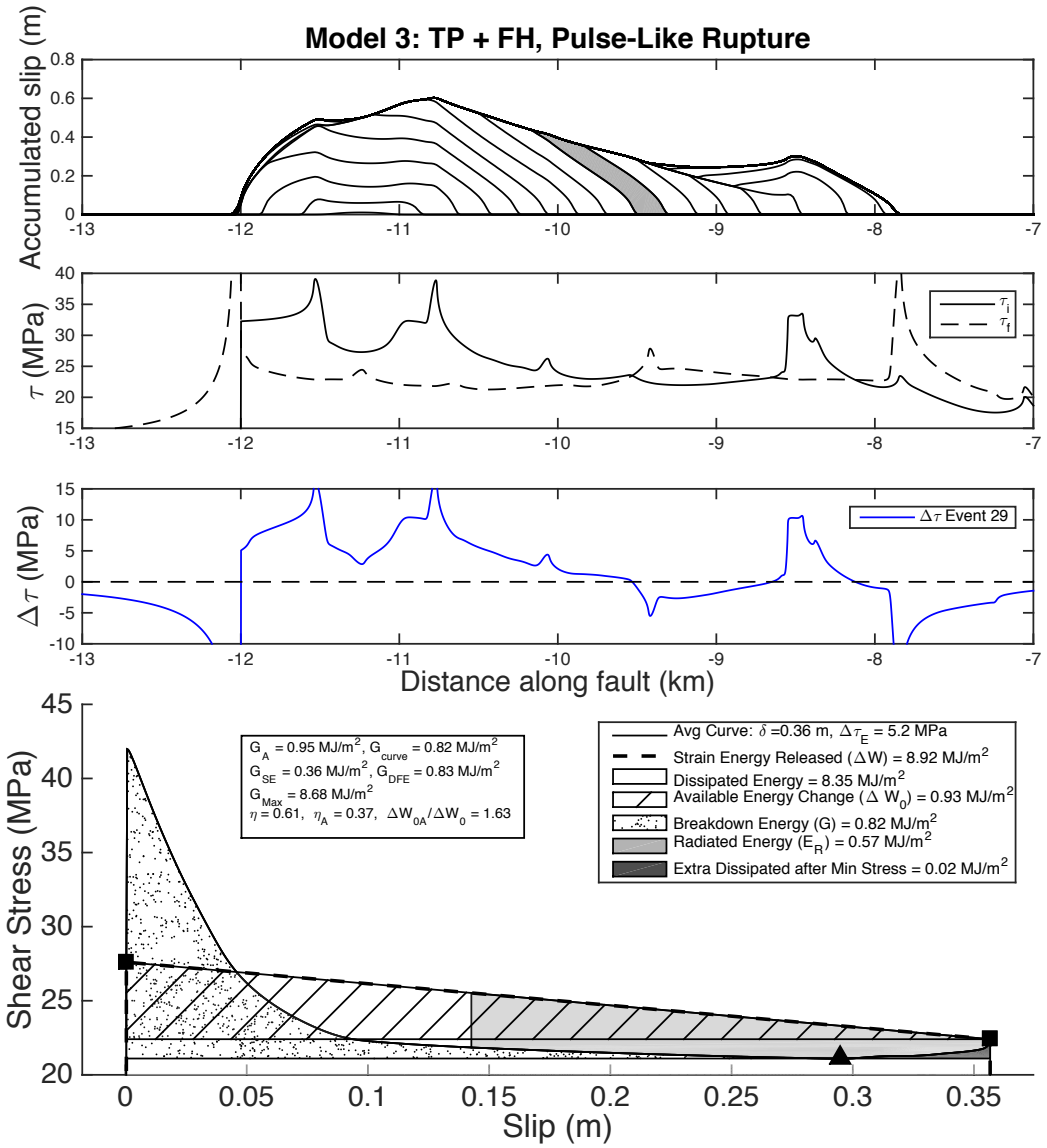

Figure 4.9: Representative event from model 3 showing pulse-like behavior that restrengthens before final slip. Row 1) Accumulated slip profile with slip distribution along the fault plotted every 0.5 seconds. Slip accumulated between the thirteenth and fourteenth timesteps is shaded to emphasize the pulse-like behavior. Row 2) Initial and final stress distributions along the fault. Row 3) Stress drop distribution along the fault. Row 4) Average shear stress vs. slip curve with relevant energy quantities labeled. Initial and final stresses are marked with black squares. The minimum level of shear stress is marked with a black triangle. $\Delta W_{0A}/\Delta W_0 = 1.63$. The undershoot here is slightly larger than in the previous cases, leading to a higher ratio. G_{SE} underestimates G_A by a factor of 3. The early stress recovery is not significant enough to cause a great discrepancy between G_{DFE} and G_A.

4.3.3 Pulse-Like Events

While Models 1 and 2 exhibit events that transition from crack-like to pulse-like behavior, utilizing flash heating in Models 3 and 4 produces events with sharply pulse-like behavior (Figures 4.10). We further extend Model 3 into a 100 km VW region to achieve even sharper pulses (Figure 4.11). The shaded regions of accumulated slip (Row 1) illustrate the dramatic pulse-like behavior of these events. Correspondingly, they have significant restrengthening and a stress undershoot on the order of 5 - 10 MPa in both events, much larger than the average stress drop of ~2 MPa. This results in much larger actual available energy ΔW_{0A} than the seismically estimated ones, by factors of 6 and 9, respectively. The much larger ΔW_{0A} is nearly equally split between G_A and E_R/A, and both of them are significantly larger than ΔW_0. Thus seismically observed radiation ratios η are much greater than 1 (η = 3.22 and 5.57 respectively) while the actual radiation ratios remain reasonable (η_A = 0.53 and 0.61 respectively).

Because E_R/A is larger than ΔW_0, the seismically estimated breakdown energy G_{SE} is now negative as occurs for ~ 20% of events in the study from Abercrombie and Rice, 2005. However, G_A is still a reasonable value on the order of 1-10 MJ/m^2 for these events. G_{DFE} provides a much better estimate of G_A, as we expect, within 25% of the true value.

The event from Model 4 (Figure 4.10) experiences a nearly total dynamic stress drop before recovering to around 8 MPa final shear stress. G_{Max} gives a much better approximation of G_A in this case, here within a factor of 2. However, it still overestimates G_A, even when the assumption of nearly complete strength drop is valid.

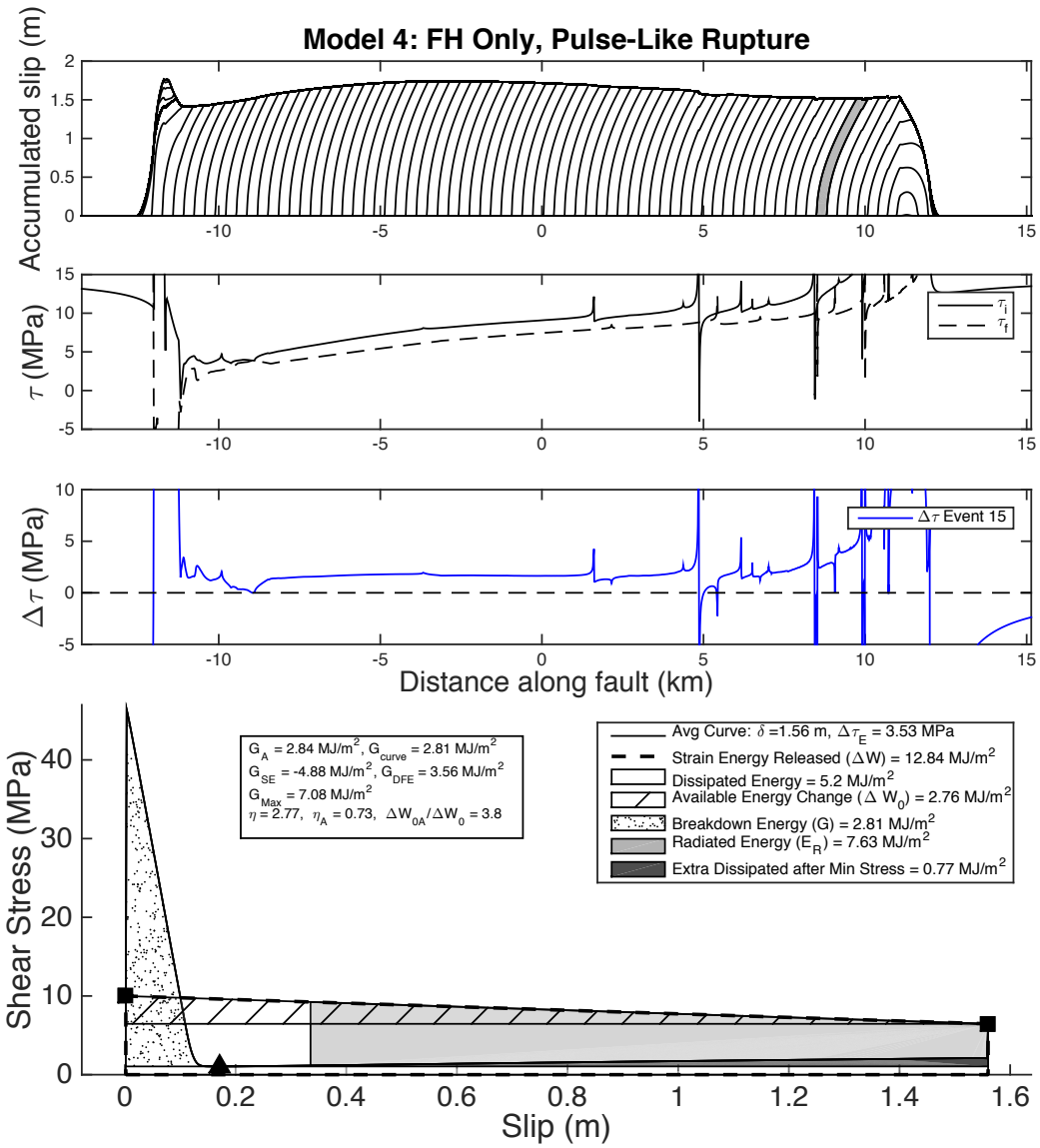

Figure 4.10: Representative event from model 4 showing pulse-like behavior that weakens a dynamic level of shear stress very near to 0. Row 1) Accumulated slip profile with slip distribution along the fault plotted every 0.1 seconds. Slip accumulated during a single time period is shaded to emphasize the pulse-like behavior. Row 2) Initial and final stress distributions along the fault. Row 3) Stress drop distribution along the fault. Row 4) Average shear stress vs. slip curve with relevant energy quantities labeled. Initial and final stresses are marked with black squares. The minimum dynamic level of shear stress (black triangle) gives nearly a complete strength drop. The pulse-like nature of the rupture leads to significant restrengthening and a large stress undershoot at final slip, larger than the average stress drop, leading to $\Delta W_{0A}/\Delta W_0 = 4$. As such, the seismically estimated available underestimates the actual available energy by a factor of 4. Since the radiated energy is larger than the seismically estimated available energy, the seismically estimated G_{SE} gives an unphysical (negative) value.

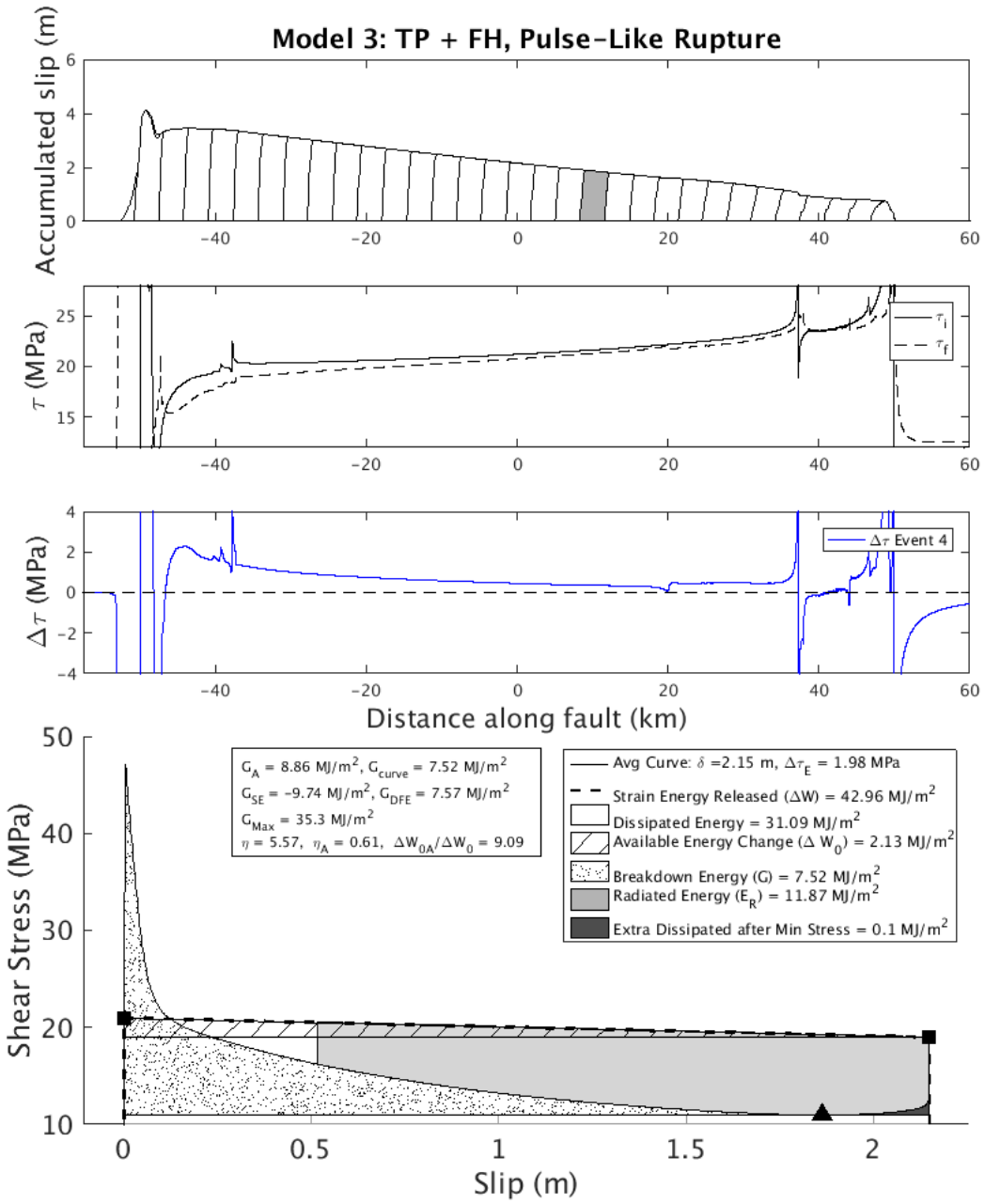

Figure 4.11: Representative event from extended model 3 (100 km VW Region) showing stronger pulse-like behavior. Row 1) Accumulated slip profile with slip distribution along the fault plotted every 1 second. A portion of slip accumulated is shaded to emphasize the pulse-like behavior. Row 2) Initial and final stress distributions along the fault. Row 3) Stress drop distribution along the fault. Row 4) Average shear stress vs. slip curve with relevant energy quantities labeled. Initial and final stresses are marked with black squares. The minimum level of shear stress (black triangle) occurs late in the event due to continuous weakening from the thermal pressurization. The sharp pulse-like nature of the rupture leads to significant restrengthening and a large stress undershoot at final slip, which is several times larger than the average stress drop, leading to $\Delta W_{0A}/\Delta W_0 >> 1$. Again, G_{SE} gives an unphysical (negative) value.

4.3.4 Trends in G, η, and $\Delta W_{0A}/\Delta W_0$

The entire suite of events from each of the 4 models further corroborates our conclusions from the specific sample events shown in the previous section. The sample events illustrated in detail in the previous 3 sections are shown in gold stars amongst the rest of the events from each sequence.

The trends of the breakdown energy with the event average slip in Models 1-3 are as expected based on Chapters 2-3 (Figures 4.12 - 4.16). Model 1, with the standard rate-and-state formulation, shows a saturation of G_A with slip with the increasing event size. Both Models 2 and 3 include thermal pressurization and show a significant increase in the breakdown energy with the event size. There are significantly more events that have somewhat of a pulse-like nature in Model 3 and this leads to some much lower G_{SE} values in that model. Model 4 with strong flash heating produces sharp pulses without much complexity in terms of the event sizes. Similar to the models with the standard rate-and-state formulation, G does not increase much with the increasing event size in Model 4, since the peak stress and the effective slip weakening distance vary relatively insignificantly with the event dynamics. The different trends are more obvious when viewed side-by-side (Figure 4.16).

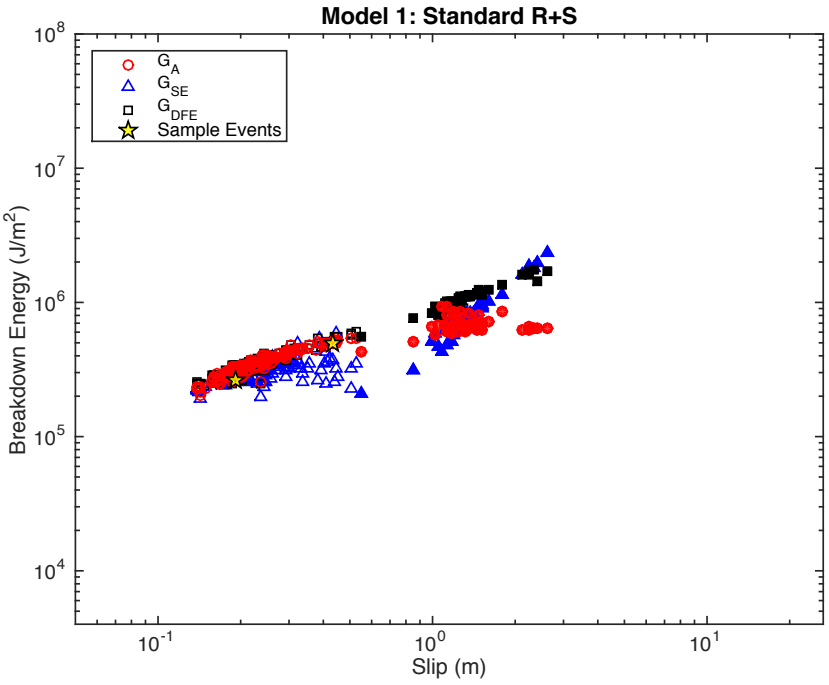

Figure 4.12: Breakdown energies G_A, G_{SE}, and G_{DFE} for all events in Model 1. Sample events shown in previous figures are given by gold stars.

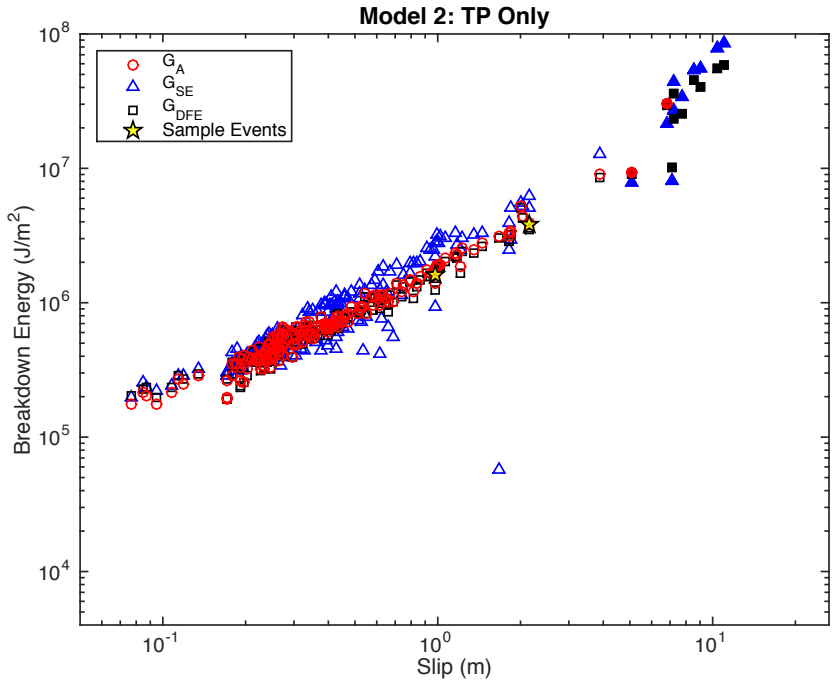

Figure 4.13: Breakdown energies G_A, G_{SE}, and G_{DFE} for all events in Model 2. Complete rupture events are indicated by filled markers. Sample events shown in previous figures are given by gold stars.

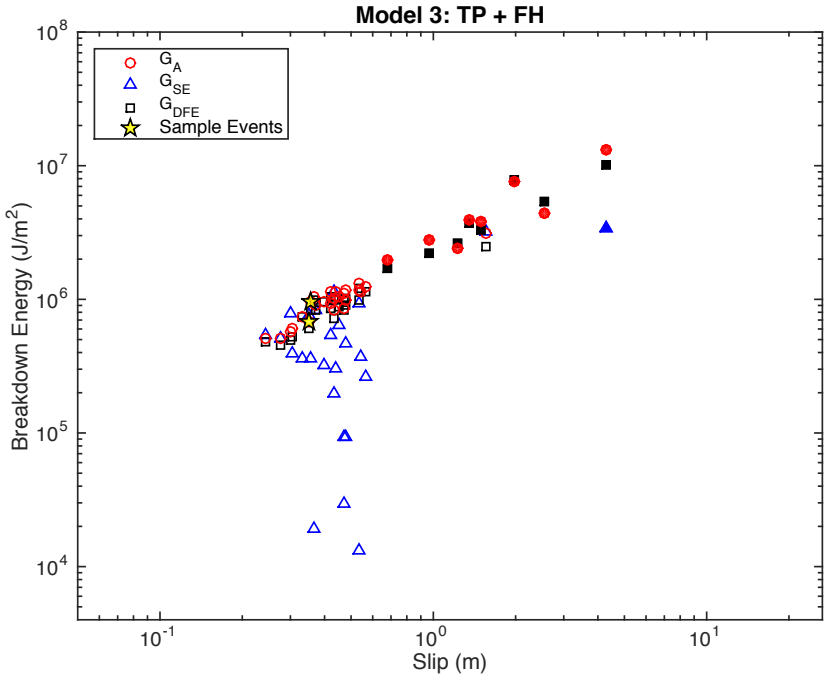

Figure 4.14: Breakdown energies G_A, G_{SE}, and G_{DFE} for all events in Model 3. Complete rupture events are indicated by filled markers. Sample events shown in previous figures are given by gold stars.

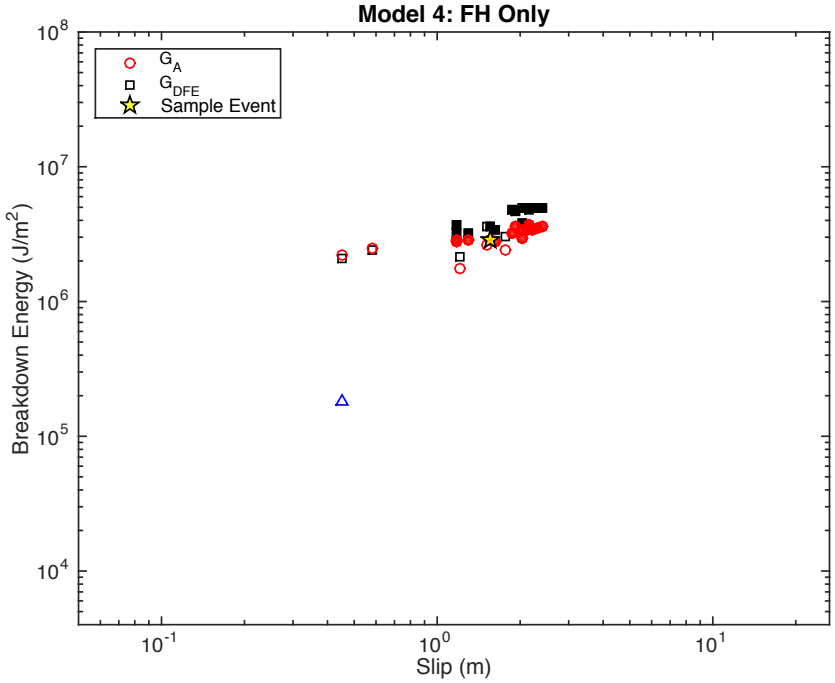

Figure 4.15: Breakdown energies G_A, G_{SE}, and G_{DFE} for all events in Model 4. Complete rupture events are indicated by filled markers. Sample events shown in previous figures are given by gold stars. Nearly all G_{SE} values are negative and thus the only positive value is shown.

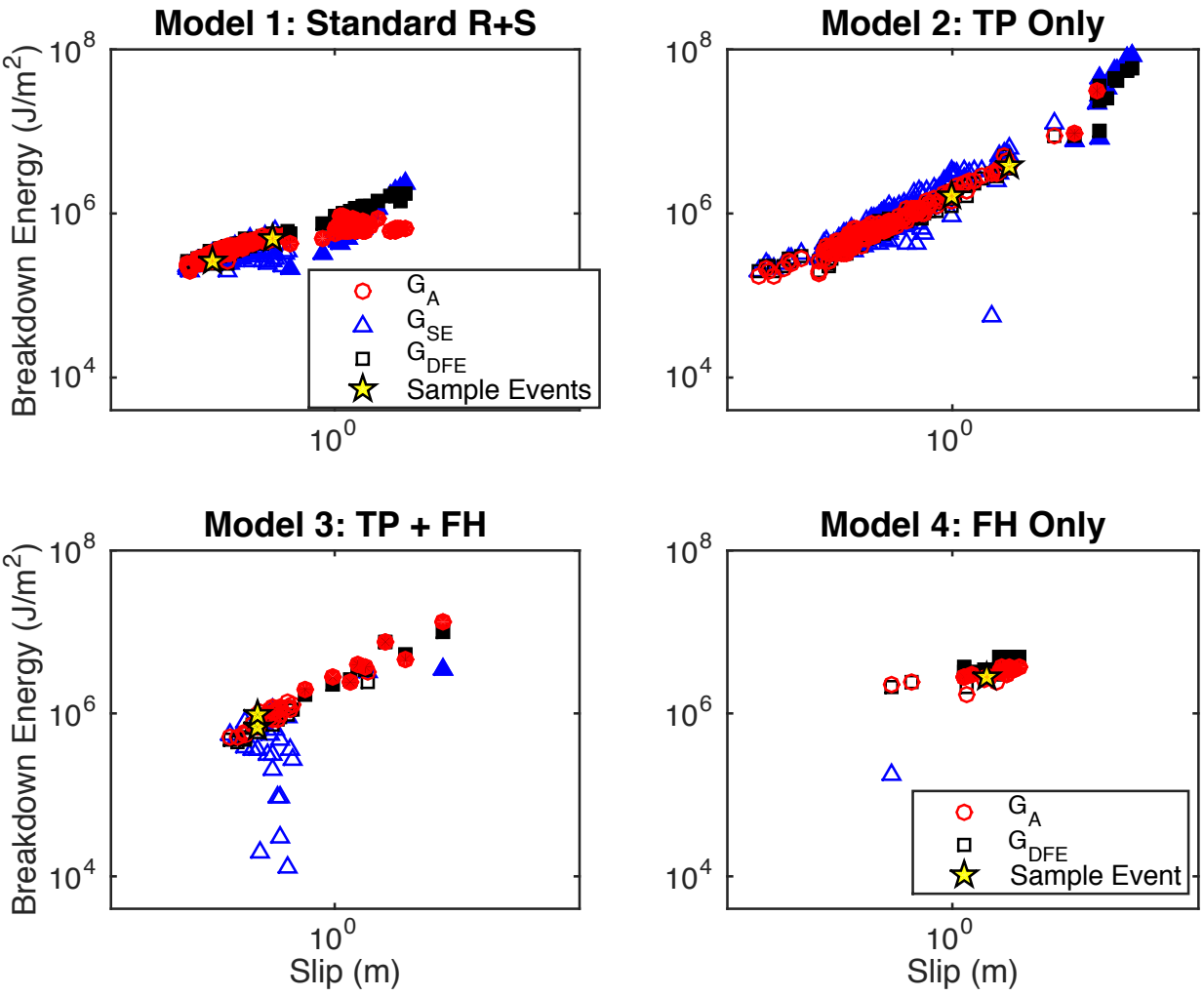

Figure 4.16: Breakdown energies G_A, G_{SE}, and G_{DFE} for all events in each of the 4 models; the different trend for each model is evident. Complete rupture events are indicated by filled markers. Sample events shown in previous figures are given by gold stars. All G_{SE} values for model 4 are negative and thus not shown.

How well the seismically estimated available energy ΔW_0 approximates the actual available energy ΔW_{0A} depends on the mode of the rupture (Figures 4.17-4.21). For crack-like-ruptures, broad pulse-like ruptures, and transitional rupture modes, they are within a factor of 2 and often closer. Crack-like ruptures tend to produce a relatively small overshoot, in which case ΔW_0 overestimates ΔW_{0A} but not much more than 20% or so. More complex ruptures may experience restrengthening towards the end of slip and then a small overshoot or undershoot, resulting in the discrepancy closer to 100%. As ruptures become more pulse-like (Models 3

and 4), their undershoot increases and the actual available energy ΔW_{0A} becomes increasingly larger than the seismically estimated one by a factor of up to 15 in some of the simulated events. This much larger available energy typically corresponds to both breakdown energy and radiated energy that each individually are also larger than the available energy, leading to negative values of the seismically estimated G_{SE} and values of the seismically estimated radiation efficiency η larger than 1.

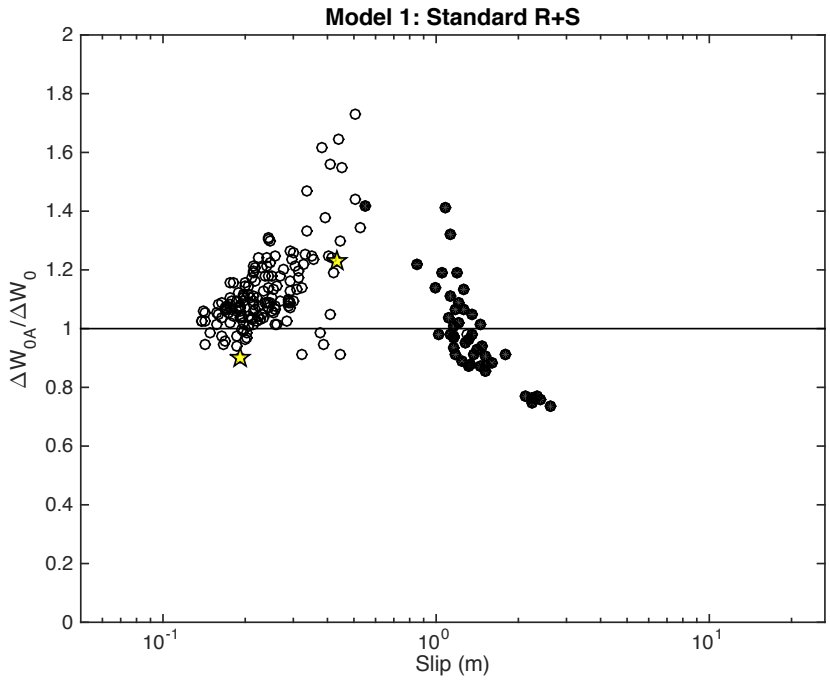

Figure 4.17: Ratio of actual available energy ΔW_{0A} to seismically estimated available energy ΔW_0 vs. average slip for all events in Model 1. Sample events shown in previous figures are given by gold stars.

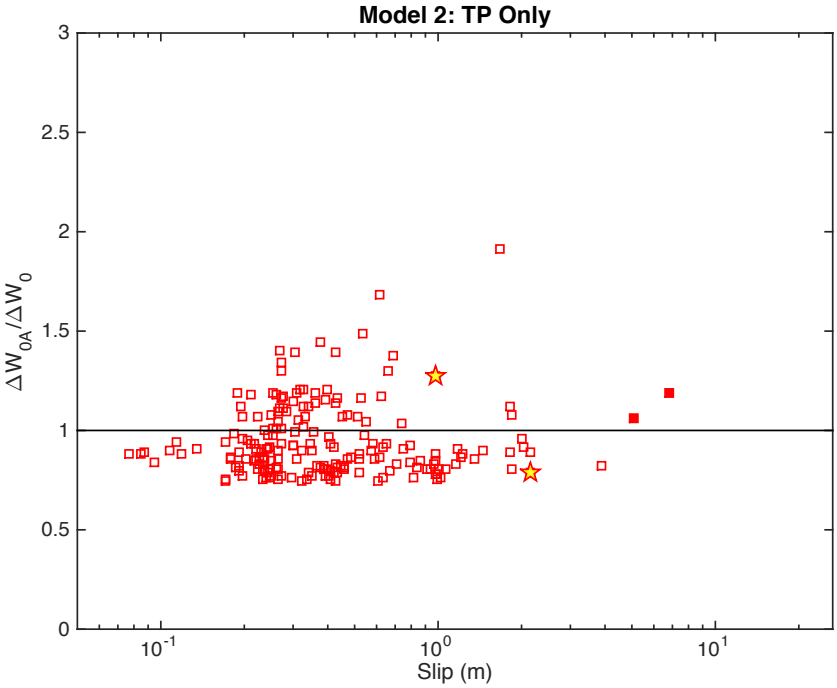

Figure 4.18: Ratio of actual available energy ΔW_{0A} to seismically estimated available energy ΔW_0 vs. average slip for all events in Model 2.

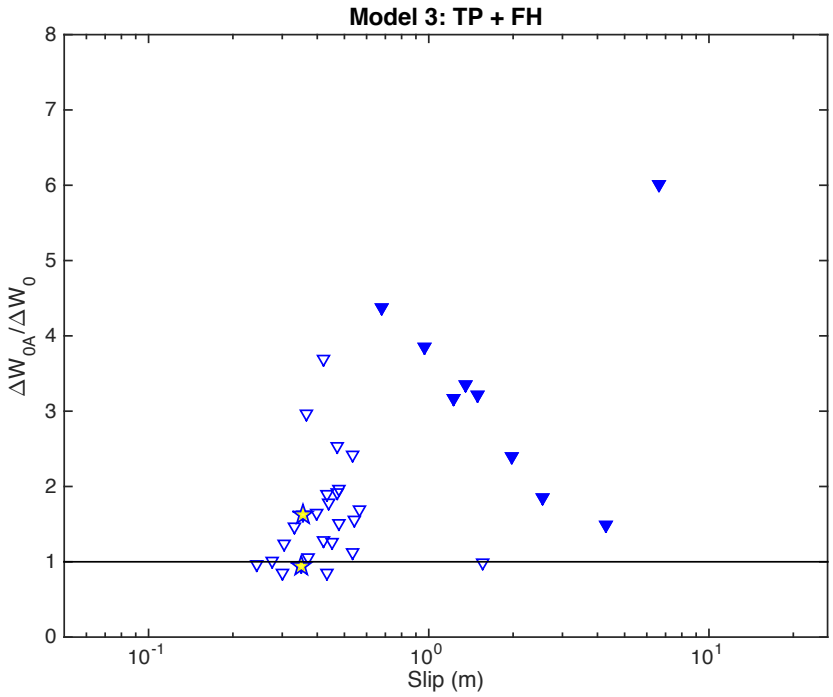

Figure 4.19: Ratio of actual available energy ΔW_{0A} to seismically estimated available energy ΔW_0 vs. average slip for all events in Model 3. Sample events shown in previous figures are given by gold stars.

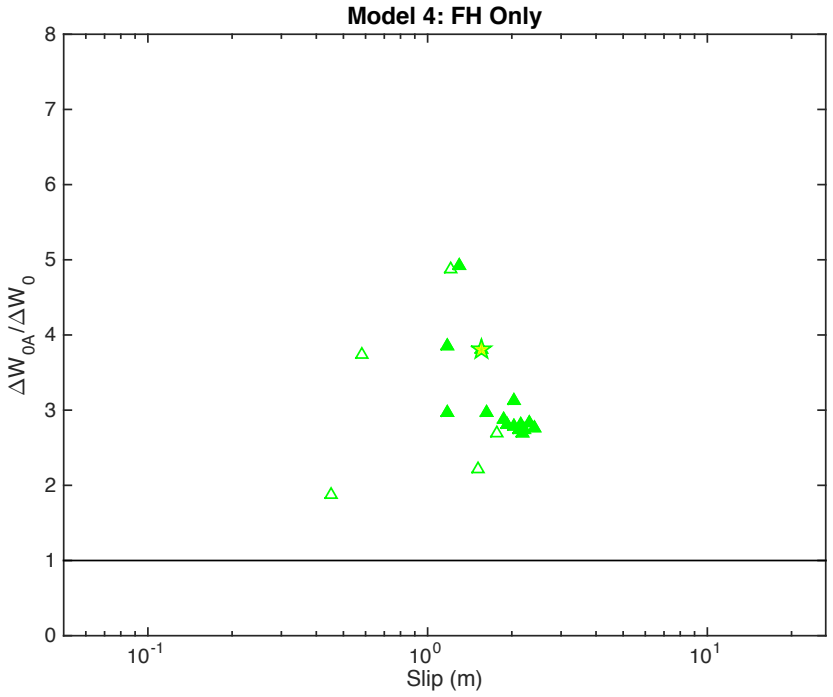

Figure 4.20: Ratio of actual available energy ΔW_{0A} to seismically estimated available energy ΔW_0 vs. average slip for all events in Model 4.

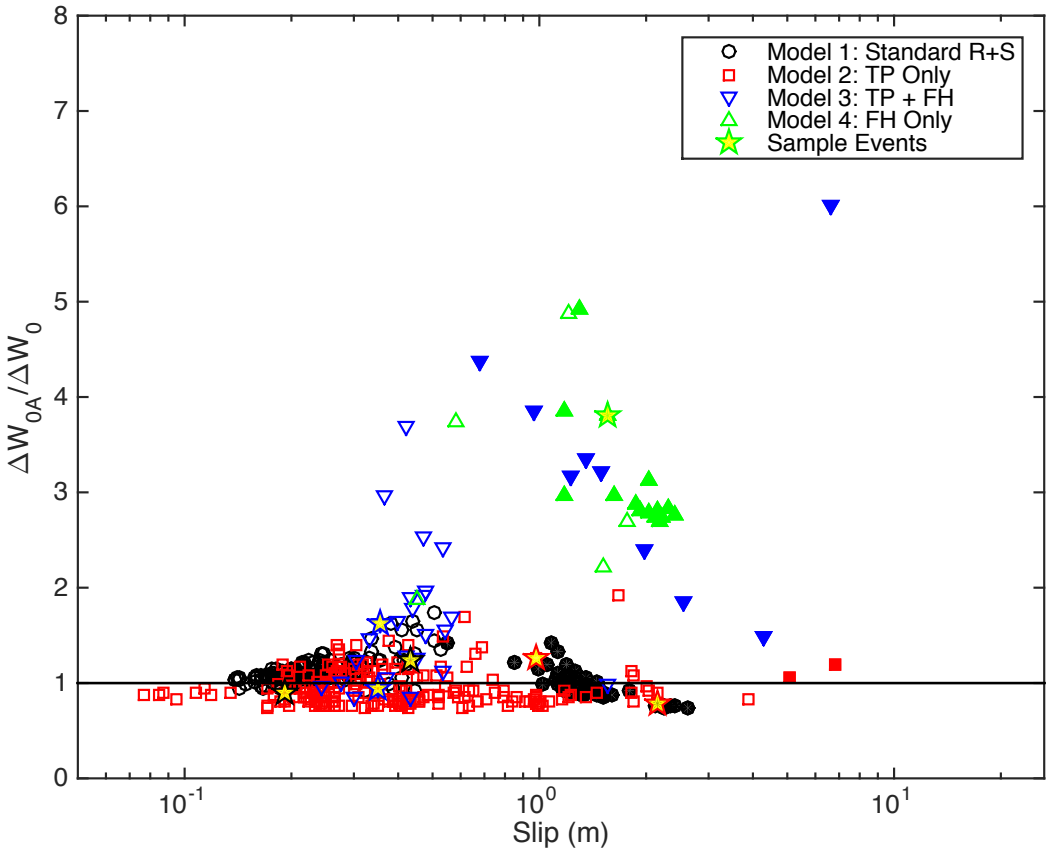

Figure 4.21: Ratio of actual available energy ΔW_{0A} to seismically estimated available energy ΔW_0 vs. average slip for all events in each of the four models. Values greater than 1 (solid black line) signify that the seismically estimated available energy is underestimating the actual available energy, due to stress undershoot during the event which can be quite significant for sharp pulses. Values smaller than 1 indicate overestimates of the available energy due to stress overshoot; since the stress overshoot tends to be small in comparison with stress drop, the values are only slightly different from 1, indicating good estimates for crack-like ruptures.

The ratios G_{SE}/G_A and G_{DFE}/G_A (Figure 4.22-4.25) show the relation of the two estimates of the actual breakdown energy G_A. Models 1 and 2 produce many events that are clearly crack like and Model 3 produces some. These events tend to have a slight overshoot and their seismically estimated G_{SE} overestimates G_A, but not by much, and certainly within a factor of 2. These models also produce some broad pulse-like and transitional events, and those often have a slight undershoot, with G_{SE} then underestimating G_A, again within a factor of 2. Adding flash heating (Model 3) leads to more pulse-like behavior in events, and thus G_{SE} shows a greater discrepancy with G_A (Figure 4.24). Some of the largest events in this model event even result

in a negative estimate of G_{SE} (which means that the radiated energy exceeds the seismically estimated available energy). Model 4 produces sharp pulses, most of which show nearly complete dynamic stress drop during the event (Figure 4.25). The disparity between G_A and G_{SE} is the largest in Model 4 among all models; all events in this simulation produce negative G_{SE} values. In all 4 models, G_{DFE} estimates G_A better than G_{SE} (Figure 4.26), as expected; however, as already noted, G_{DFE} requires knowing the difference between the final and dynamic levels of stress, e.g., the amount of overshoot or undershoot, which are currently not accessible observationally.

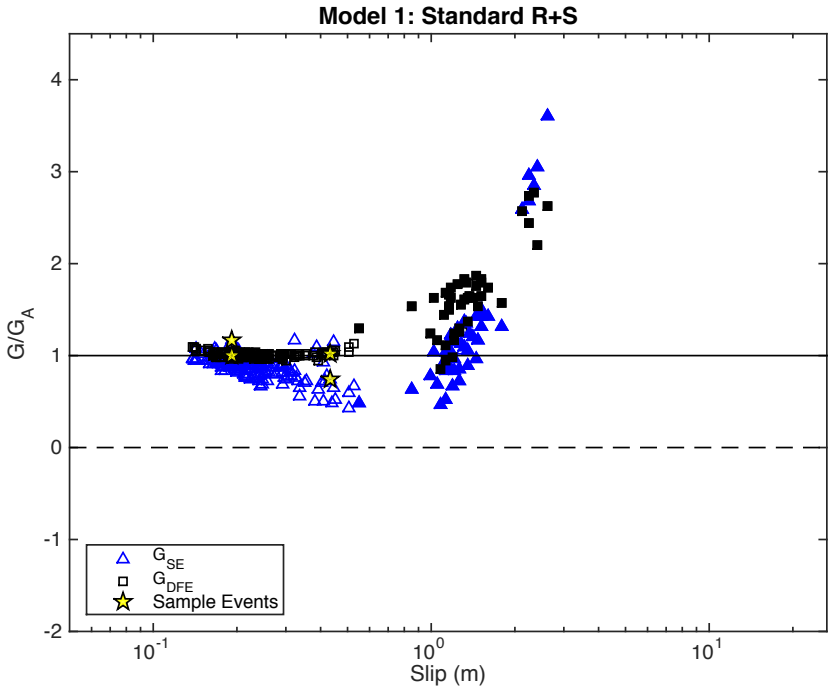

Figure 4.22: Ratios of G_{SE} to G_A and G_{DFE} to G_A vs. average slip for all events in model 1. Sample events shown in previous figures are given by gold stars. Values near 1 (solid black line) signify good agreement between the two methods.

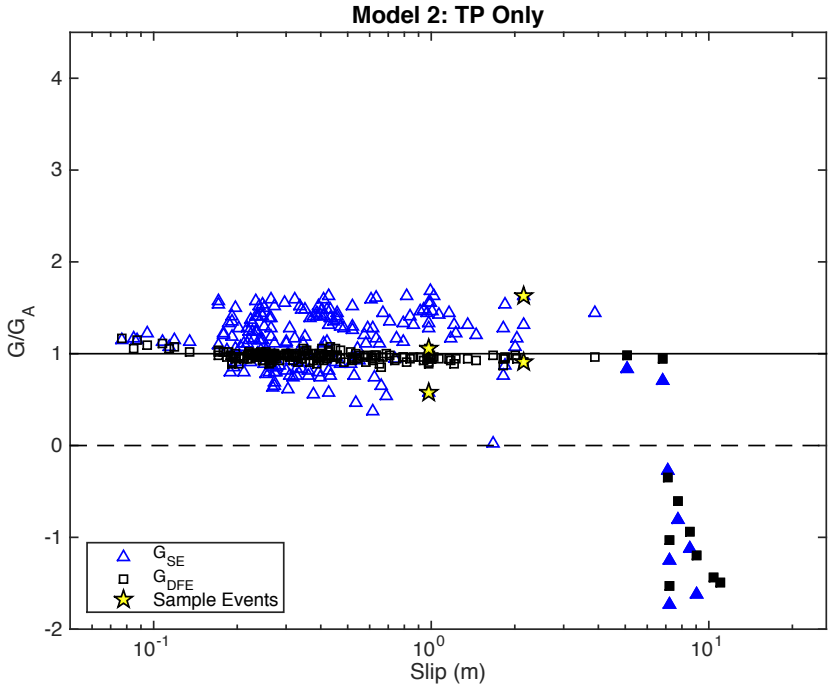

Figure 4.23: Ratios of G_{SE} to G_A and G_{DFE} to G_A vs. average slip for all events in model 2. Values above 1 (solid black line) are indicative of crack-like events with non-negligible overshoot. Negative values correspond to seismically estimated breakdown energies for the pulse-like ruptures that have higher actual radiated energy than the seismically estimated available energy.

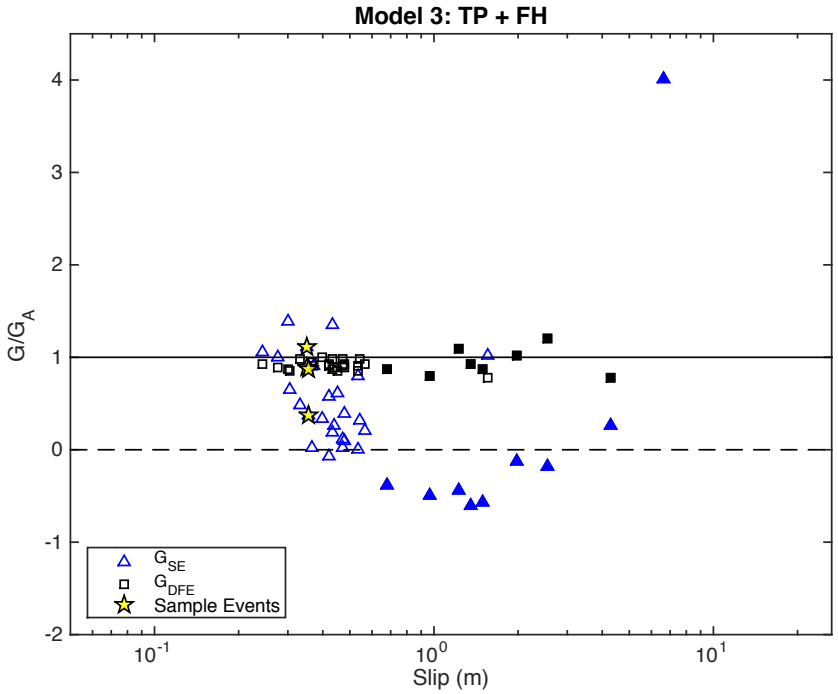

Figure 4.24: Ratios of G_{SE} to G_A and G_{DFE} to G_A vs. average slip for all events in model 3. Sample events shown in previous figures are given by gold stars. Values near 1 (solid black line) signify good agreement between the two methods. Negative values (below dotted line) are from negative G_{SE} due to stress undershoot in pulse-like events.

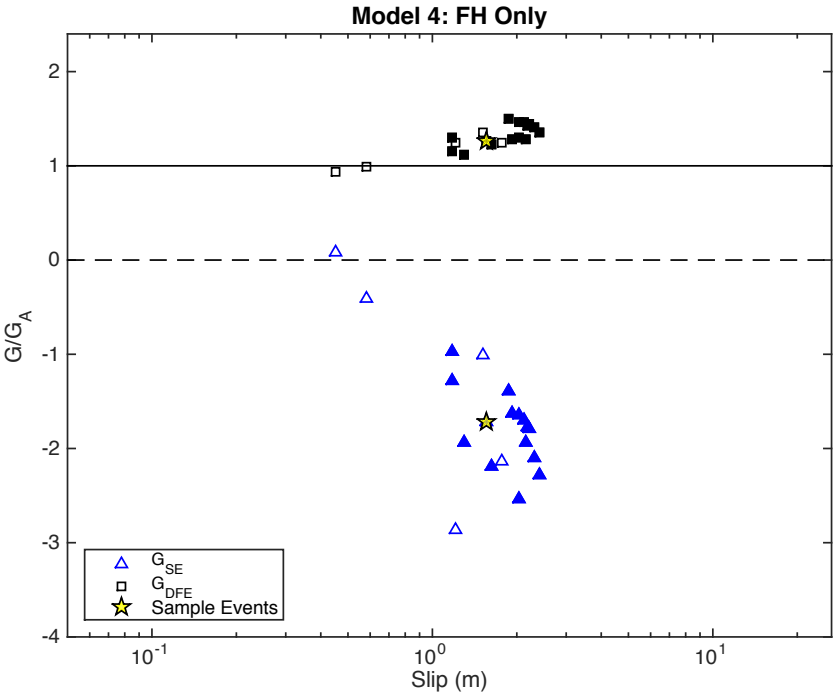

Figure 4.25: Ratios of G_{SE} to G_A and G_{DFE} to G_A vs. average slip for all events in model 4.

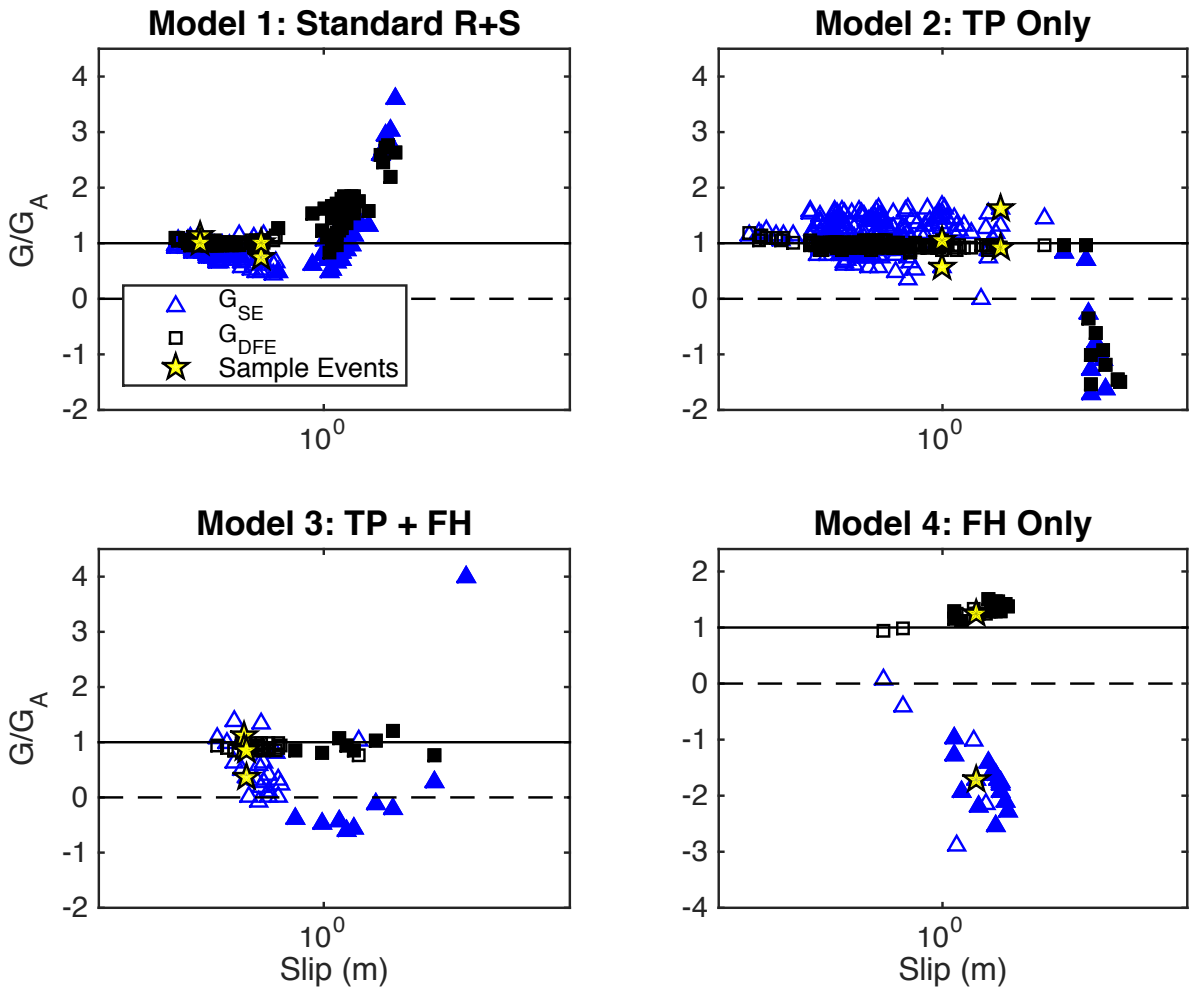

Figure 4.26: G_{SE}/G_A and G_{DFE}/G_A vs. average slip for all events in each of the 4 models. Values near 1 (solid black line) signify that the method agrees well with the true breakdown energy G_A. Values larger than 1 are indicative of crack-like events and values near and below 0 are indicative of pulse-like events. Note that the vertical axis for model 4 has been extended to show the greater range of negative ratios for that model.

Radiation ratios for all events in Models 1-4 confirm the same trends (Figures 4.27-4.31). The actual radiation ratios $\eta_A < 1$, by definition, and tend to increase with the event size in the same simulation. The trend is especially strong in Model 1, in which the breakdown energy is relatively constant and independent of the event size, resulting in the systematic increase of the radiation ratio approaching 1. As events become more pulse-like, their seismically estimated radiation ratios both tend to increase and to deviate more from the actual ratios, mirroring the trends in the actual and seismically estimated available energies already discussed. Many events

in Models 3 and 4 have seismically estimated radiation ratios that are greater than 1.

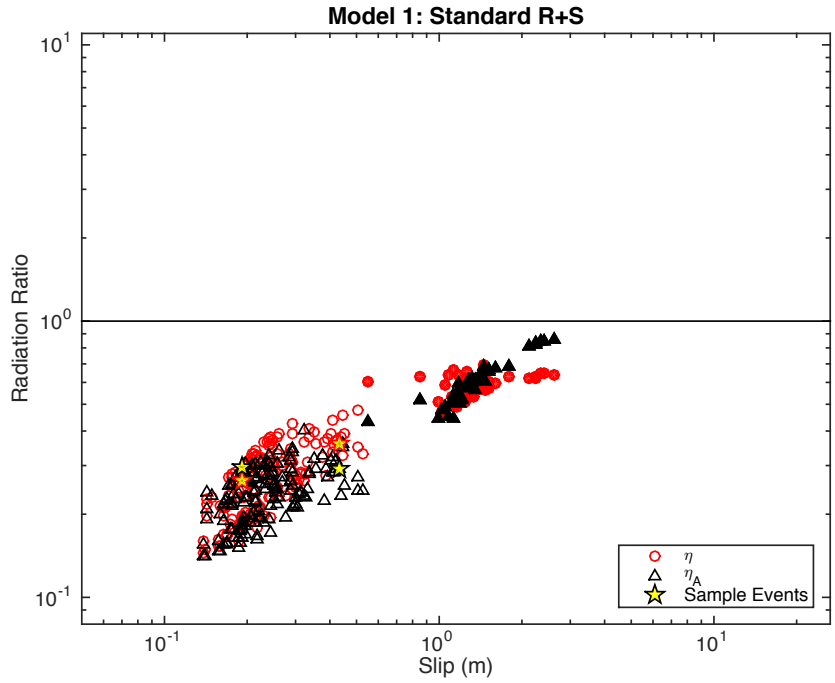

Figure 4.27: Seismically estimated radiation ratios (η) and actual radiation ratios η_A vs. average slip for all events Model 1. Values of η greater than 1 (solid black line) signify that the radiated energy E_R exceeded the available energy ΔW_0 for these events. $0 \leq \eta_A \leq 1$ by definition.

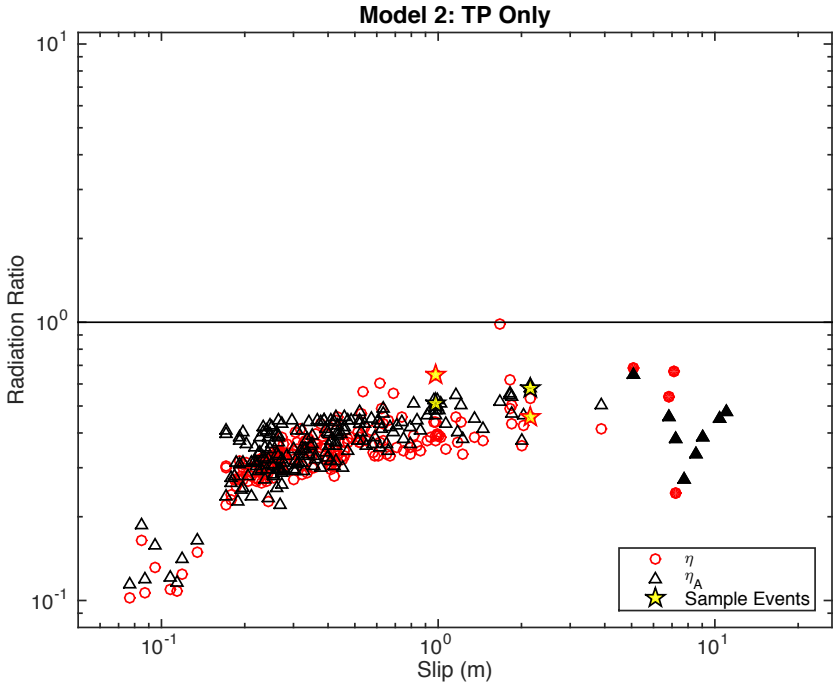

Figure 4.28: Seismically estimated radiation ratios (η) and actual radiation ratios η_A vs. average slip for all events Model 2.

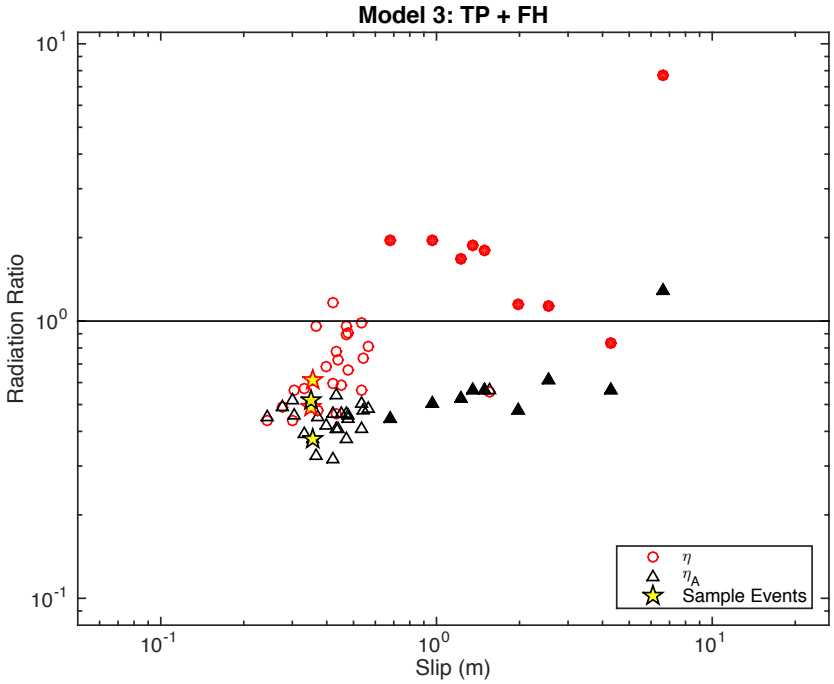

Figure 4.29: Seismically estimated radiation ratios (η) and actual radiation ratios η_A vs. average slip for all events Model 3. Values of η greater than 1 (solid black line) signify that the radiated energy E_R exceeded the available energy ΔW_0 for these events. $0 \leq \eta_A \leq 1$ by definition.

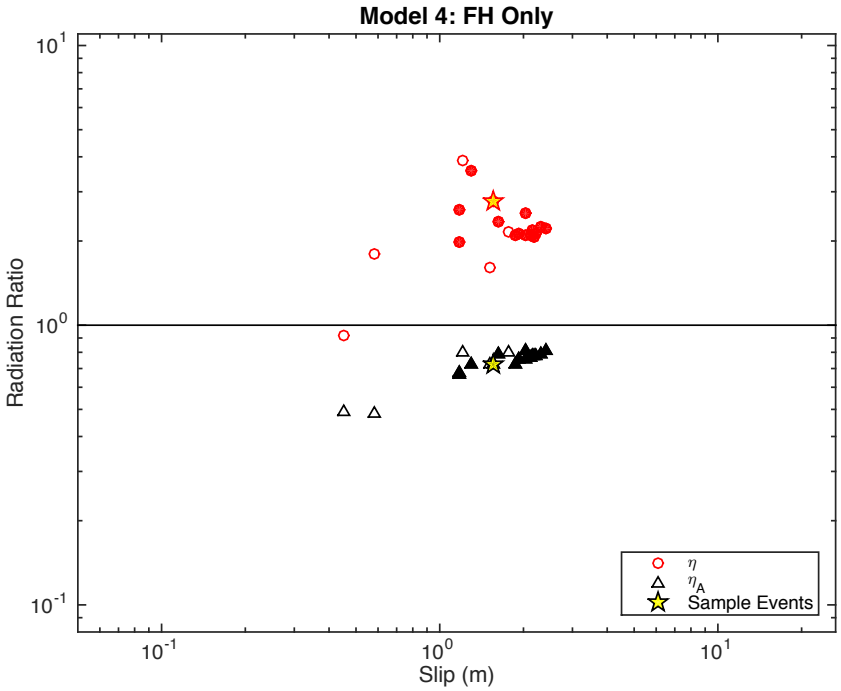

Figure 4.30: Seismically estimated radiation ratios (η) and actual radiation ratios η_A vs. average slip for all events Model 4.

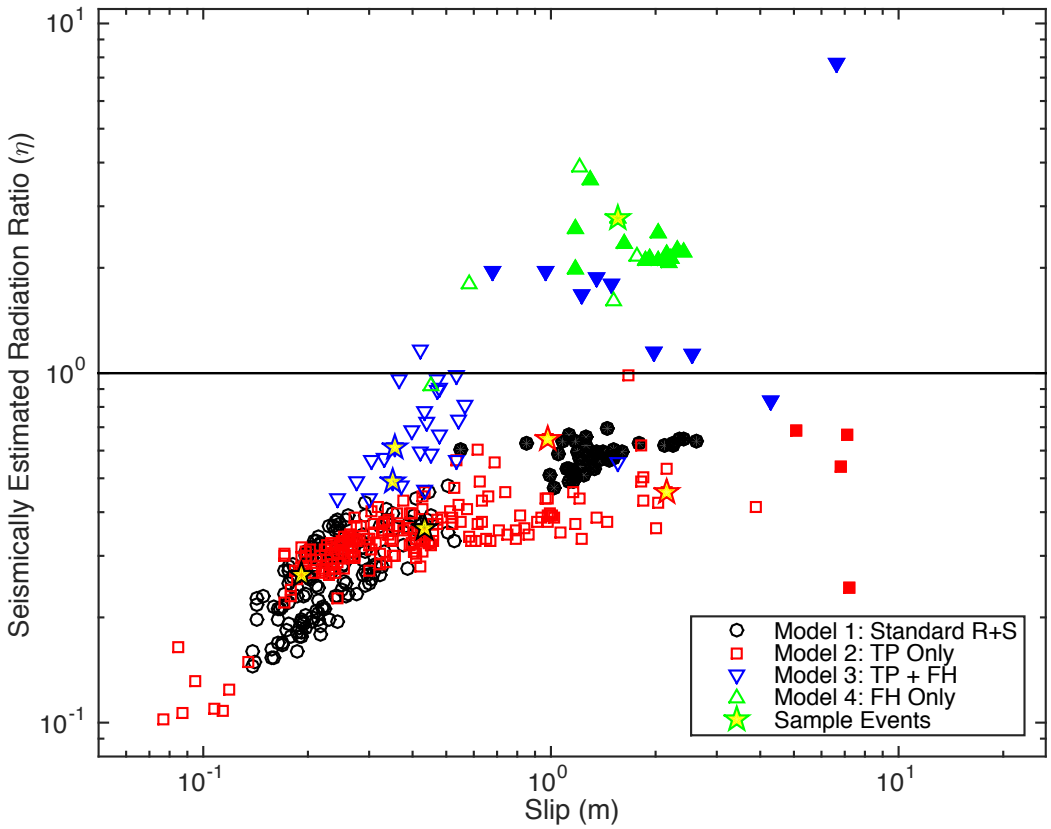

Figure 4.31: Seismically estimated radiation ratios (η) vs. average slip for all events in each of the 4 models. Values greater than 1 (solid black line) signify that the radiated energy E_R exceeded the available energy ΔW_0 for these events, indicating a more pulse-like rupture. All of the events for Model 4 have seismically estimated radiation ratios exceeding 1.

G_{max} should not be a good estimate for the events on Models 1-3, since their dynamic level is relatively far from zero, and our results confirm that (Figure 4.32). If events experience a nearly complete stress drop dynamically, as is the case for events in Model 4, G_{Max} does a better job of estimating G_A. Even for these events, the estimate is often too high by a factor of 2 or more.

Our average curves conserve both the total strain energy release ΔW and dissipated energy E_D. However, breakdown energy G is not necessarily conserved as can be seen in Figure 4.33. Ratios of G_{curve} to G_A cluster around 1 for all 4 models, meaning G_{curve} is a good estimate for G_A for any type of rupture behavior. The largest discrepancy is about a factor of 2 and there is a slight trend for greater disparity in larger events. This could be due to the fact that larger events tend

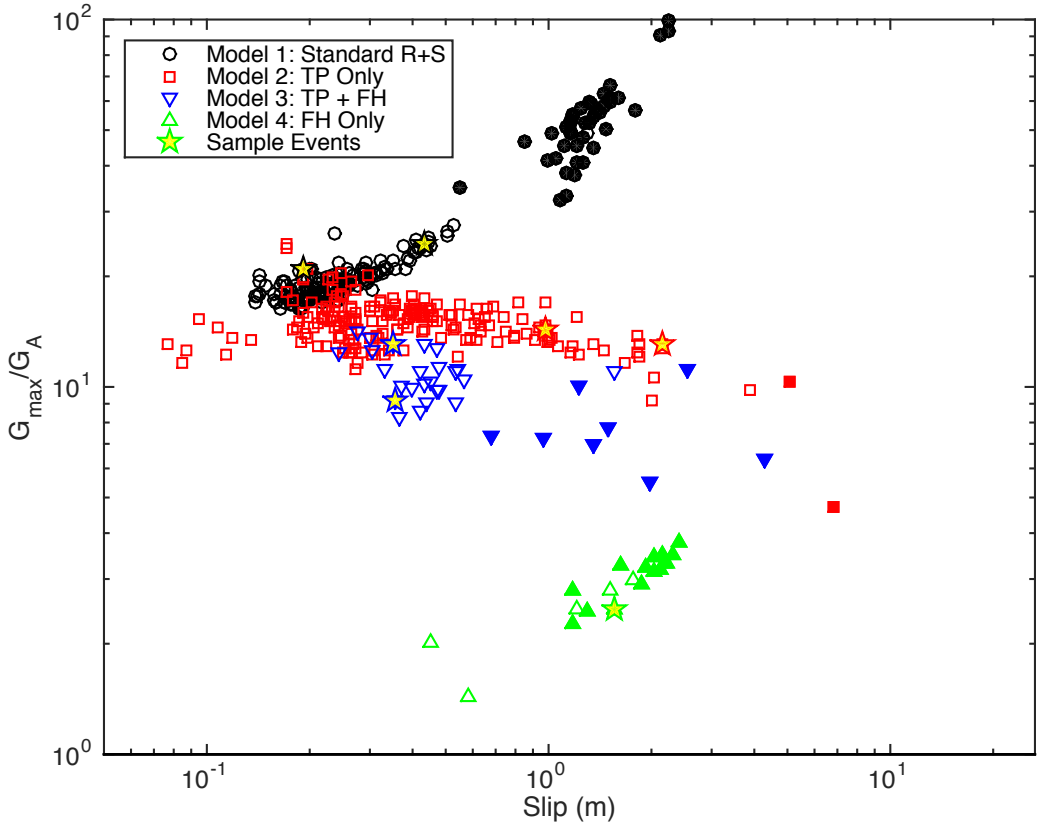

Figure 4.32: G_{max}/G_A for all events in each of the 4 models. Values close to 1 signify that G_{max} is a good approximation of G_A. G_{max} exceeds G_A for all events produced. Events with lower minimum dynamic stress levels produce better agreement, and the best agreement for events from Model 4. However, for the other models G_{max} significantly overestimates the breakdown energy, as expected.

to have more points from the velocity-strengthening portions of the fault model contributing to the average curve, which perhaps affects its shape, making is less representative of the "typical" behavior of the breakdown energy. Thus, G_{curve} is not an accurate representation of G_A but provides a good illustration for it, within a factor of 2, on the average curves.

4.4 Conclusions

To summarize, for crack-like and broad pulse-like ruptures in our models, seismically estimated ΔW_0, G_{SE}, and η provide a reasonable estimate for the actual available energy, breakdown energy, and radiation ratio, $\Delta W_0 A$, G_A, and η_A, respectively, generally within a factor of 2. Radiation ratios for crack-like events all fall within the expected range from 0-1. This is because such models result in either much

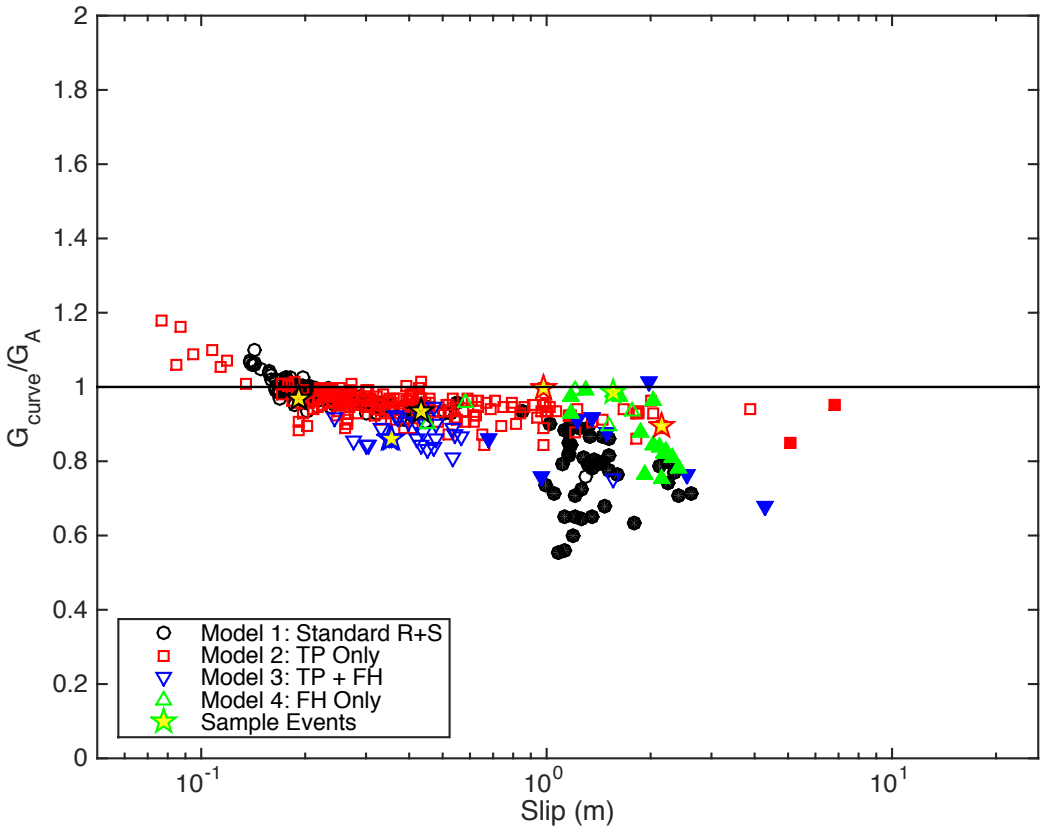

Figure 4.33: G_{curve}/G_A vs. slip for all events in each of the 4 models. G_{curve} is a good approximation to G_A (nearly always within a factor of 2), but the two values are rarely equal.

smaller overshoot or undershoot than the stress drop, and hence remain close to the idealized behavior based on which the seismically estimated quantities are expressed in terms of observable parameters. One exception may be extreme crack-like events, which can potentially achieve much larger overshoot, in which case the available energy would be significantly overestimated, and hence the radiation ratio would be significantly underestimated. Our models did not include such a case but that does not mean that this is physically impossible.

As events become more pulse-like, the stress undershoot, i.e. the difference between the minimum dynamic and final stress, increases. The significant undershoot found in many of our pulses leads to a significant underestimation of the available energy. The difference between actual available energy ΔW_{0A} and seismically estimated available energy ΔW_0 can be an order of magnitude for the sharpest pulses. A large difference between ΔW_{0A} and ΔW_0 means that either breakdown energy G, or

radiated energy E_R, or both are significantly larger than the seismically estimated available energy ΔW_0, leading, in most cases, to negative G_{SE} and seismically estimated radiation ratios larger than 1.

The work of Viesca and Garagash, 2015 utilized the seismically estimated values of the radiation energy, average slip, and stress drop from previous studies for natural events, and hence most events in their catalog produce radiation ratios < 1, as common for observations. At the same time, they envision that the largest natural events are pulse-like ruptures with significant undershoot, and hence much larger available energy than the seismically estimated one. The significant extra available energy from the largest events is then all put into the breakdown energy, resulting in the estimates of the breakdown energies that are (1) much larger than those of Abercrombie and Rice (2005) and (2) much larger than the radiated energy, with the actual radiation ratio being around 0.1 or less. In contrast, in our simulated pulse-like events that have $\Delta W_{0A}/\Delta W_0 >> 1$, the breakdown energy G and radiated energy E_R/A are comparable, resulting in the actual radiation ratios between 0.5 and 1 (and seismically estimated radiation ratios $\eta > 1$.) It remains to be seen whether large and sharp pulse-like ruptures can be produced such that the breakdown energy G is much larger than radiated energy E_R, corresponding to a small actual radiation ratio, as effectively assumed in the work of Viesca and Garagash, 2015. Such events would need to have a combination of larger stress excess $(\bar{\tau}_p - \bar{\tau}_i)$ and more gradual weakening in order to substantially increase G.

There is no simple way to calculate G reliably for pulse-like ruptures using current seismic observations. G_{SE} underestimates G and can even be negative. G_{DFE} can estimate the breakdown energy accurately, but it requires knowing the amount of the overshoot, e.g., the difference between the final and the dynamic levels of stress on the fault, and this currently cannot be measured for natural events. G_{max} used in Viesca and Garagash, 2015 suffers from the same issue, the need to know the absolute stresses on the faults; in addition, its assumption of zero dynamic shear resistance may not be universally applicable.

The idealized model of the earthquake energy budget is often used to analyze observed natural events, and values for G_{SE} and η are normally, but not always, positive and smaller than 1, respectively. Ambercrombie and Rice (2005) removed events with negative G_{SE} from their analysis and specify that 14 out of their 89 total events fall into this category. Perhaps these events are more pulse-like than the others in their catalog. Similarly, Venkataraman and Kanamori, 2004 reported

radiation ratios larger than 1 for some of their events.

The relative rarity of negative G_{SE} and η greater than 1 suggests one of the three possibilities: (i) the large sharp pulse-like ruptures are relatively rare; (ii) these pulse-like ruptures have much larger breakdown energy than radiated energy, with actual radiation ratios of 0.1 or less, as effectively assumed in Viesca and Garagash; or (iii) the seismic estimates are inaccurate, e.g., the radiation energy is significantly underestimated. Exploring the validity of the estimates of the radiation energy using our models and commonly applied seismological techniques is another direction for future work.

References

Abercrombie, Rachel E. and James R. Rice (2005). "Can observations of earthquake scaling constrain slip weakening?" In: *Geophysical Journal International* 162, pp. 406–424. DOI: 10.1111/j.1365-246X.2005.02579.x.

Kanamori, Hiroo and Thomas H. Heaton (2000). "Microscopic and macroscopic physics of earthquakes". In: *Geocomplexity and the Physics of Earthquakes*, pp. 147–163.

Kanamori, Hiroo and Luis Rivera (2006). "Energy Partitioning during an earthquake". In: *Earthquakes: Radiated energy and the physics of faulting*, pp. 3–13.

McGarr, Arthur (1999). "On relating apparent stress to the stress causing earthquake fault slip". In: *Journal of Geophysical Research: Solid Earth* 104.B2, pp. 3003–3011.

Noda, Hiroyuki (2008). "Frictional constitutive law at intermediate slip rates accounting for flash heating and thermally activated slip process". In: *Journal of Geophysical Research: Solid Earth* 113.B9.

Noda, Hiroyuki and Nadia Lapusta (2010). "Three-dimensional earthquake sequence simulations with evolving temperature and pore pressure due to shear heating: Effect of heterogeneous hydraulic diffusivity". In: *Journal of Geophysical Research* 115, B123414. DOI: 10.1029/2010JB007780.

Noda, Hiroyuki, Nadia Lapusta, and Hiroo Kanamori (2013). "Comparison of average stress drop measures for ruptures with heterogeneous stress change and implications for earthquake physics". In: *Geophysical Journal International*. DOI: 10.1093/gji/ggt074.

Rice, James R. (2006). "Heating and weakening of faults during earthquake slip". In: *Journal of Geophysical Research* 111, B05311. DOI: 10.1029/2005JB004006.

Sibson, R. H. (1973). “Interactions between temperature and pore-fluid pressure during earthquake faulting and a mechanism for partial or total stress relief.” In: *Nature* 243.126, pp. 66–68.

Venkataraman, Anupama and Hiroo Kanamori (2004). “Observational constraints on the fracture energy of subduction zone earthquakes”. In: *Journal of Geophysical Research: Solid Earth* 109.B5.

Viesca, Robert C. and Dmitry I. Garagash (2015). “Ubiquitous weakening of faults due to thermal pressurization”. In: *Nature Geoscience* 8, pp. 875–879. DOI: 10.1038/NGEO2554.

Wibberley, Christopher AJ and Toshihiko Shimamoto (2005). “Earthquake slip weakening and asperities explained by thermal pressurization”. In: *Nature* 436.7051, pp. 689–692.

Ye, Lingling, Thorne Lay, Hiroo Kanamori, and Luis Rivera (2016). “Rupture characteristics of major and great (Mw 7.0) megathrust earthquakes from 1990 to 2015: 1. Source parameter scaling relationships”. In: *Journal of Geophysical Research: Solid Earth* 121.2, pp. 826–844.

Chapter 5

CONCLUSIONS AND FUTURE RESEARCH DIRECTIONS

We have explored models with both standard rate-and-state friction and well as models with enhanced dynamic weakening due to thermal pressurization and flash heating. We observed a variety of rupture behaviors from crack-like ruptures to pulse-like ruptures.

The standard rate-and-state model produces magnitude-invariant stress drops with interesting subtrends and breakdown energies mildly increasing with the event size, for the same fault properties. It is able to emulate increasing breakdown energy G with increasing event size through increasing values of the characteristic slip distance L. However, we see that this behavior saturates as events get larger and thus this model alone is not sufficient to match both the observed magnitude-invariant stress drop trend and increasing breakdown energy trend. One option is that off-fault dissipation, which we do not consider in our models, contributes to the observed increase of the breakdown energy for larger events. In fact, one could take increasing L as qualitative proxy for such behavior. However, it is not clear that the energies involved in the actual off-fault inelastic processes in dynamic rupture are significant enough. This is an important issue for future work.

The addition of thermal pressurization of pore fluids results in continuous weakening of the fault with slip, resulting in increasing breakdown energies with the increasing event size consistent with observations, as pointed out in previous studies. Interestingly, such models also have magnitude-invariant stress drops due to larger events having both lower average levels of prestress and and lower average final stresses. Moreover, the stress drops have reasonable values consistent with observations. The theoretical basis for this finding requires further study.

We also observe that the properties of the velocity-strengthening boundaries can have a profound effect on the stress drops of events that arrest there. The more velocity-neutral the VS region is, the more propagation into the VS region the rupture achieves, leading to larger areas of relatively small slip and zero to negative stress drops, and hence decreased average stress drops, especially for larger events. This effect can be significant enough that it controls the trend of stress drops for the largest events and is able to produce both an increasing or decreasing trend

depending on the model.

Both fault models with standard rate-and-state properties as well as the ones with the additional thermal pressurization of pore fluids produce, for the properties studied, mostly crack-like ruptures and events with transitional crack-to-pulse like behavior that still resembles a crack. These dynamic events have insignificant overshoot or undershoot, the actual available energy similar to the seismically estimated one, and both breakdown energy and radiation ratio similar to observations.

Pulse-like events are produced occasionally in our models with thermal pressurization, but much more readily in models with severe weakening due to flash heating. These events occur with significant stress undershoot and hence exhibit larger available energy than can be seismically estimated. This additional available energy can make the breakdown energy much larger than its seismically estimated value, the radiated energy much larger than the seismically estimated available energy ΔW_0, or, as is often seen in our simulations, lead to both. This makes the seismically estimated breakdown energies unreliable for pulse-like events. The radiated energy larger than ΔW_0 would lead to negative values of the seismically estimated G_{SE} and η greater than 1, as inferred for a fraction of the natural events.

As discussed in section 4.3.4, the relative rarity of negative G_{SE} and η greater than 1 suggests one of the three possibilities: (i) the large sharp pulse-like ruptures are relatively rare; (ii) these pulse-like ruptures have much larger breakdown energy than radiated energy, with actual radiation ratios of 0.1 or less, as effectively assumed in Viesca and Garagash (2015); or (iii) the seismic estimates are inaccurate, e.g., the radiation energy is significantly underestimated.

In the view of our findings, it is important to study in more detail the energy budget and average quantities for pulse-like events, since the seismically estimated values can be quite misleading for such ruptures, yet accumulating evidence suggests that many large events behave as pulse-like ruptures. Simulating a broader range of models that result in pulse-like ruptures would be needed to establish the likelihood of possibility (ii), since much larger breakdown energy than radiation energy may be inconsistent with pulse-like behavior. Exploring the validity of the estimates of the radiation energy using our models and commonly applied seismological techniques, to clarify the possibility (iii), is another direction for future work. Finally, it would be important to confirm the conclusions in 3D models with 2D faults, rather than the 2D models with 1D faults utilized in this work for numerical convenience.